Study of Earth global rheological properties through VLBI observation

Ibnu Nurul Huda

PSL★
UNIVERSITÉ PARIS

THÈSE DE DOCTORAT
DE L'UNIVERSITÉ PSL

Préparée à Observatoire de Paris

Etude des propriétés rhéologiques globales de la Terre à l'aune des observations VLBI

Soutenue par
Ibnu NURUL HUDA
Le 16 Décembre 2019

École doctorale n°127
Astronomie et Astrophysique - Ile de France

Spécialité
Astronomie et Astrophysique

Composition du jury :

Emmanuel LELLOUCH		
Observatoire de Paris	Président	
Véronique DEHANT		
Observatoire Royal de Belgique	Rapporteuse	
Lucia SEOANE		
Observatoire Midi-Pyrénées	Rapporteuse	
Marianne GREFF-LEFFTZ		
Institute de Physique du Globe de Paris	Examinatrice	
Olivier DE VIRON		
Université la Rochelle	Examinateur	
Nicolas RAMBAUX		
Observatoire de Paris	Examinateur	
Christian BIZOUARD		
Observatoire de Paris	Directeur de thèse	
Sébastien LAMBERT		
Observatoire de Paris	Co-Directeur de thèse	

Abstract

Since the beginning of the 20th century, the observation of the Earth rotation variations through astro-geodetic techniques enables to investigate the global rheological properties of the Earth, in particular, the resonance parameters of the free rotation modes reflect the solid Earth anelasticity, the ocean response to an external forcing, and the properties of the fluid inner core, eventually of the solid inner core. Better constraints on these resonance parameters can be obtained by confronting the observed terrestrial motion of the rotation pole (the so-called polar motion) - including nutation as a retrograde diurnal polar motion - to the modelled excitation producing it. The more precise the modelled excitation and the observed polar motion are, the better the Earth rheological properties will be determined. For now, the best precision are reached in the nutation band. So, our work is first dedicated to a direct adjustment of the nutation components from VLBI delays, then the adjustment of the resonance parameters in the transfer function between the observed nutation terms and the corresponding rigid nutation terms that reflects the luni-solar forcing. The obtained resonance parameters confirms in particular the shortening of the polar motion resonance period of about 40 - 50 day in the retrograde diurnal band. Then, we show that the dynamical behaviour of the oceans in the diurnal band is mostly responsible for that. We also predicted a supplementary change of the resonance parameters in the vicinity of the free core nutation resonance, as expected from the solid Earth response, and confirmed by the adjustment of these parameters through the nutation terms. In addition to the nutation band, we revisit the estimation of the polar motion resonance parameters in the seasonal band, dominated by the Chandler wobble, in light of the most recent global circulation models of the hydro-atmospheric layers. Finally, we extend the investigation of polar motion resonance to the prograde diurnal polar motion, where the excitations mostly result from the ocean tides. We ob-

tain a resonance period of about 400 days, and confirmed by our prediction based on the ocean tidal models. These results allow us to impose constraints on the frequency dependence of the Love number $\tilde{k}_2$ and the Love number oceanic $\tilde{k}_o$, characterizing respectively the response of the solid Earth and the oceans to an external potential of degree 2.

Résumé

Depuis le début du vingtième siècle, l'observation des variations de rotation de la Terre par les techniques astro-géodésiques permet de dévoiler les propriétés rhéologiques globales de la Terre. En particulier, les paramètres des modes d'oscillation libre de l'axe de rotation, qui sont aussi des paramètres de résonance - reflètent les défauts d'élasticité de la Terre solide, la réponse de l'océan au forçage externe et les propriétés de la graine fluide, éventuellement du noyau solide. On peut obtenir de meilleures contraintes sur ces paramètres de résonance en confrontant le mouvement terrestre du pôle de rotation observé (mouvement du pôle) – et aussi la nutation en tant que mouvement du pôle en rétrograde diurne - à l'excitation modélisée qui le produit. Les propriétés rhéologiques de la Terre sont d'autant mieux déterminées que le mouvement du pôle (y compris dans la bande diurne) est observé précisément et l'excitation modélisée correctement. A l'heure actuelle, si la précision du mouvement du pôle est légèrement meilleure au delà de 2 jours, la meilleure reconstitution du forçage concerne la bande de nutation (la bande rétrograde diurne), car il est procède alors des marées gravimétriques luni-solaires, lesquelles sont modélisées avec une grande précision). C'est pourquoi notre travail est d'abord consacré à l'ajustement direct des composantes luni-solaires périodiques de la nutation à partir des retards du VLBI, puis à l'estimation des paramètres de résonances dans la fonction de transfert entre ces termes de nutation observés et ceux modélisés pour une terre rigide, lesquels reflètent le forçage luni-solaire. Les résultats obtenus confirme notamment le raccourcissement d'environ 40-50 jours de la période de résonance du mouvement du pôle dans la bande rétrograde diurne. Nous montrons comment cette diminution s'explique par la réponse dynamique des océans à la marée du pôle, laquelle est étudiée à l'aune des modèles de marées océaniques diurnes . Nous prédisons également un changement des paramètres de résonance du mouvement du pôle

à proximité de la fréquence de résonance de la nutation libre du noyau ; cette modification semble confirmée par la détermination de ces paramètres à partir des termes de nutation. Notre étude des paramètres de résonance s'étend au delà de la bande de nutation. D'une part, nous réexaminons l'estimation des paramètres de résonance du mouvement du pôle dans la bande saisonnière, dominée par l'oscillation de Chandler, en utilisant les derniers modèles hydro-atmosphériques. D'autre part, nous étudions la résonance du mouvement du pôle à la bande prograde diurne, où l'excitation est dominée par la marée océanique. Nous obtenons une période de résonance de l'ordre de 400 jours, corroboré par notre modélisation fondée sur les modèles de marée océanique. L'ensemble des résultats obtenus permet d'apporter des contraintes sur la dépendance en fréquence du nombre de Love $\tilde{k}_2$ et du nombre de Love océanique caractérisant respectivement la réponse de la Terre solide et des océans à un potentiel externe de degré 2.

Contents

Introduction

Polar motion and nutation: a sensor of Earth rheology.   The observation of Earth rotation variation started more than two thousands years ago. Hipparchus (190-120 BC) observed a motion of the stars with respect to the autumnal equinox at the rate of about 50 arcsecond per year. This phenomenon, called *precession*, corresponds to a conical motion of the Earth rotation axis around the polar axis of the ecliptic. Thousands of years later, the emergence of the telescopic era allowed an English astronomer, James Bradley, to discover a superimposed oscillation of the rotation axis with a 18.6-year period called *nutation*.

Until the 19th century, the only known motion of the rotation axis was the precession-nutation. This motion has an astronomical cause: the lunisolar tidal torque on the equatorial bulge of the Earth. Meanwhile, in the middle of the 18th century, Euler predicted the existence of a motion of a rotation pole with respect to the crust due to the Earth flattening, especially a free wobble at the period of 304 days. This terrestrial wobble of the rotation pole, called *polar motion*, was observed at the eve of the 20th century. It is mostly composed of a wobble in 430 day, called Chandler Wobble (CW), and an annual term. Whereas the annual term unveils the seasonal mass redistribution within the atmosphere and the oceans, the CW is interpreted as the Euler free mode modified by the Earth non-rigidity, and forced as well by the mass redistribution in the hydro-atmosphere. Therefore, the polar motion provided a new kind of data for investigating the Earth's global rheological properties, including the response of the ocean to an external forcing. At the same epoch, from the presence of an internal fluid core, Poincaré concluded the existence of a second mode of rotation, called free core nutation (FCN). This mode influences the nutation at the level of 50 milliarcsecond (mas). Detected in the 1970s, it was fully confirmed in the 1980s by Very Long Baseline Interferometry (VLBI) observations.

1

Actually, it can be shown that the nutation in the terrestrial frame can be considered equivalently as a retrograde diurnal polar motion.

The CW and FCN resonances appear theoretically in the angular momentum balance of the Earth composed of a mantle and a fluid core. A three-layered Earth, where the solid inner core is added, leads to two supplementary modes: a prograde diurnal mode of about one day, corresponding to the Free Inner Core Nutation (FICN) in the celestial reference frame with a period of about 500-1000 days, and a terrestrial wobble of 7 years, named Inner Core Wobble or ICW. Until now, these two modes remain quite speculative and have not been clearly detected. In the framework of a three-layered Earth, the frequency parameters pertaining to CW, FCN, FICN, and ICW are related to several Earth rheological parameters such as the dynamical ellipticity of the Earth layers, mantle inelasticity, and the properties of fluid and solid inner core.

Motivation. Hence, the study of Earth rotation, especially the resonance parameters, allows a link to the Earth rheology and its internal structure. Actually, several authors have estimated the resonance parameters either in the common polar motion band (see, e.g. Furuya and Chao, 1996; Kuehne et al., 1996; Nastula and Gross, 2015), i.e., from two days to secular time scale, or in the retrograde diurnal band, that is the nutation band (see, e.g. Mathews et al., 1991a, 2002; Rosat et al., 2016). However, until now, there is no study that gives a comprehensive picture of the Earth resonance parameters in both frequency bands. So, we aim at estimating the resonance parameters in the polar motion and nutation band, and even extending it into the prograde diurnal band. These parameters can be determined by comparing observed polar motion or nutation to the modeled excitation producing it.

Contents. This thesis is divided into three parts. In the first part, we deal with the estimation of the resonance parameters in the common polar motion band (from 10 days to 10 years). In the Chapter 1, we recall the polar motion theory for a two-layer Earth model, which forcing is restricted to the internal mass transports. The corresponding polar motion resonance (PMR) parameters are estimated in Chapter 2.

In the second part, we consider the resonance in the diurnal retrograde band, or the nutation band in the celestial frame. Then, the theory has to be extended to a three-layered Earth, as

explained in Chapter 3. For the lunisolar nutation, forced by the gravitational tides, the problem can be restricted to the transfer function between the observed nutation terms and the corresponding rigid Earth nutation terms, which describe the excitation process. Chapter 4 provides details about the nutation terms adjustment to VLBI observations. In this Chapter, we introduce a so-called "direct" approach that permits to increase the precision of the determination of nutation amplitudes. In Chapter 5, the resonance parameters are estimated by using the results from Chapter 4, the influence of a non-tidal atmospheric and oceanic excitation to the estimated resonance parameters is also discussed. A geophysical explanation of the results obtained in the retrograde diurnal band for the PMR parameters is given in Chapter 6.

The third part is an extension to the prograde diurnal band. Both theoretical background and estimation of the resonance parameters are given in the unique Chapter 7.

Part I

Common polar motion band

Chapter 1

Theory: Earth with 2 layers

1.1 Liouville equation

The theoretical development of Earth rotation variations has been done in many ways. However, it may be classified into two major branches, either using the Hamiltonian formalism or the law of angular momentum balance. For studying geophysical effects, the second approach is much more easier to handle and is favoured in this work.

The law of angular momentum balance states that the Earth angular momentum $\mathbf{H}$ is related to the external torque $\boldsymbol{\Gamma}$ acting on it in the terrestrial reference system as follows

$$\frac{d\mathbf{H}}{dt} + \omega \times \mathbf{H} = \boldsymbol{\Gamma} \ , \tag{1.1}$$

where ω is the instantaneous rotation vector of the Earth. The angular momentum is composed of a term related to the Earth moment of inertia matrix $\mathbf{I}$ and of the relative angular momentum $\mathbf{h}$:

$$\mathbf{H} = \omega \cdot \mathbf{I} + \mathbf{h} \ . \tag{1.2}$$

Here $\mathbf{I}$ depends on the Earth mass distribution whereas $\mathbf{h}$ is produced by any velocity field appearing in the Earth system, especially the winds and the oceanic currents. The substitution of (1.2) into (1.1) leads to the Liouville equation:

$$\frac{d(\omega \cdot \mathbf{I} + \mathbf{h})}{dt} + \omega \times (\omega \cdot \mathbf{I} + \mathbf{h}) = \boldsymbol{\Gamma} \ . \tag{1.3}$$

Since the deviation from uniform rotation is small, the linearization can be applied to (1.3). First, the rotation vector and moment of inertia are split into their constant and perturbation parts:

$$\omega = \omega_0 + \Delta\omega = \begin{bmatrix} 0 \\ 0 \\ \Omega \end{bmatrix} + \begin{bmatrix} \Omega m_1 \\ \Omega m_2 \\ \Omega m_3 \end{bmatrix} = \begin{bmatrix} \Omega m_1 \\ \Omega m_2 \\ \Omega(1 + m_3) \end{bmatrix}, \tag{1.4}$$

and

$$\mathbf{I} = \mathbf{I}_0 + \Delta\mathbf{I} = \begin{bmatrix} A & 0 & 0 \\ 0 & B & 0 \\ 0 & 0 & C \end{bmatrix} + \begin{bmatrix} c_{11} & c_{12} & c_{13} \\ c_{21} & c_{22} & c_{23} \\ c_{31} & c_{32} & c_{33} \end{bmatrix}, \tag{1.5}$$

where $\Omega = 7.2921150 \times 10^{-5}$ rad/s is the reference Earth angular velocity, A and B are the equatorial moments of inertia, C is the axial moment of inertia, and c_{ij} are small increments of inertia due to the mass redistribution. Here m_1, m_2, and $1 + m_3$ correspond to the direction cosines of the Earth instantaneous rotation axis with respect to the terrestrial reference frame. As $A \approx B$, we introduce the averaged value of the Earth equatorial moment of inertia $\bar{A} = (A + B)/2$. In the following, we consider the Earth as a bi-axial body ($A = B = \bar{A}$).

By substituting the expression (1.4) and (1.5) to (1.3), and by neglecting the second order quantities with respect to m_i and c_{ij}, we obtain the linearized Liouville equation, where the equatorial part is given by

$$m + \frac{i}{\sigma_e}\dot{m} = \chi - \frac{i}{\Omega}\dot{\chi} + \frac{i\,\Gamma}{(C - \bar{A})\Omega^2} \cdot \tag{1.6}$$

Here $m = m_1 + i\,m_2$ is the complex rotation pole coordinate and $\sigma_e = e\Omega$ is the Euler angular frequency, where $e = (C - \bar{A})/\bar{A} \sim 1/304$ is the dynamical ellipticity of the Earth. The quantity $\chi = \chi_1 + i\chi_2$ is called the angular momentum function and defined as

$$\chi_1 = \frac{c_{13}}{C - \bar{A}} + \frac{h_1}{(C - \bar{A})\Omega} \,,$$
$$\chi_2 = \frac{c_{23}}{C - \bar{A}} + \frac{h_2}{(C - \bar{A})\Omega} \cdot \tag{1.7}$$

This function can be divided into the *mass* term χ_{ma}, which is related to a change in the moment of inertia $c = c_{13} + i\,c_{23}$, and the *motion* term, which is related to the relative angular momentum $h = h_1 + i\,h_2$:

$$\chi_{ma} = \frac{c}{C - \bar{A}} \,,$$
$$\chi_{mo} = \frac{h}{(C - \bar{A})\Omega} \,. \tag{1.8}$$

1.2   Liouville equation of pole coordinates

The variation of Earth rotation axis is monitored through several space geodetic techniques such as VLBI, Global Navigation Satellite System (GNSS), and Satellite Laser Ranging (SLR) (see A.1 for the details of each technique). However, they determine the celestial and terrestrial oscillation of the CIP or Celestial Intermediate Pole (see A.2) which differs from the instantaneous rotational axis up to 20 mas (Bizouard, 2014). The position of CIP with respect to the terrestrial frame is called *pole coordinates* $p = x - iy$. The relation between m and p is given by

$$m = p - \frac{i}{\Omega}\dot{p} \,. \tag{1.9}$$

Substituting this expression of m into (1.6), and casting aside the external torque in view of the linearity of the problem, we obtain

$$p + \frac{i}{\sigma_e}\dot{p} - \frac{i}{\Omega}\frac{d}{dt}\left(p + \frac{i}{\sigma_e}\dot{p}\right) = \chi - \frac{i}{\Omega}\dot{\chi} \,. \tag{1.10}$$

This equation can be reduced to

$$p + \frac{i}{\sigma_e}\dot{p} = \chi \,, \tag{1.11}$$

where the left-hand side of (1.11) is named the *geodetical excitation* since it is estimated through astrogeodetic observation and the right-hand side is called the *geophysical excitation* since it is reconstructed from a geophysical model, like global atmospheric circulation model. In the frequency domain, the equation (1.11) is written as

$$p(\sigma) = T(\sigma)\chi(\sigma) \,, \tag{1.12}$$

where the transfer function $T(\sigma)$ is given by

$$T(\sigma) = -\frac{\sigma_e}{\sigma - \sigma_e} \,. \tag{1.13}$$

1.3 Influence of the Earth non rigidity

The equation (1.11) is not adequate to describe the polar motion, as it still ignores the Earth non-rigidity, especially it does not account the planetary deformation produced by the variation of centrifugal force accompanying the displacement of the rotation pole. By considering this phenomenon, the dynamical system of (1.11) becomes

$$p + \frac{i\dot{p}}{\tilde{\sigma}_{PMR}} = \chi^{eff} = \chi^{eff}_{ma} + \chi^{eff}_{mo} , \qquad (1.14)$$

where $\tilde{\sigma}_{PMR}$ is the complex angular frequency of PMR:

$$\tilde{\sigma}_{PMR} = \sigma_e \frac{\bar{A}}{A_m} \left(1 - \frac{\tilde{k}_2 + \tilde{k}_o}{k_s} \right) . \qquad (1.15)$$

Here $k_s = 0.938$ is the secular Love number, $\bar{A}$ and A_m are the mean equatorial moments of inertia of the whole Earth and of the mantle respectively, $\tilde{k}_2$ and $\tilde{k}_o$ are the complex Love number describing the anelastic response for the solid Earth and the ocean response respectively. Here "~" is the symbol of the complex quantity. It has to be noted that the imaginary part of $\tilde{k}_o$ is vanished in the common polar motion band since the ocean response is considered at equilibrium.

This resonance has to be distinguished from the observed CW resonance. Indeed, as a resonant process, the CW does not result from a single harmonic excitation at the resonance frequency, but from a broadband process surrounding the resonance frequency. If the spectral content of the excitation dominates at a slightly different frequency, this one will determine the observed CW frequency. In contrast, the PMR frequency $\tilde{\sigma}_{PMR}$ is fixed by the properties of the Earth and does not depend on the forcing.

Meanwhile, the effective angular momentum function χ^{eff} taking the form

$$
\begin{aligned}
\chi^{eff}_{ma} &= \frac{1 + k_2'}{1 - \frac{\tilde{k}_2 + \tilde{k}_o}{k_s}} \chi_{ma} , \\
\chi^{eff}_{mo} &= \frac{1}{1 - \frac{\tilde{k}_2 + \tilde{k}_o}{k_s}} \chi_{mo} .
\end{aligned}
\qquad (1.16)
$$

Here χ^{eff} means an "effective" version of χ accounting for the pole tide deformation by Love number $\tilde{k} = \tilde{k}_2 + \tilde{k}_o$ and loading deformation through the loading Love number k_2'.

The complex PMR angular frequency can be written in the form of its period P_{PMR} and quality factor Q_{PMR} as follows

$$\tilde{\sigma}_{PMR} = \sigma_{PMR}(1 + i/2Q_{PMR}) \,,$$
$$\sigma_{PMR} = 2\pi/P_{PMR} \,,$$
(1.17)

where Q_{PMR} is inversely proportional to the damping factor $\alpha_{PMR} = \sigma_{PMR}/(2Q_{PMR})$. Applying a Fourier transform to (1.14), we obtain

$$p(\sigma) = -\frac{\tilde{\sigma}_{PMR}}{\sigma - \tilde{\sigma}_{PMR}}\chi^{eff}(\sigma) \,.$$
(1.18)

Hence, the transfer function of (1.13) becomes

$$T(\sigma) = \frac{p(\sigma)}{\chi^{eff}(\sigma)} = -\frac{\tilde{\sigma}_{PMR}}{\sigma - \tilde{\sigma}_{PMR}} \,.$$
(1.19)

The comparison of the transfer function amplitude in (1.19) and (1.13) is shown in Figure 1.1. The non-rigidity of the Earth has shifted the resonance toward a lower frequency and the dissipation decreases the maximal amplitude from infinite down to 40 for a very strong damping ($Q_{PMR} = 20$).

1.4   Modelling of the hydro-atmospheric excitation

At seasonal time scale, the geophysical excitation χ generally comes from non-tidal transports in the atmosphere, oceans, and land-water layers. Their respective contributions are obtained by the reconstruction of their moment of inertia (matter term) c_F and their relative angular momentum (motion term) h_F from global circulation models (Eubanks, 1993). As the equatorial momentum of a fluid layers is $H_F = \Omega c_F + h_f$, these data are generally named atmospheric, oceanic, hidrological angular momentum.

In the case of atmospheric angular momentum, there are two types of data for the matter term depending on whether the oceans respond isostatically to overlying barometric loading, like Inverted Barometer (IB), or their surface remains rigid such as Non-Inverted Barometer (NIB). In the IB data, air pressure variations do not impact the ocean bottom, whereas in the NIB data, the atmospheric load simply transmits directly to the ocean bottom. For periods

longer than one week, the response of the ocean to the atmospheric surface pressure forcing is static. Thus, the IB ocean model quite well describes the ocean-atmospheric isostatic coupling at a time scale longer than one week.

As seen above, the hydro-atmospheric excitation is amplified by the deformation process in the Earth crust. This process is accounted for by considering the deformation parameters and introducing the effective angular momentum function, referred EAAM for the atmosphere, EOAM for the ocean, and EHAM for the land-water.
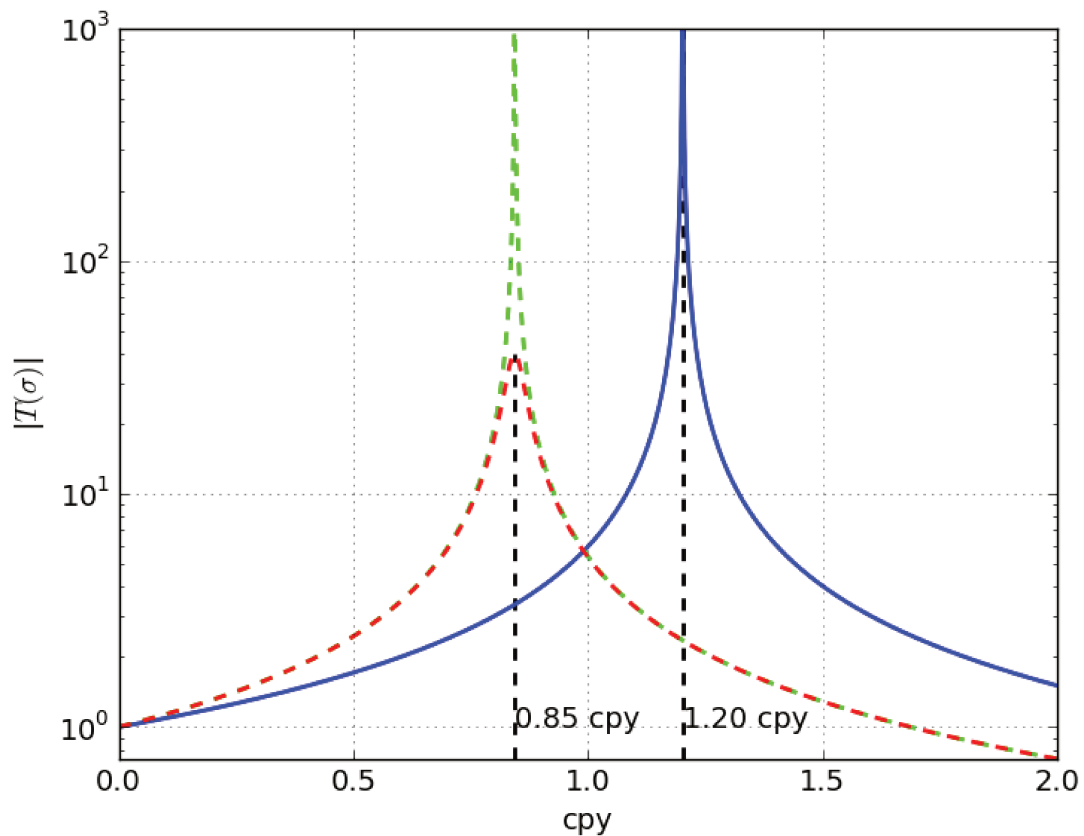

Figure 1.1 – The comparison of the transfer function's amplitude from rigid and non-rigid Earth model. Here — is for the rigid Earth, —— is for the non-rigid Earth with $Q_{PMR} = 20$ (maximal damping), and —— is for the non-rigid Earth with $Q_{PMR} = 150000$ (minimal damping).

Chapter 2

Polar motion resonance estimation in seasonal band

Before 1990s, in the absence of a precise modeling, the equatorial geophysical excitation was assimilated to a Gaussian white noise (see, e.g. Wilson and Haubrich, 1976; Wilson and Vicente, 1980) for undertaking the estimation of PMR parameters. Nowadays, many studies (see, e.g. Brzeziński et al., 2012) have concluded that the sub-secular part of the polar motion excitation can be well reconstructed from global circulation taking place in the hydro-atmospheric layer, composed of the atmosphere, ocean, and land-water. This information has been considered for adjusting the resonance parameters. The early studies, which considered the atmospheric excitation, have been done, for example, by Furuya and Chao (1996) and Kuehne et al. (1996). The more recent studies (see, e.g. Nastula and Gross, 2015) considered a more complete excitation by including ocean and land-water angular momentum. In this study, this issue is revisited by improving the estimation technique reported in Kuehne et al. (1996), and considering the full hydro-atmospheric excitation as known today. Hereafter, to avoid any ulterior confusion, we will use the term "Chandler Wobble" or CW for referring to the PMR in the seasonal band.

2.1 Data

The geophysical excitation is constituted by the EAAM and EOAM series calculated at Ge-oForschungsZentrum (GFZ). These series are based upon the European Centre for Medium-Range Weather Forecasts (ECMWF) and the Max Planck Institute Ocean Model (MPIOM) model (Dobslaw et al., 2010), and are available from 1976 with a 3 hr sample interval. As a comparison, we also used another data available through the Global Geophysical Fluid Center of the International Earth Rotation Service (IERS): EAAM produced by National Center for Environmental Prediction (NCEP) reanalysis (Kalnay et al., 1996) and EOAM data calculated from the output of the Estimating the Circulation and Climate of the Ocean (ECCO) model (Gross et al., 2005). NCEP data is sampled at 6 hr interval from 0hUTC, whereas ECCO data is given at 0hUTC and with 10 day steps from 1948 to 1998 and once per day afterward. All these series provide the corresponding matter and motion terms. In the case of EAAM, we select the matter term derived according to the IB approximation, quite well describing the ocean-atmospheric coupling in the seasonal band as mentioned in the Chapter 1. The comparison between the EAAM series of ECMWF and NCEP as well as the EOAM series of MPIOM and ECCO are shown in Figure 2.1 and 2.2 respectively. Besides the ocean and atmosphere, land-water has a significant contribution to the geophysical excitation. To quantify the influence of this component, we use the angular momentum function of the land-water (HAM) produced at GFZ from the Land Surface Discharge Model (LSDM) (Dobslaw et al., 2010) given at 12hUTC once per day. The time series of EHAM are shown in Figure 2.3.

Meanwhile, pole coordinates come from C04 daily series (Bizouard et al., 2018). They are obtained from the combination of operational Earth Orientation Parameter (EOP) series, including also celestial pole offset and UT1-UTC, derived from the astro-geodetic techniques, namely VLBI, GNSS, SLR, and DORIS. The Table 2.1 summarises the data that we used for this estimation.

Figure 2.1 – EAAM time series. Before plotting, the time series are re-sampled at 10 day interval and the linear trend and biases are removed. Here — corresponds to NCEP series and — to ECMWF series.

Figure 2.2 – EOAM time series. Before plotting, the time series are re-sampled at 10 day interval and the linear trend and biases are removed. Red color — corresponds to ECCO series and blue color — to MPIOM series.
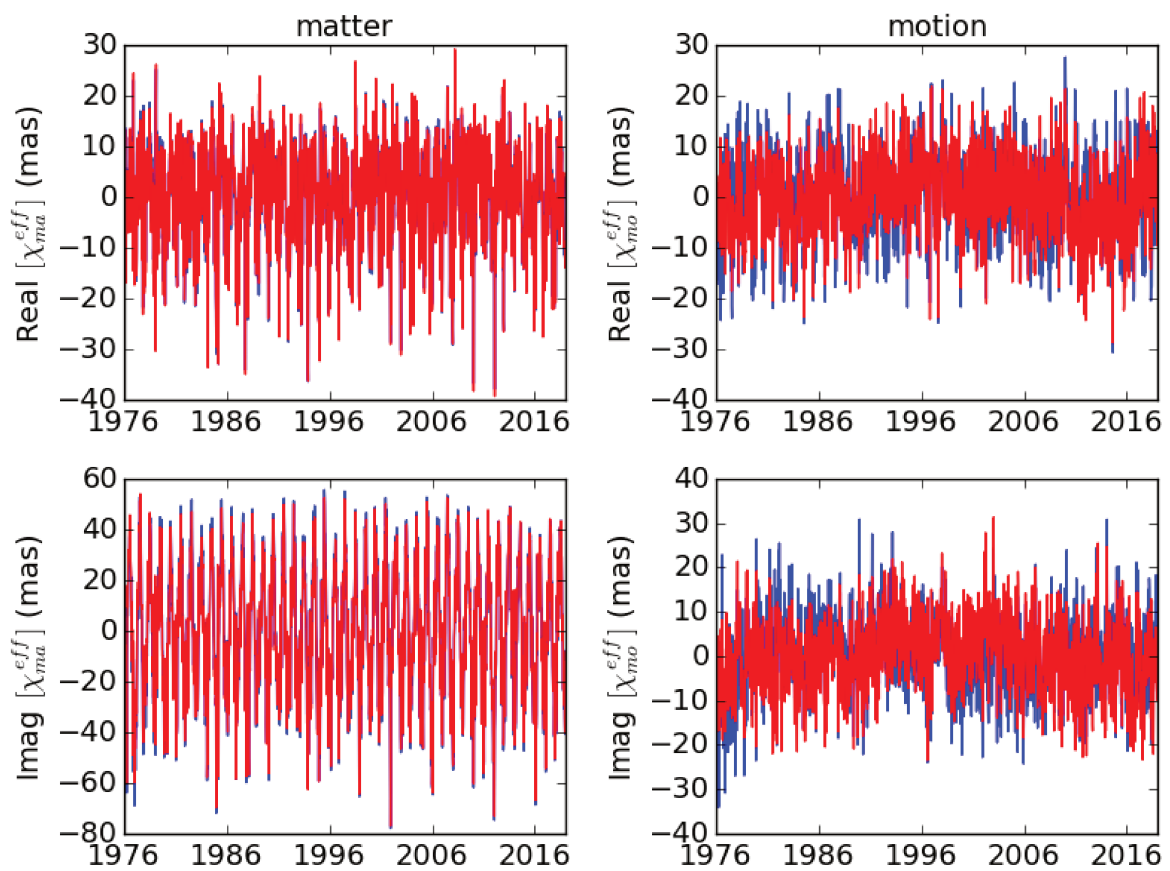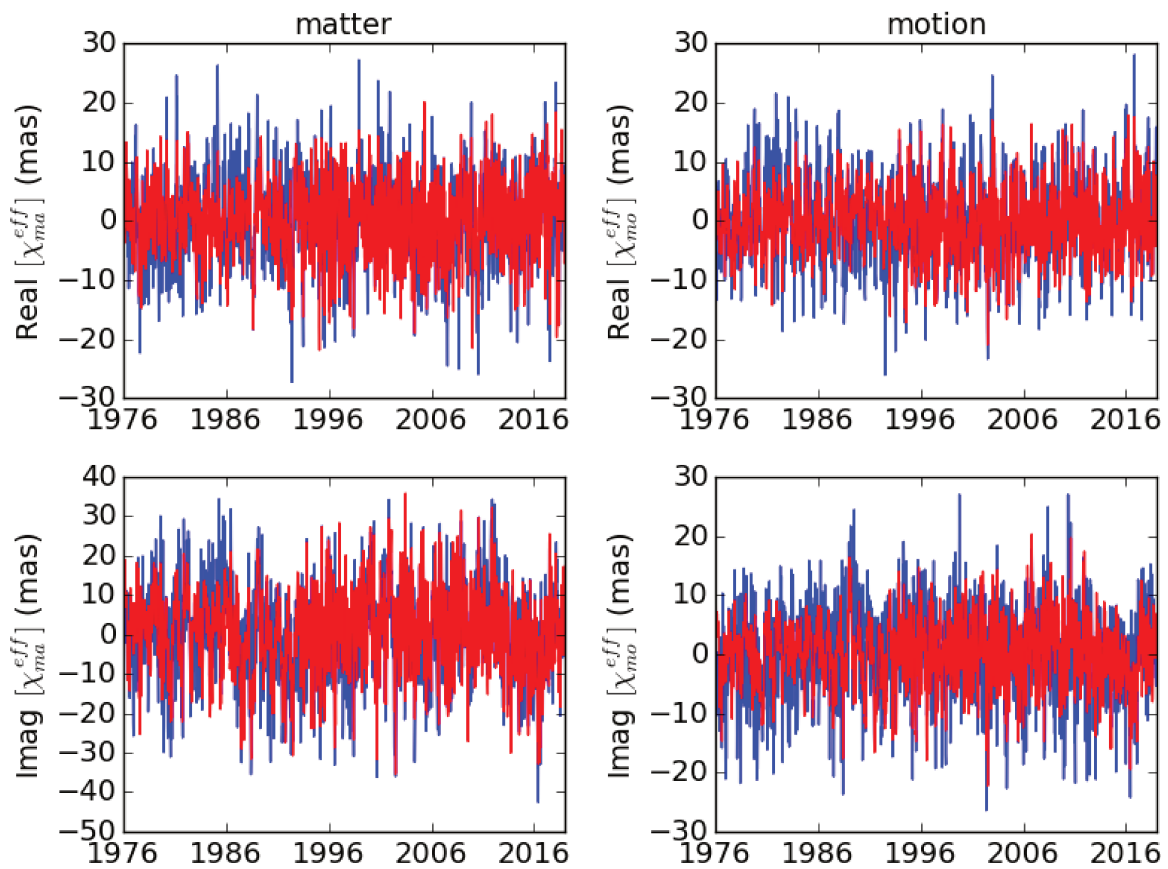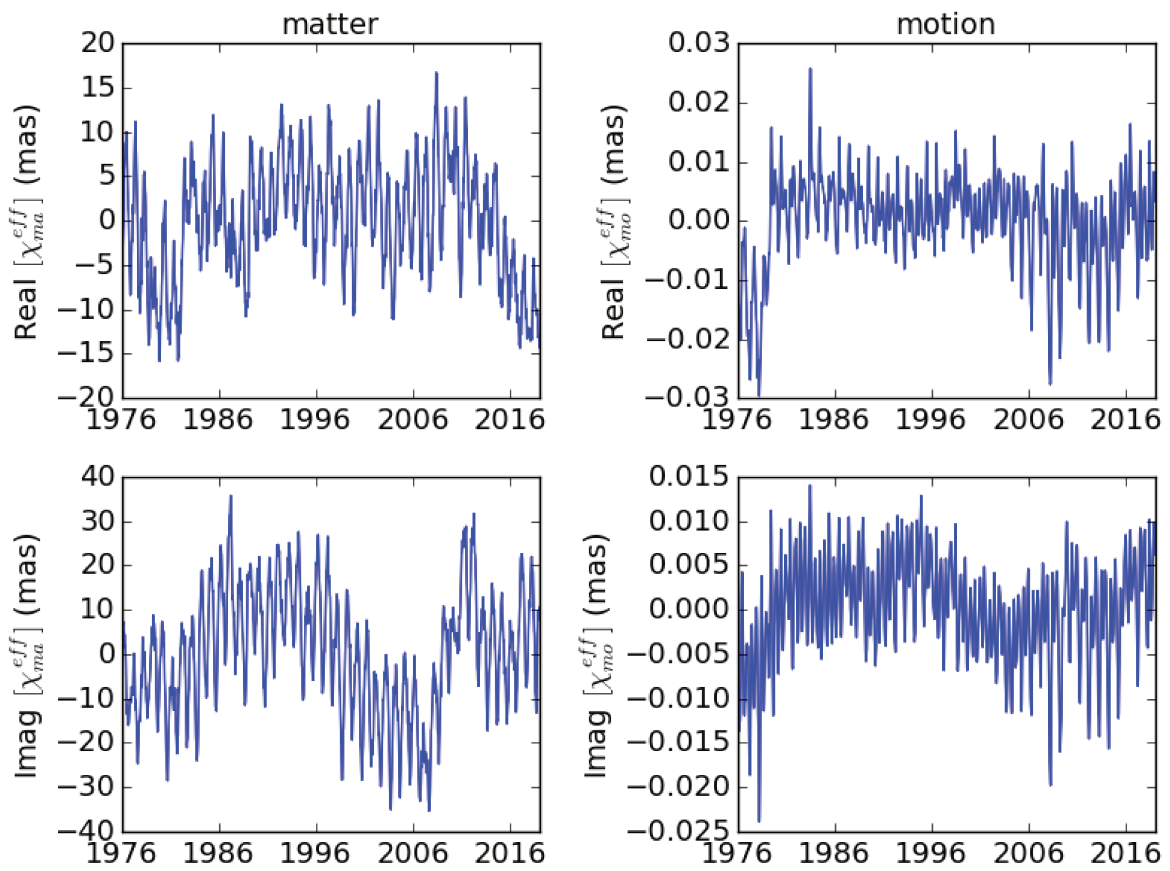
Figure 2.3 – EHAM time series. Before plotting, the time series are re-sampled at 10 day interval and the linear trend and biases are removed.

Table 2.1 – Synopsis of the geophysical excitation and observed polar motion data.

	model or series name	version	available data	sampling interval
Atmosphere	ECMWF	v1.0	1976 - 2019	3 hours
	NCEP	reanalysis	1948 - 2019	6 hours
Ocean	MPIOM	v1.0	1976 - 2019	3 hours
	ECCO	50yr	1948 - 2002	10 day
	ECCO	kf080i	1998 - 2019	1 day
Land water	LSDM	v1.2	1976 - 2019	3 hours
Polar coordinate	C04	-	1962 - 2019	1 day

2.2   Chandler parameters estimation

The PMR parameters can be roughly estimated by using the spectral approach. In this approach, the geophysical excitation is assumed to be white noise, characterized by a flat power spectrum. Then, the PMR frequency corresponds to the maximum of the spectral power, and the quality factor is calculated from the full width at half maximum (FWHM) by $Q_{PMR} = \sigma_{PMR}/FWHM$. For instance, based on the spectral plot of Figure 2.4, we can deduce $\sigma_{PMR} = 0.842$ cpy and FWHM = 0.04 cpy, corresponding to $P_{PMR} = 433$ days and $Q_{PMR} = 45$. However, this technique has some deficiencies. First, the estimate of Q_{PMR} depends on the spectral resolution. Second, as shown in the log-log plot of Figure 2.5, the spectral power of the excitations are not completely flat, even for the band near CW frequency (0.5 - 1.1 cpy), either for NCEP + ECCO series or ECMWF + MPIOM series. Thus, the real geophysical excitation is not perfectly white noise, which contradicts the assumption.

In order to refine the estimation of CW parameters, the information from geophysical excitation model have to be considered. So, the estimation can be done by using equation (1.14). The L.H.S. of this equation (geodetic excitation), which contains a time derivative of the polar motion, has to be adapted to a discrete polar coordinates. Hence, we adopt the digitization
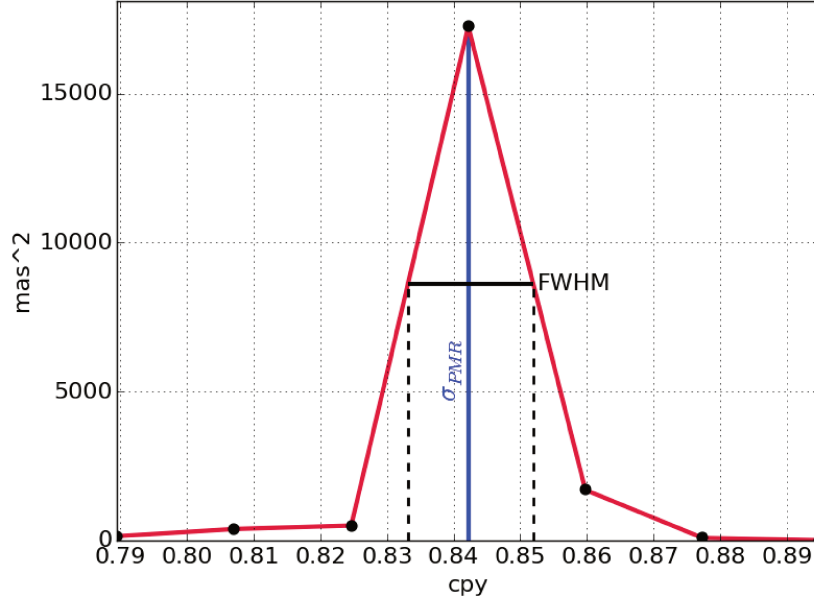
Figure 2.4 – Spectral power of the polar motion around PMR frequency (0.844 cpy) over the period 1962 - 2019 (combined series C04).

proposed in Wilson (1985):

$$\chi_{t+h/2}^{eff} = (a p_{t+h} + b p_t) \,,$$

$$a = \frac{i\,e^{-i\pi f_{CW}h}}{\tilde{\sigma}_{CW}\,h} \,, \tag{2.1}$$

$$b = -a\,e^{i\tilde{\sigma}_{CW}h} \,,$$

where the complex frequency $\tilde{\sigma}_{CW} = 2\pi f_{CW}(1 + i/2Q_{CW})$ describes the PMR affecting an extensive frequency band from one month to several years.

This Wilson filter tends to slightly mitigate the amplitude of the geodetic excitation of (1.14) at short periods approaching the sampling period h. This edge effect can be neglected if we consider fluctuations much larger than h. Meanwhile, it is clearly seen in (2.1) that the variable a and b are linearly correlated. This correlation is avoided by modifying (2.1) as follows

$$rp_t = \left(\frac{\chi_{t+h/2}^{eff}}{a} - p_{t+h}\right) \,, \tag{2.2}$$

where $r = b/a = -e^{i\tilde{\sigma}_{CW}h}$. Hence, the CW parameters are determined by

$$P_{CW} = \frac{2\pi h}{arg(-r)} \qquad Q_{CW} = \frac{-h\pi f_{CW}}{\log|-r|} \ . \qquad (2.3)$$

The CW parameters are estimated through r by a least-square adjustment. First, the variable a is initialized by using a-priori values of $P_{CW} = 433$ days and $Q_{CW} = 100$. Then r is adjusted from which we derive the new values of P_{CW} and Q_{CW}. These values yield to a new a value. We iterate these steps until the estimated value converges. Since the geophysical excitation and the polar coordinate data do not have the same sample interval, we applied a low pass filter by using Butterworth method before the inversion and resampled the data at a 10 day interval, corresponding to the sampling interval of ECCO version 50yr (see Table 2.1). We also remove the linear decadal trends (beyond 10 years) of the polar motion series by using the Butterworth high-pass band filter. The CW parameters are estimated over the period 1976 - 2019, corresponding to the available geophysical excitation data produced by the GFZ.
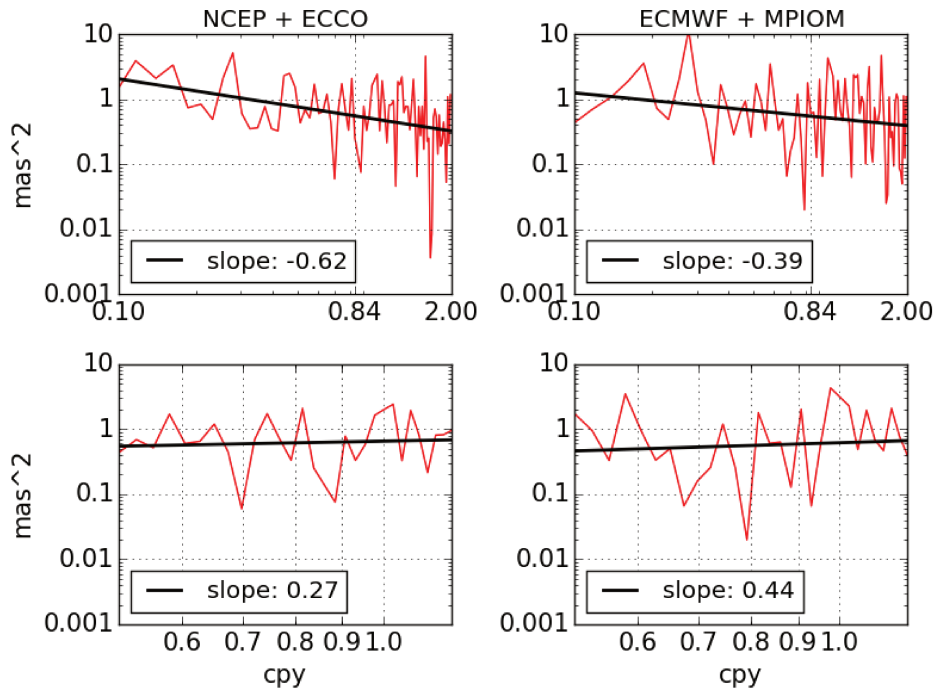

Figure 2.5 – Geophysical excitation spectral power for two different time series over the period 1976 - 2019. Here the horizontal and vertical axis are shown in logarithmic scale.

2.3   Results

We estimate the CW parameters in two ways. First, we consider all of seasonal terms. Second, we eliminate the seasonal components with periods $1/n$ yr, where $n = 1, 2, 3, 4, 5, 6$, by least square adjustment, both for their prograde and retrograde parts. The estimation is performed for three sets of geophysical excitations: NCEP + ECCO, ECMWF + MPIOM and ECMWF + MPIOM + LSDM over the period 1976 - 2019. As shown in Table 2.2, the inconsistency of CW period between ECMWF + MPIOM and NCEP + ECCO sets disappeared when we eliminate the seasonal terms, yielding the values of CW period in the range between (431.6, 434.5). Moreover, the exclusion of seasonal terms leads χ^2 slightly getting closer to one. However, the presence of seasonal terms better constraints the range of quality factor (33, 57) versus (41, 109) when the seasonal contribution is suppressed. The addition of land-water (LSDM) to the ECMWF + MPIOM improves the estimation by reducing the χ^2 from 4.70 to 4.36 in the case of when the seasonal terms are present and from 4.13 to 3.85 in the case of when the seasonal terms are excluded.

Table 2.2 – The estimated CW parameters from combined atmospheric-oceanic excitation according to several geophysical excitation series. Here we used the data from 1976 to 2019. The uncertainty corresponds to 1σ.

	Periode (days)	Q	χ^2
with seasonal terms			
NCEP + ECCO	425.8 ± 0.9	$(33, 48)$	4.40
ECMWF + MPIOM	433.9 ± 1.0	$(36, 57)$	4.70
ECMWF + MPIOM + LDSM	433.2 ± 0.9	$(35, 52)$	4.36
seasonal terms excluded			
NCEP + ECCO	432.6 ± 1.0	$(50, 109)$	4.12
ECMWF + MPIOM	433.5 ± 1.0	$(45, 88)$	4.13
ECMWF + MPIOM + LSDM	432.4 ± 1.0	$(41, 74)$	3.85

The robustness of the estimated parameters is analyzed by fitting the parameters over a decreasing range of data ($\Delta = t_f - t_i$). We start with $t_i = 1976$ and increase by steps of one year until $t_i = 2018$, whereas t_f is fixed at 2019. Figure 2.6 displays the results. Whatever the data range, the geophysical models lead to a consistent period when we exclude the seasonal terms. Moreover, this exclusion makes the quality factor less constrained, with two geophysical series yielding a similar result for the data range over 25 years (i.e. $t_i < 1993$).

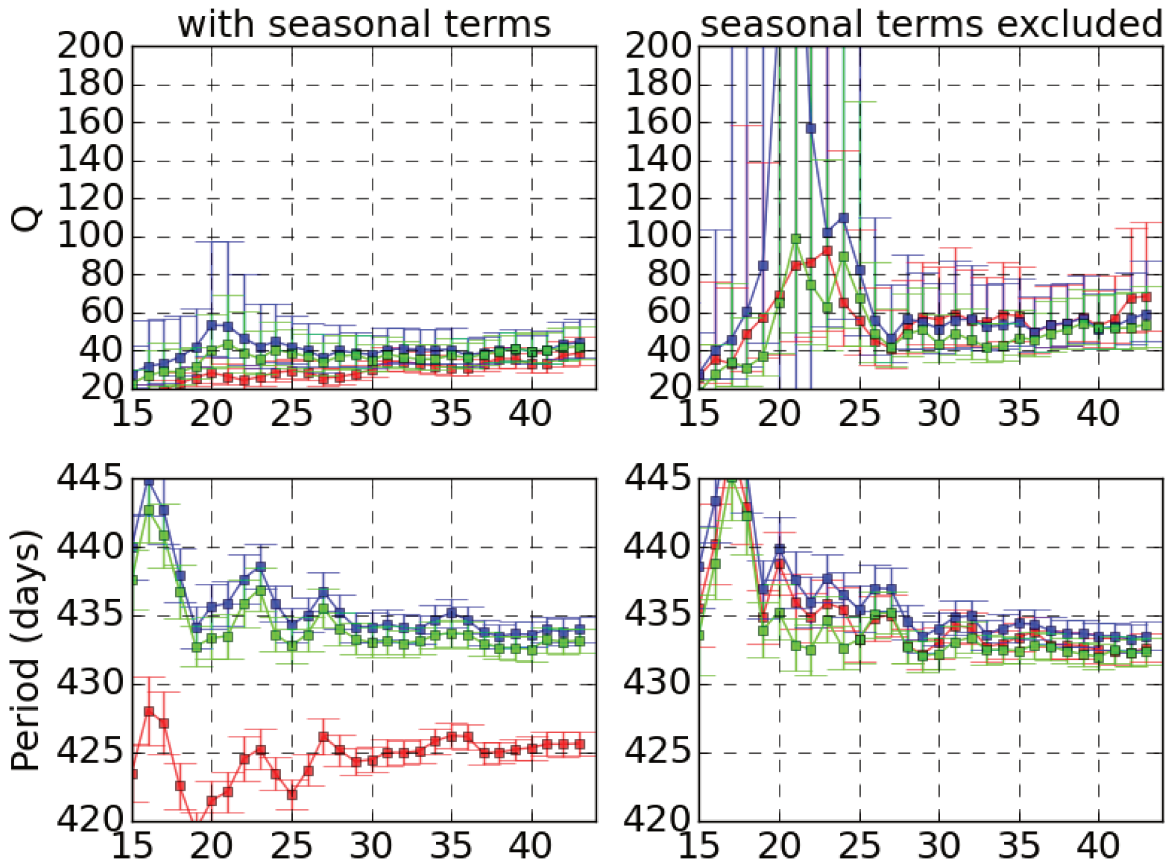Figure 2.6 – CW parameters for three sets of hydro-atmospheric excitation in function of the data range. The abscissa means $\Delta t = t_f - t_i$ in years with t_f is 2019. Here ■ corresponds to NCEP + ECCO, ■ to ECMWF + MPIOM, and ■ to ECMWF + MPIOM + LSDM.

Figure 2.7 shows a comparison of CW parameters estimates based upon the matter and motion term only as well as their combination over the period 1976 - 2019. The removal of

the matter term affects the results, and thus pointing out that the matter term is much more influential on the estimation of CW parameters.

Table 2.3 shows the comparison of our estimated parameters to the previous ones. Our estimates match with the results published in the previous studies, and lie well within the given interval of 433 - 435 days for the period and 30 - 1000 for the quality factor. However, the estimated period of Kuehne et al. (1996) significantly differs from ours. It is likely due to the presence of decadal band as well as the absence of the ocean and land-mass excitation in the estimation which can lengthen the estimated period.
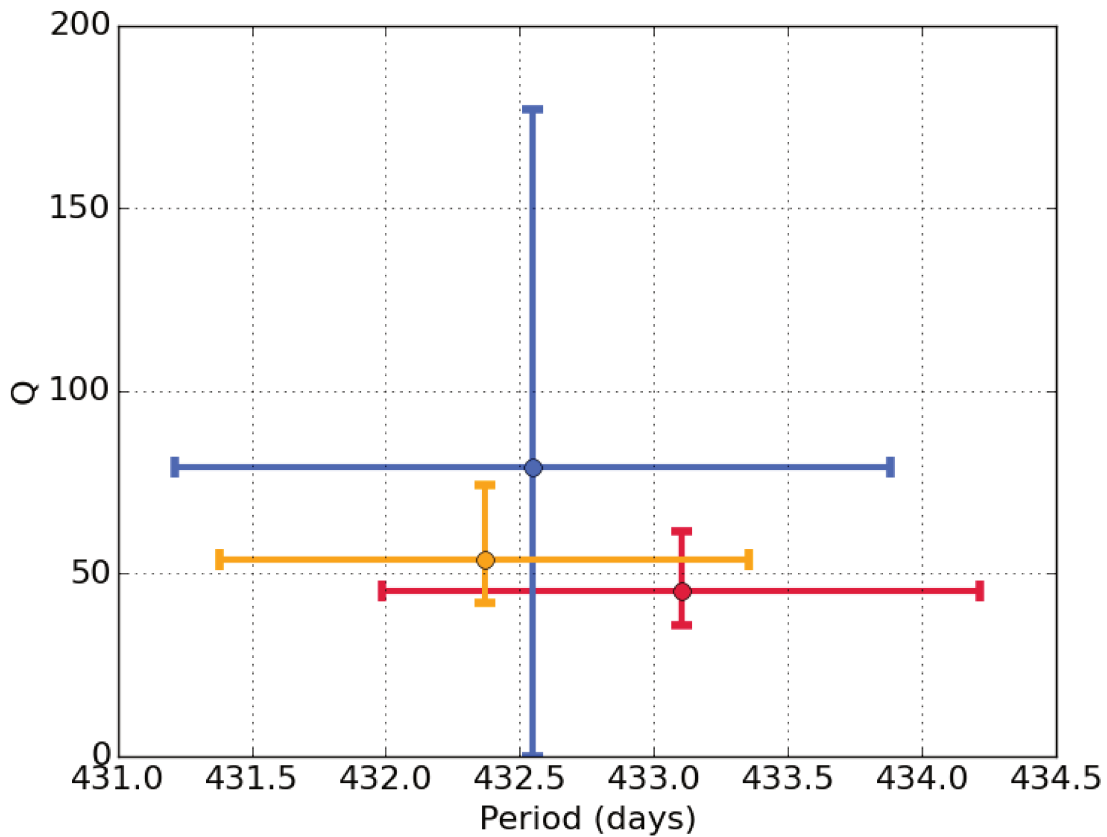
Figure 2.7 – The estimated CW parameters from matter term only •, motion term only •, and their combined contribution •. Here we used the data from 1976 to 2019.

Now, we calculate the Love number $\tilde{k}_2$ from the estimated CW period and quality factor,

reported in Table 2.2. From (1.15) the expression of $\tilde{k}_2$ is

$$\tilde{k}_2 = k_s \left(1 - \frac{\tilde{\sigma}_{PMR}}{\sigma_e} \frac{A_m}{\bar{A}} \right) - \tilde{k}_o \,, \tag{2.4}$$

where $\tilde{\sigma}_{PMR}$ is given from estimated parameters by (1.17). In the band selected for estimating these parameters, we can assuming an hydrostatic ocean pole tide, described by oceanic Love number $k_o = 0.0477$ (Desai, 2002). Moreover we select the more robust estimates of P_{CW} and Q_{CW} obtained in the case "seasonal terms excluded". As shown in Table 2.4, the estimated $\tilde{k}_2$ lies in the interval (0.305, 0.310) for the real part and (-0.0071, -0.0027) for the imaginary part. This result matches the $\tilde{k}_2$ value proposed in IERS Convention 2010 (Petit and Luzum, 2010) $(0.307 - i\,0.0035)$.

Table 2.3 – List of the previous results based on Table 2 in Nastula and Gross (2015) and our result from ECMWF + MPIOM + LSDM set.

Period (days)	Q	Data span (years)	Reference*
Statistical excitation			
433.2 ± 2.2	(36,192)	67.6	(a)
434.0 ± 2.6	(50,400)	70	(b)
434.8 ± 2.0	(50,300)	76	(c)
433.3 ± 3.1	(47,1000)	78	(d)
433.0 ± 1.1	(74,789)	86	(e)
Atmospheric excitation			
439.5 ± 2.1	(30,500)	8.6	(f)
433.7 ± 1.8	(35,100)	10.8	(g)
430.8	41	10	(h)
Atmospheric + oceanic excitation			
429.4	107	10	(h)
431.9	83	51	(h)
433.0	97	60	(i)
430.9 ± 0.7	(56, 255)	25	(j)
Semianalytic			
430.3	88.4	20	(k)
433.03	100.20	20	(l)
This work			
432.4 ± 1.0	(41, 74)	43	-

*Reference: (a) Jeffreys (1968); (b) Wilson and Haubrich (1976); (c) Ooe (1978); (d) Wilson and Vicente (1980); (e) Wilson and Vicente (1990); (f) Kuehne et al. (1996); (g) Furuya and Chao (1996); (h) Gross (2005); (i) Seitz et al. (2012); (j) Nastula and Gross (2015); (k) Mathews et al. (2002); (l) Chen and Shen (2010).

Table 2.4 – The Love number $\tilde{k}_2$ derived from the estimated CW period and quality factor in Table 2.2 for the case "seasonal terms excluded".

	$\mathrm{Re}[\tilde{k}_2]$	$\mathrm{Im}[\tilde{k}_2]$
NCEP + ECCO	$(0.306, 0.308)$	$(-0.0058, -0.0027)$
ECMWF + MPIOM	$(0.306, 0.310)$	$(-0.0065, -0.0033)$
ECMWF + MPIOM + LSDM	$(0.305, 0.308)$	$(-0.0071, -0.0039)$

Part II

Retrograde diurnal band

Chapter 3

Nutation theory in the frame of three layers-Earth

The dynamical equation in Chapter 1 is limited to the common polar motion band. For the nutation band, this equation has to be modified: first it has to be extended to a three-layered Earth model (mantle, fluid outer core, and solid inner core) and the excitation process has to be replaced by the lunisolar gravitation torque. By adding the solid inner core, two new resonances appeared: FICN and ICW. The pioneer model developed by Mathews et al. (1991b) was limited in several aspects. Mathews et al. (2002) later refined it by notably including the ocean tide effects, mantle anelasticity and electromagnetic couplings at the fluid core boundaries, yielded the actual nutation reference model (IAU2000), adopted by the International Astronomical Union and the International Union of Geodesy and Geophysics.

3.1 Analytic formulation for the nutation

According to Mathews et al. (2002), the dynamical equation of the retrograde diurnal oscillation forced by the lunisolar tides in frequency domains is written as

$$\mathbf{M}(\sigma)\mathbf{x}(\sigma) = \mathbf{y}(\sigma)\tilde{\phi}(\sigma) . \tag{3.1}$$

Here σ is the frequency in the terrestrial frame, $\mathbf{x} = (\tilde{m}, \tilde{m}_f, \tilde{m}_s, \tilde{n}_s)$ is a four line matrix containing the mantle, outer core and inner core wobbles, and the inner core tilt, $\tilde{\phi}$ is the lunisolar perturbing potential, and $\mathbf{M}$ and $\mathbf{y}$ are four-by-four and four-line matrixes respectively, whose coefficients depend on the geophysical parameters such as ellipticity, Earth moment of inertia, and nine compliances which describe the response of the whole Earth, the outer core, and the inner core to their own respective wobble. The solution $m(\sigma)$ is the first component of $\mathbf{x}(\sigma)$ obtained by inversion of the system (3.1):

$$m(\sigma) = [\mathbf{M}^{-1}(\sigma)\mathbf{y}(\sigma)]_1 \tilde{\phi}(\sigma) . \tag{3.2}$$

Practically, the tidal potential $\tilde{\phi}(\sigma)$ is determined by the rigid Earth nutation. Such models were done, for example, by Roosbeek and Dehant (1998) (RDAN97) and Souchay et al. (1999) (REN2000). More precisely, the dynamical equation of an Earth rigid ("R") model is governed by

$$m_R(\sigma) = \frac{e\,\Omega}{e\,\Omega - \sigma} \tilde{\phi}(\sigma) . \tag{3.3}$$

The kinematic relation between $m(\sigma)$ with its corresponding nutation $\zeta(\sigma)$ described in the terrestrial frame is given by

$$\zeta(\sigma) = -\frac{\Omega}{\Omega + \sigma} m(\sigma) . \tag{3.4}$$

Following Brzeziński and Capitaine (1993), the nutation as seen from the celestial frame is given by

$$\eta(\sigma') = \zeta(\sigma)e^{i\,\Theta(t)} , \tag{3.5}$$

where $\sigma' = \sigma + \Omega$ is the frequency in cycle per day (cpd) as seen from a celestial frame and $\Theta(t)$ is the Earth rotation angle:

$$\Theta(t) = \Theta(t_0) + \Omega(t - t_0), \tag{3.6}$$

where $\Theta(t_0) \approx -79.53^o$ is the rotation angle at the reference time t_0 (12h00 of 1 January 2000).

The ratio between the amplitude of a non-rigid Earth and a rigid Earth is the same for $m(\sigma)$, $\zeta(\sigma)$, and $\eta(\sigma')$:

$$\tilde{T}(\sigma; e) = \frac{\eta(\sigma')}{\eta_R(\sigma')} = \frac{\zeta(\sigma)}{\zeta_R(\sigma)} = \frac{m(\sigma)}{m_R(\sigma)} = \frac{e\,\Omega - \sigma}{e\,\Omega}[\mathbf{M}^{-1}(\sigma)\mathbf{y}(\sigma)]_1 , \tag{3.7}$$

where $\zeta_R(\sigma)$ is the Earth rigid nutation in the celestial frame and $\tilde{T}(\sigma; e)$ is the transfer function. Hence, a given nutation term of frequency σ is modelled by

$$\zeta(\sigma) = \tilde{T}(\sigma; e)\zeta_R(\sigma) . \tag{3.8}$$

Several approximations are needed to expand the transfer function (3.7). It has to be noted that the matrix $\mathbf{M}$ has 4×4 size and therefore the analytical expansion will be very complicated and will not be practical. Mathews et al. (2002) had made several approximations to reach a simpler form of the expansion in the transfer function in function of the rotation modes:

$$\tilde{T}(\sigma; e) = \frac{\zeta(\sigma)}{\zeta_R(\sigma)} = \frac{(e - \sigma/\Omega)}{(e + 1)} \left[1 + (1 + \sigma/\Omega) \left(\frac{-\tilde{\sigma}_1/e}{\sigma - \tilde{\sigma}_1} + \frac{\tilde{N}_2\Omega}{\sigma - \tilde{\sigma}_2} + \frac{\tilde{N}_3\Omega}{\sigma - \tilde{\sigma}_3} \right) \right] . \tag{3.9}$$

Here $\Omega = 1.0027379$ cpd, $\tilde{N}_{(2,3)}$ are complex coefficients and $\tilde{\sigma}_{(1,2,3)}$ are the complex frequencies specifying the resonance modes. These latter ones are put under the form $\tilde{\sigma}_j = 2\pi/P_j (1 + n_j (i / 2Q_j))$, where n_j is '+1' for the prograde and '-1' for the retrograde modes respectively, P_j and Q_j are the corresponding Earth-referred period and quality factor respectively. The indexes 1 until 3 are for representing the resonances associated with PMR, FCN, and FICN respectively. In our study, we ignore the contribution of the ICW since its contribution is negligible to the nutation (Mathews et al., 2002). It should be noted that the PMR parameters are characteristic of the Earth response to the pole tide potential in the retrograde diurnal band, therefore they are not the ones prevailing in the seasonal band of the polar motion, namely the CW parameters. The terrestrial frequencies $\tilde{\sigma}_j$ are mapped into celestial frequencies $\tilde{\sigma}'_j = \tilde{\sigma}_j + \Omega$ with corresponding period and quality factor P'_j and Q'_j.

3.2 Dependence on the basic Earth parameters

Even if (3.9) is an approximate expression of (3.7), it is associated with an analytical (approximate) expressions for all $\tilde{N}_{(2,3)}$ and $\tilde{\sigma}_{(1,2,3)}$ as a function of the aforementioned geophysical parameters. Mathews et al. (2002) provide such expressions for the PMR, FCN and FICN resonance complex frequencies, $\tilde{\sigma}_1$, $\tilde{\sigma}_2$ and $\tilde{\sigma}_3$, and complex coefficients, $\tilde{N}_2$ and $\tilde{N}_3$. Along with the ellipticity e, they have also identified a small set of basic Earth parameters ($\tilde{\kappa}$, $\tilde{\beta}$, $\tilde{\gamma}$, $\tilde{\nu}$, $\tilde{K}^{CMB}$,

$\tilde{K}^{ICB}$, A, A_m, A_f) whose combination can be directly related to the previous frequencies and coefficients:

$$\tilde{\sigma}_1 = \frac{A}{A_m}\left(e - \tilde{\kappa}\right) ,$$

$$\tilde{\sigma}_2 = -\frac{A}{A_m}\left(e_f - \tilde{\beta} + \tilde{K}^{CMB} + \tilde{K}^{ICB}\frac{A_s}{A_f}\right) - \Omega ,$$

$$\tilde{\sigma}_3 = \left(\alpha_2 e_s + \tilde{\nu} - \tilde{K}^{ICB}\right) - \Omega ,$$ (3.10)

$$\tilde{N}_2 = \frac{A_f}{A_m}\left(1 - \frac{\tilde{\gamma}}{e}\right) ,$$

where A, A_m, A_f, and A_s are the mean equatorial moments of inertia of the Earth, the mantle, the fluid outer core, and the solid inner core, respectively, $\tilde{K}^{CMB}$ and $\tilde{K}^{ICB}$ are the electromagnetic coupling constants at the Core-Mantle Boundary (CMB) and Inner-Core Boundary (ICB), $\tilde{\beta}$, $\tilde{\kappa}$, $\tilde{\nu}$, $\tilde{\gamma}$ are the compliance, and α_2 is the coupling constant. The flattenings e_f and e_s are the dynamical ellipticity of the fluid and solid inner cores. The compliance $\kappa = e\,k/k_s$ expresses the deformability at the surface under degree 2 tidal forcing. Moreover, the full expression for $\tilde{N}_3$ can be found in, e.g., Dehant et al. (2005). When estimating the basic Earth parameters from VLBI observation, they appear to be strongly correlated (Rosat et al., 2016), thus it is more robust to consider a restricted number of parameters, namely $\tilde{N}_2$ and $\tilde{\sigma}_{(1,2,3)}$.

Chapter 4

Nutation terms adjustment

VLBI is the only space geodetic technique that can determine the nutation with a sub milliarc-second precision. The principle of VLBI is based on the measurement of the time difference between the arrival of a radio signal, emitted by extra-galactic source in our case, at several VLBI stations (Dehant and Mathews, 2015). Figure 4.1 shows a schematic picture of the VLBI principle. The received signals from several stations are combined by using a so-called correlator. This correlator then produces time delays ($\tau = t_2 - t_1$) as an output. Here τ depends on the length of the distance between the stations $\underline{b}$ and the position of the observed source $\underline{k}$. Mathematically, VLBI time delay is given by

$$\tau = -\frac{\underline{k}.M.\underline{b}}{c} + \Delta\tau .\tag{4.1}$$

Here ($\underline{k}.\underline{b}/c$) is called geometric delay and becomes the dominant factor for the delay, M is the matrix of transformation from terrestrial to celestial frame, and $\Delta\tau$ is the sum of all other time delays, which have much smaller magnitude, caused by the troposphere, ionosphere, atomic clocks synchronization, and measurement noise. VLBI can provide the determination of several parameters such as station positions, source positions, EOP, and sub-daily variations of troposphere zenith delay and clock offsets. The parameters can be estimated over all VLBI sessions, namely global parameters, or for each 24-hour, called local parameters, or even estimated over 60 minute time spans, namely segmented parameters. In VLBI, the desired parameter is calculated by comparing the observed time delay with the modeled one.
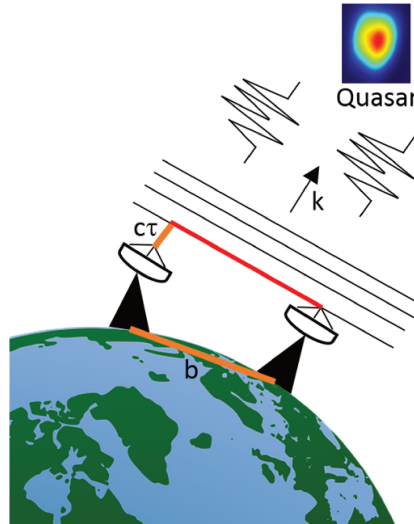
Figure 4.1 – VLBI technique schematic picture.

VLBI determines the nutation by adjusting session-wise nutation offsets (so-called celestial pole offsets: CPO) to an a priori model that is currently IAU2000 model. This model is composed of about two thousand periodic elliptical motions, where the most significant are the 18.6-yr (10"), the semi-annual (1"), the semi-monthly, and the annual terms. Figure 4.2 and 4.3 show the nutation offset determined by VLBI with respect to IAU2000 for its *dX* and *dY* components. The nutation offset time series shows up with an root mean square (RMS) of about 0.2 mas in terms of displacement at the Earth's surface and are composed of several significant periodic signals and the free core nutation, all containing subtle information about the non-rigid Earth response to tidal forcing (Dehant et al., 2003). The analysis of these nutation offset time series can be used to improve the IAU2000 nutation model by (i) correcting the amplitudes of the Poisson series and, more interestingly, by (ii) adjusting the basic Earth parameters of the underlying geophysical model used in IAU2000 (see, e.g., Koot et al., 2008; Rosat and Lambert, 2009; Rosat et al., 2016; Dehant et al., 2017).
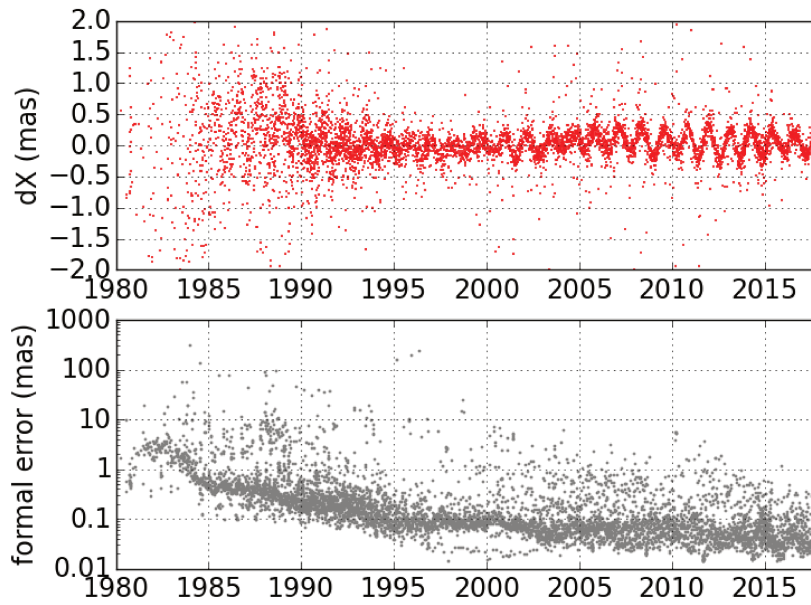
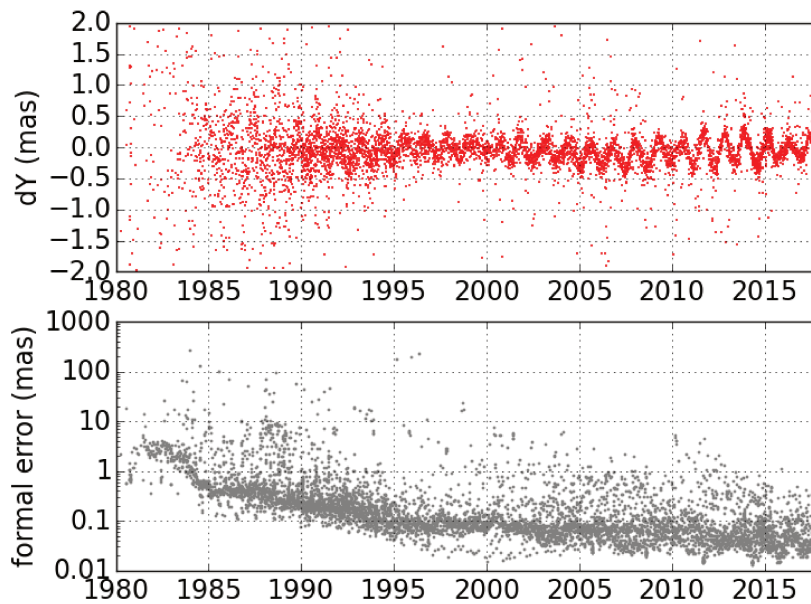Figure 4.2 – Observed dX component from VLBI and its formal error (1σ).

Figure 4.3 – Observed dY component from VLBI and its formal error (1σ).

4.1 Indirect versus direct approaches

The nutation offset (dX, dY) is composed by several harmonic terms, reflecting the defects of the modelled lunisolar components. At a given frequency, they can be represented by the sum of a prograde and retrograde uniform circular motions, formulated by

$$dX + i\,dY = \sum_j \left(A_j^+ e^{i\theta_j(t)} + A_j^- e^{-i\theta_j(t)} \right) + a\,t + b \,, \tag{4.2}$$

where $\theta_j(t)$ are the frequency associated with periodical motion of the Moon and the Sun, which is generally given by a linear combination of the five Delaunay arguments: l, l', F, D, and Ω (see A.3), and a and b are the complex coefficients of the linear term modelling the defect of the precession model. Here $A_j^{+/-} = A_{IP,j}^{+/-} + iA_{OP,j}^{+/-}$ are the nutation components, where IP and OP denote in-phase and out-of-phase respectively.

   The common way to estimate the nutation components relies on least square analysis of the nutation offset time series that are produced by the analysis of a complete VLBI observational database (see, e.g., Herring et al., 2002; Koot et al., 2008; Rosat and Lambert, 2009; Rosat et al., 2016). This approach will be referred as indirect approach in the following since it needs two steps: one global VLBI analysis to produce nutation offset time series plus one specific analysis for estimating the nutation offset terms. Here we aim at evaluating the performance of the direct approach which has been developed by Himwich and Harder (1988) and Petrov (2007). The nutation components are estimated directly from VLBI delays, short-cutting, therefore, the traditional two-step approach. Also, it allows a rigorous propagation of the delay errors into the estimated parameters and the use of the full covariance information from the nutation components as well as the other parameters.

4.2 Data processing

In order to apply the direct approach, we need to express the partial derivatives of the group delay τ in (4.1) with respect to the CPO amplitudes $A_j^{+/-}$. These partial derivatives read

$$\frac{\partial \tau}{\partial A_j^{+/-}} = c^{-1} \cdot \underline{k} \cdot \frac{\partial M}{\partial A_j^{+/-}} \cdot \underline{b} \,, \tag{4.3}$$

where matrix M can be represented as

$$M = Q(X, Y)R(-\Theta)W(x_p, y_p) ,\qquad(4.4)$$

with x_p and y_p are the polar motion, and X and Y are the nutation (i.e., the nutation-precession model plus the CPO). Matrix Q can be decomposed as

$$Q(X, Y) = dQ(dX, dY).Q(X_{\text{IAU 2000A}}, Y_{\text{IAU 2000A}}) ,\qquad(4.5)$$

where

$$dQ(dX, dY) = \begin{bmatrix} 0 & 0 & dX \\ 0 & 0 & dY \\ -dX & -dY & 0 \end{bmatrix} .$$

The derivation of dQ with respect to the IP and OP components of $A_j^{+/-}$ gives

$$\frac{\partial dQ}{\partial A_{\text{IP},j}^+} = \begin{bmatrix} 0 & 0 & \cos\theta_j(t) \\ 0 & 0 & \sin\theta_j(t) \\ -\cos\theta_j(t) & -\sin\theta_j(t) & 0 \end{bmatrix} ,$$

$$\frac{\partial dQ}{\partial A_{\text{OP},j}^+} = \begin{bmatrix} 0 & 0 & -\sin\theta_j(t) \\ 0 & 0 & \cos\theta_j(t) \\ \sin\theta_j(t) & -\cos\theta_j(t) & 0 \end{bmatrix} ,$$

and

$$\frac{\partial dQ}{\partial A_{\text{IP},j}^-} = \begin{bmatrix} 0 & 0 & \cos\theta_j(t) \\ 0 & 0 & -\sin\theta_j(t) \\ -\cos\theta_j(t) & \sin\theta_j(t) & 0 \end{bmatrix} ,$$

$$\frac{\partial dQ}{\partial A_{\text{OP},j}^-} = \begin{bmatrix} 0 & 0 & \sin\theta_j(t) \\ 0 & 0 & \cos\theta_j(t) \\ -\sin\theta_j(t) & -\cos\theta_j(t) & 0 \end{bmatrix} .$$

We applied this modeling to find the corrections of 21 prograde and 21 retrograde nutation terms yielded in Herring et al. (2002) and Mathews et al. (2002). These specific terms are the terms

that could be reliably estimated. Even though IAU2000 has 678 lunisolar nutation terms, some components are so close to each others, thus the estimates of all components will not be reliably obtained (Herring et al., 2002).

The nutation terms are estimated from the data consists of 6246 VLBI sessions between August 1979 to December 2017. This data is taken from the IVS data center. We used the geodetic analysis software Calc/Solve (Ma et al., 1986) developed and maintained by the VLBI group at NASA/GFSC[1] in a standard configuration. We estimated the station coordinate differences with respect to ITRF2014 (Altamimi et al., 2016) as global parameters with no-net rotation and no-net translation conditions applied to the positions and velocities of a group of 38 stations. All of the a-priori station positions were corrected from tridimensional displacements due to oceanic and atmospheric tidal loading using FES2004 (Lyard et al., 2006) and the output from the inverted-barometer version of the Atmospheric Pressure Loading Service (APLO; Petrov and Boy, 2004) as well as corrections for the post-seismic relaxation for relevant stations as given in the ITRF2014. Radio source coordinates were estimated as global parameters for most of the sources except a set of 39 particularly active quasars (tagged as special-handling sources in the ICRF2 work, Fey et al., 2015) whose coordinates were estimated once per session. A no-net rotation condition was applied to the 295 ICRF2 defining sources. Antenna thermal deformations were obtained in Nothnagel (2009). A-priori dry zenith delays were estimated from local pressure values and then mapped to the elevation using the Vienna Mapping Function (Böhm et al., 2006). The modeling of intraday variations of the troposphere wet delay, clocks, and troposphere gradients is realized through continuous piecewise linear functions whose coefficients are estimated every 10 min, 30 min, and 6 hours, respectively. A-priori Earth orientation parameters were taken from the IERS EOP 14 C04 data associated with the IAU2000/2006 nutation and precession models (Mathews et al., 2002; Capitaine et al., 2003). Offsets to the polar motion and UT1 a-priori, together with polar motion and UT1 rates, were estimated once per session.

---

[1]https://vlbi.gsfc.nasa.gov.

4.3   Free Core Nutation

The FCN is the dominant contributor to the nutation offset. Its period can be considered as strongly constrained by the fluid core properties (Mathews et al., 2002). Its amplitude and phase, likely driven by surface fluid dynamics, remain unpredictable (Chao and Hsieh, 2015), and still need to be accounted for by empirical modeling that does not address, however, the underlying physics.
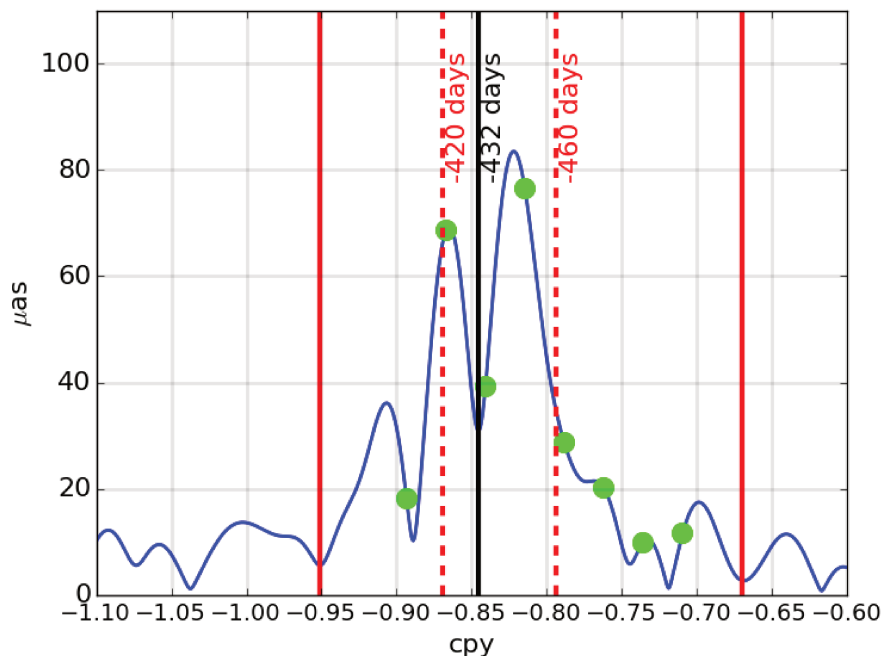

Figure 4.4 – The FFT spectrum of the nutation offset around the FCN frequency. The red vertical lines indicates suggested limits of the FCN broad peak. The chosen frequencies are shown by green dots.

As shown in Figure 4.4, the FCN appears as a broad band spectral process (e.g., Vondrák et al., 2005; Chao and Hsieh, 2015), hinting that its amplitude and phase are variable. The spectrum of Figure 4.4 was obtained by FFT of the nutation offset series regularized at 10 day intervals by a running average, and padded with zeros to get 2^{12} points. It suggests that the power relevant to the FCN lies between approximately -0.95 and -0.67 cpy, i.e., -386 to -545

days. This large band contains the periods of the two 'extreme' peaks at −420 days and −460 days showed by Fast Fourier Transform (FFT) spectra realized over different time spans by Chao and Hsieh (2015) and earlier with little differences by Vondrák et al. (2005).

Table 4.1 – The FCN complex amplitudes estimated by the direct and indirect approaches. Unit is μas.

Period	Indirect			Direct		
	IP	OP	±	IP	OP	±
-408.58	64.2	-24.1	2.7	58.1	-20.7	1.3
-420.97	-87.5	107.9	3.6	-81.4	102.4	1.8
-434.12	49.8	-64.1	4.3	44.1	-54.3	2.1
-448.12	21.6	-60.8	4.6	22.1	-69.1	2.3
-463.06	-46.2	-29.6	4.5	-43.0	-20.0	2.2
-479.03	0.5	-10.8	4.1	-8.3	-17.2	2.0
-496.14	-6.4	6.4	3.5	3.4	6.4	1.7
-514.51	3.5	-9.9	2.6	-3.5	-6.3	1.3

Several empirical models of the FCN have been obtained by different methods (least-squares fit over sliding windows, wavelet decomposition, Singular Spectral Analysis) in the recent years, all being generally in good agreement (Malkin, 2007; Krásná et al., 2013; Belda et al., 2016). A direct adjustment of the FCN usually has been made via a sliding window, by selecting a subset of data similarly to what is done in the indirect approach. However, as the window is restricted to some years, the sliding window method introduces correlations with other nutation terms. Here, we propose the adjustment of an empirical harmonic model composed of close frequencies for representing the broad band spectral peak in according to

$$\mathrm{d}X_{\mathrm{FCN}} + i\,\mathrm{d}Y_{\mathrm{FCN}} = \sum_j A_{\mathrm{FCN},j} e^{i\sigma'_{\mathrm{FCN},j}t} \,, \tag{4.6}$$

where $A_{\mathrm{FCN},j}$ is the complex amplitude of the jth FCN component, and $\sigma'_{\mathrm{FCN},j}$ is its frequency.

We found that eight equally-spaced frequencies within the interval $[-0.95, -0.67]$ cpy describe at best the FCN over the period 1979-2018, in the sense that a more dense model does not drop significantly the residuals. Then, the $A_{\mathrm{FCN},j}$ parameters are estimated by the direct and indirect approaches. In contrast to estimates obtained by the sliding window adjustment, the formulation (4.6) constitutes a compact description that can be extrapolated into the future. The corresponding results are reported in Table 4.1 and Figure 4.5. It matches the estimates obtained by the more traditional sliding-window approach within one sigma standard errors, except before 1985 and after 2016, where the sliding window results are perturbed by a 3.5 year edge effect.
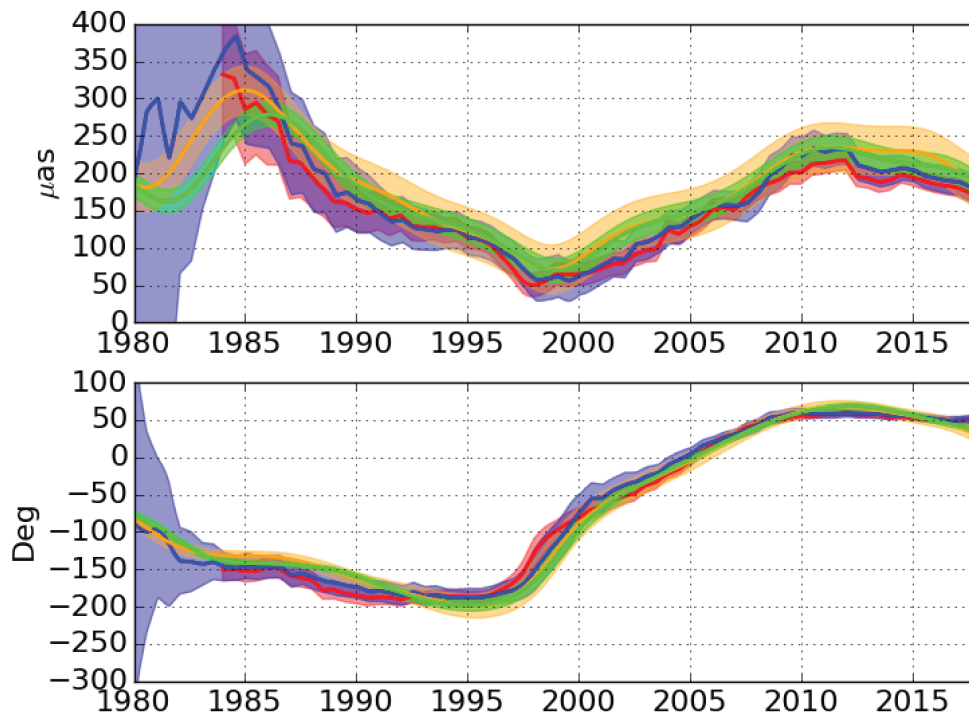

Figure 4.5 – The amplitude (*top*) and phase (*bottom*) of the FCN in time domain. Here — corresponds to 7-year sliding window by using C04 series, — is 7-year sliding window from VLBI data, — is the harmonic model from the indirect approach, and — is a harmonic model from the direct approach. The thinner color corresponds to their 3σ.

4.4 Results and comparison between the direct and indirect approaches

The corresponding estimates of 42 nutation offset terms for both the indirect and the direct approaches are shown in Table 4.2. The largest differences between the two approaches reside in the long period terms (18.6-yr and 9.3-yr) for which the complex amplitude change is larger than 10 μas. The direct approach returned a χ^2 per degree of freedom of 0.94 whereas the indirect approach has χ^2 per degree of freedom 3.99. The direct approach provides formal errors that are smaller than for the indirect approach by a factor of two to three. Here the formal errors are produced from the multiplication of the co-variance matrix's diagonal elements with the root square of χ^2. The correlations between the various estimated complex amplitudes are reported in Figure (4.6 and 4.7). The direct approach permits to lower the correlations between the 18.6-yr and 9.3-yr terms, and between the 6.86-d and 346.64-d terms by 5% and 10%. For the other terms, there are only marginal changes of correlation between the two approaches. On average, the direct approach permits to lower the correlation by 7%.

The solutions associated with the indirect and direct approaches produced obviously different Earth rotation parameters and radio source positions, raising the question to which extent these differences are significant. The RMS differences in polar motion remain within 0.03 mas. We reached the same conclusions for UT1 and length-of-day with RMS differences of about 1 ms. The median errors for the polar motion are slightly lower (by 2 μas) in the direct approach with respect to the indirect approach. The celestial reference frames obtained from the two approaches and composed of 4118 radio sources were compared in terms of global rotation and deformations up to degree 2 (see, e.g., Mignard and Klioner, 2012). They only differ by small rotations of less than 3 μas. The modeling of nutation in the direct approach has, therefore, no significant impact on the other EOP and the celestial reference frame.

The robustness of the results are examined by estimating the nutation components from two session lists which have approximately the same number of observations. We divided the session list into two lists by taking the "even" and "odd" sessions of the initial list in chronological order. For the long periods, the nutation amplitudes are not expected to be so sensitive to the

number of observation being divided by two. For short periods (few times the mean sampling rate), one could expect an increased sensitivity due to the rapidly changing network characteristics (size, geometry, data quality) for one session to another. We found that the "even" and "odd" solutions return a χ^2 per degree of freedom which are in a good agreement with the initial session list. Figure (4.8, 4.9, 4.10, 4.11) show the differences between the results from "even" and "odd" sessions in each nutation component for both the direct and indirect approaches. It shows that the differences are larger in the indirect approach, with an average value of 3.0 μas, than the direct approach, with an average value of 2.4 μas. The dispersion of the results between the even and odd session can be interpreted as an "empirical error". Such error appear much less homogeneous than the initial standard error when contrasted with the frequency. The less robust nutation are generally short-period nutation (e.g., 13.78 days). But the empirical error does not decrease as the period increases: a possible reason for this is the in-homogeneity of the VLBI data quality and error along the observational period, especially the early data (before 1990) compared with the more recent ones.

Table 4.2 – In-phase and out-phase coefficients of 42 nutation terms estimated by the indirect and direct approaches. Here the period is given with respect to the celestial frame. Unit is day for periods and μas for the coefficients.

| l	l'	F	D	Ω		Indirect			Direct		
a_1	a_2	a_3	a_4	a_5	Period	IP	OP	$\pm$	IP	OP	$\pm$
0	0	0	0	1	-6798.38	26.2	-15.7	1.7	30.8	-26.9	0.9
0	0	0	0	-1	6798.38	2.8	-33.2	1.7	15.2	-32.8	0.9
0	0	0	0	2	-3399.19	7.3	-13.1	1.7	3.0	-10.9	0.9
0	0	0	0	-2	3399.19	20.2	-17.2	1.7	14.1	-11.5	0.9
2	0	-2	0	-2	-1615.75	-0.8	-2.2	1.7	-5.3	-5.7	0.8
-2	0	2	0	2	1615.75	-1.8	-12.8	1.7	2.6	-8.0	0.8
2	0	-2	0	-1	-1305.48	-0.9	10.0	1.7	-3.6	8.8	0.9
-2	0	2	0	1	1305.48	-5.2	1.5	1.7	-4.0	3.3	0.8
2	0	-2	0	0	-1095.18	-3.4	4.8	1.7	1.1	4.1	0.8
-2	0	2	0	0	1095.18	-4.1	6.1	1.7	-4.1	1.1	0.8
0	-1	0	0	-1	-386.00	-9.7	1.5	1.9	-9.1	-4.5	0.9
0	1	0	0	1	386.00	-1.0	-1.2	1.6	0.6	-0.0	0.8
0	-1	0	0	0	-365.26	35.7	4.5	1.8	33.5	7.6	0.9
0	1	0	0	0	365.26	-4.1	-0.2	1.7	-9.7	-0.8	0.8
0	-1	0	0	1	-346.64	-16.2	-2.8	1.8	-13.3	0.8	0.9
0	1	0	0	-1	346.64	1.3	-0.0	1.7	-0.0	-3.0	0.9
0	0	-2	2	-2	-182.62	-11.5	5.5	1.5	-12.6	5.9	0.8
0	0	2	-2	2	182.62	7.8	-5.7	1.5	9.0	-4.3	0.8
0	-1	-2	2	-2	-121.75	-4.2	4.7	1.5	-1.7	4.4	0.8
0	1	2	-2	2	121.75	4.6	1.4	1.6	3.8	-1.2	0.8
1	0	0	-2	0	-31.81	0.8	-3.9	1.5	0.7	-2.8	0.7
-1	0	0	2	0	31.81	-2.0	2.6	1.5	-3.2	2.8	0.8
-1	0	0	0	0	-27.55	-17.6	-9.4	1.5	-17.8	-7.6	0.7
1	0	0	0	0	27.55	1.1	-3.9	1.5	1.0	-2.6	0.8
-1	0	-2	2	-2	-23.94	-0.6	-1.4	1.5	-0.9	-0.2	0.7
1	0	2	-2	2	23.94	-0.8	-1.1	1.5	-1.9	-0.7	0.8
0	0	0	-2	0	-14.77	-3.1	2.2	1.5	-1.9	2.4	0.7
0	0	0	2	0	14.77	1.0	-0.0	1.5	1.3	-0.9	0.8
-2	0	0	0	0	-13.78	-2.4	-2.0	1.5	-2.4	-1.4	0.7
2	0	0	0	0	13.78	1.4	1.1	1.5	0.5	0.4	0.8
0	0	-2	0	-2	-13.66	-6.7	-7.7	1.5	-8.5	-5.6	0.7
0	0	2	0	2	13.66	-3.4	9.0	1.5	-5.6	8.6	0.8
1	0	-2	-2	-2	-9.56	-0.9	-3.7	1.5	-1.7	-1.5	0.7
-1	0	2	2	2	9.56	3.0	-3.7	1.5	2.0	-1.1	0.8
-1	0	-2	0	-2	-9.13	-1.2	1.1	1.6	-1.5	1.5	0.7
1	0	2	0	2	9.13	-1.3	3.8	1.6	-3.3	5.7	0.9
-1	0	-2	0	-1	-9.12	2.1	4.2	1.6	2.2	3.7	0.7
1	0	2	0	1	9.12	1.5	-0.9	1.6	1.4	-1.6	0.9
0	0	-2	-2	-2	-7.10	-3.8	-1.2	1.5	-5.0	0.5	0.7
0	0	2	2	2	7.10	1.4	1.9	1.7	-1.3	2.3	1.0
-2	0	-2	0	-2	-6.86	1.3	-0.1	1.6	0.2	-0.6	0.7
2	0	2	0	2	6.86	-1.3	2.9	1.6	-2.1	6.4	0.9
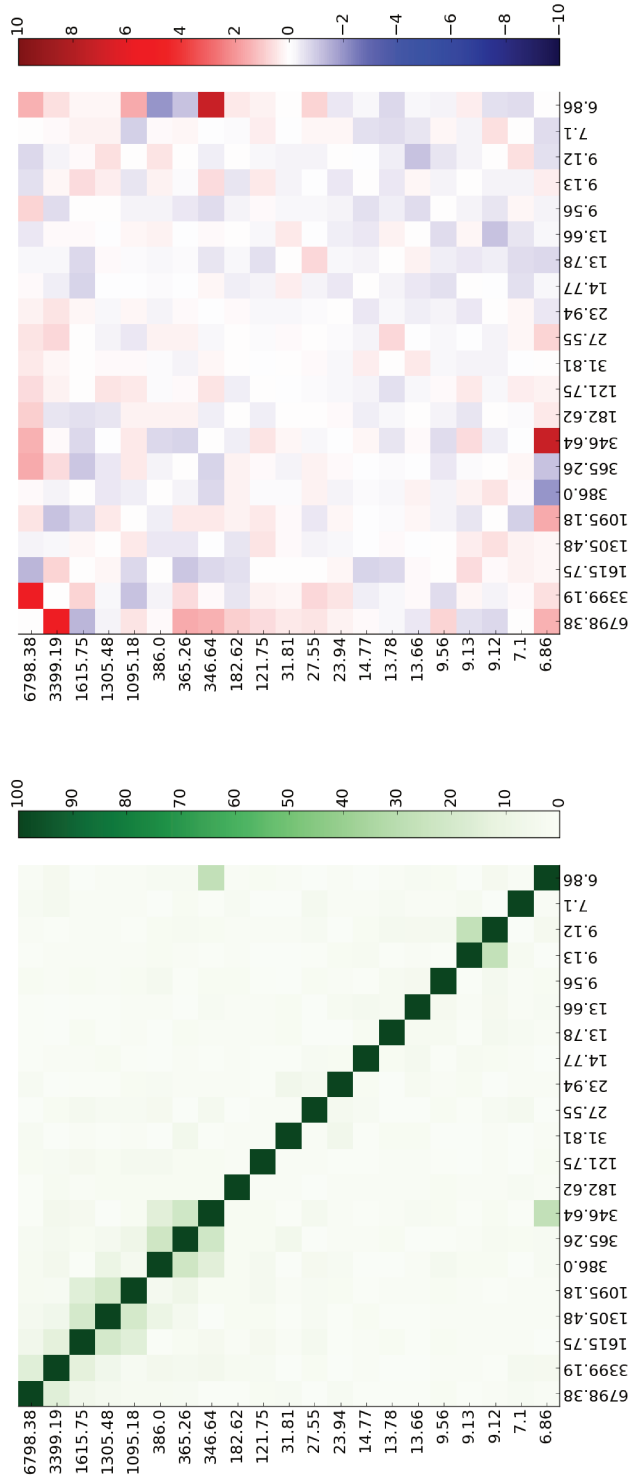
Figure 4.6 – (*Left*) The absolute correlation coefficients between several in-phase and out-phase amplitudes of prograde terms for the indirect approach. (*Right*) The absolute correlation coefficients of the indirect approach minus the absolute correlation coefficients of the direct approaches for prograde terms. A positive value means that the correlation is diminished when using the direct approach. The unit of correlation is in (%).
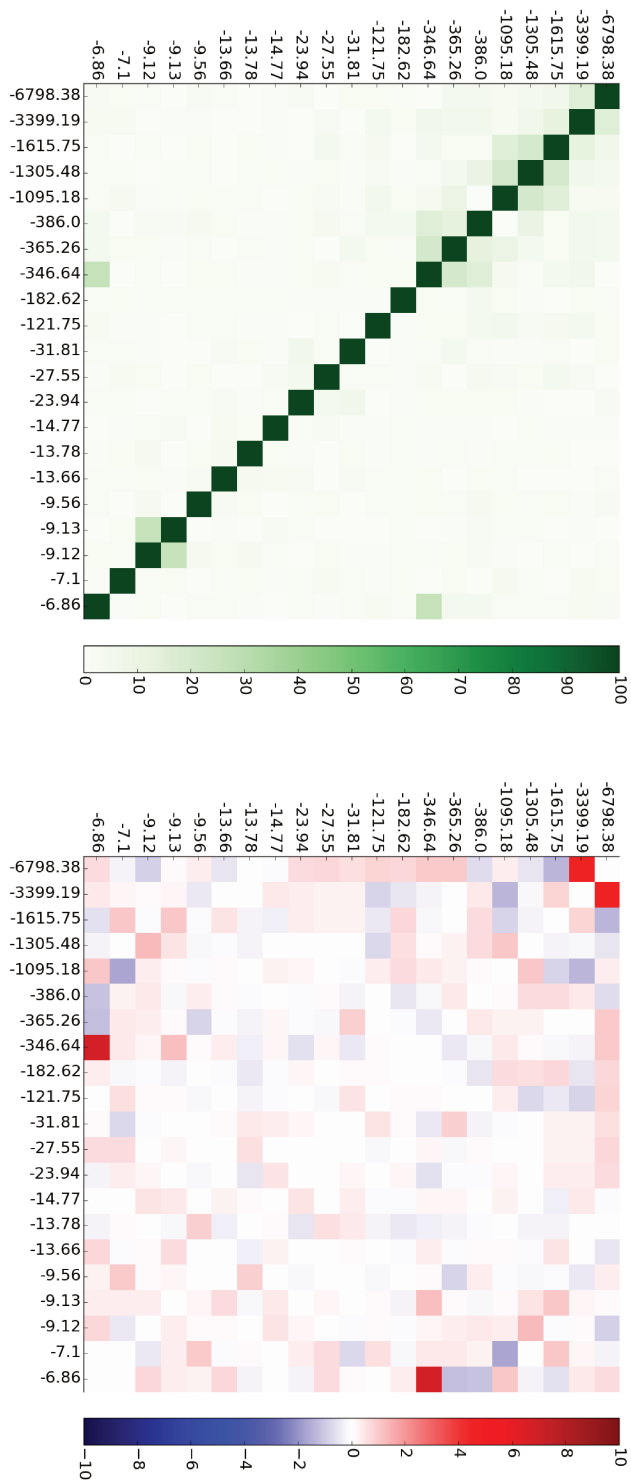
Figure 4.7 – (*Left*) The absolute correlation coefficients between several in-phase and out-phase amplitudes of retrograde terms for the indirect approach. (*Right*) The absolute correlation coefficients of the indirect approach minus the absolute correlation coefficients of the direct approaches for retrograde terms. A positive value means that the correlation is diminished when using the direct approach. The unit of correlation is in (%).
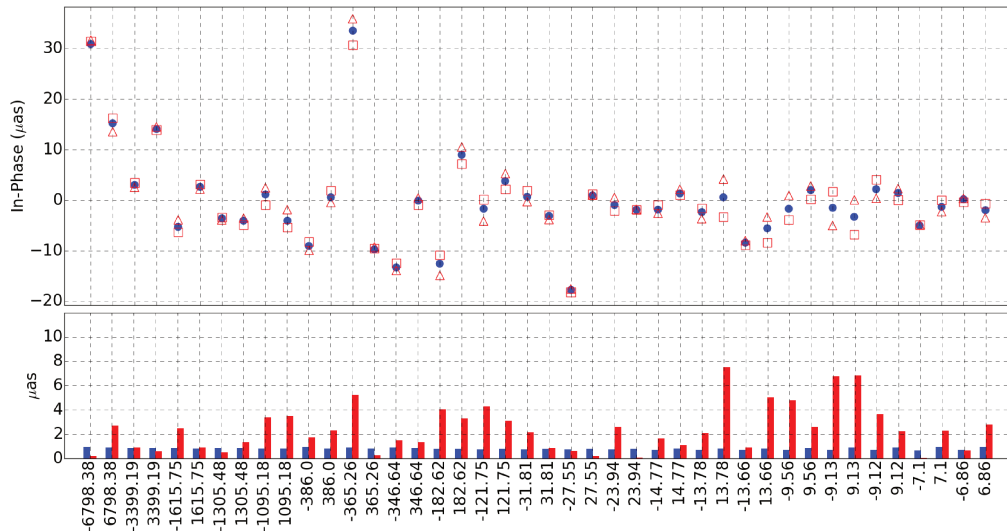
Figure 4.8 – The in-phase amplitudes of nutation components estimated by the direct approach. Here ● corresponds to the nutation terms from all VLBI sessions and △ and □ are the nutation terms from even and odd sessions respectively. The blue bars correspond to the formal error of ● and the red bars are the different between the nutation terms from odd and even sessions.

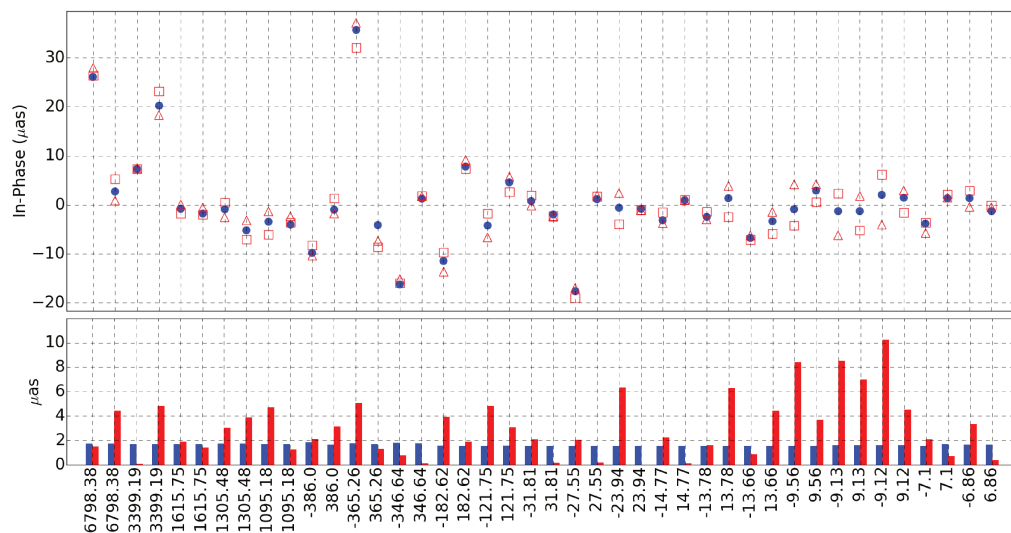Figure 4.9 – The in-phase amplitudes of nutation components estimated by the indirect approach. The detail of the figure is similar with Figure 4.8
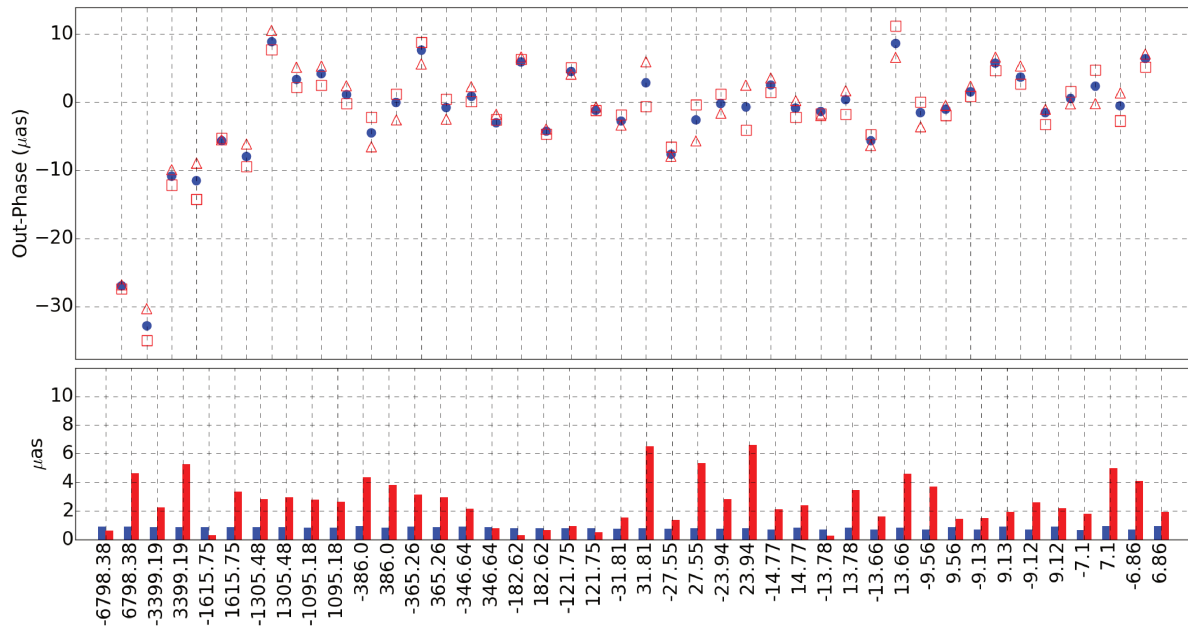
Figure 4.10 – The out-phase amplitudes of nutation components estimated by the direct approach. The detail of the figure is similar with Figure 4.8
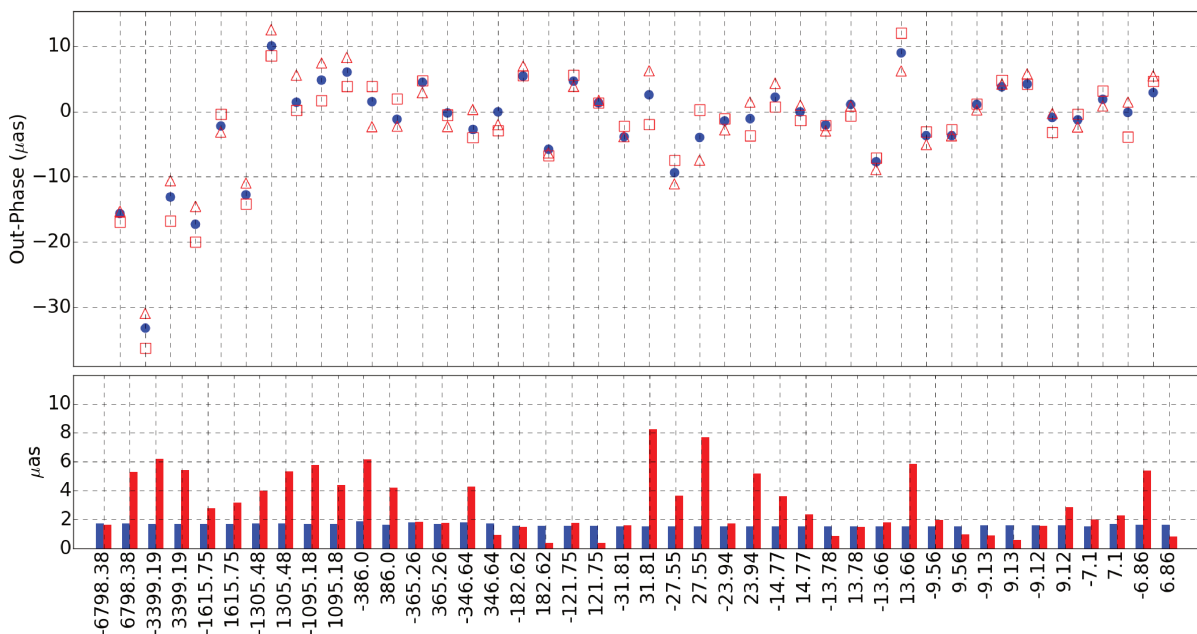

Figure 4.11 – The out-phase amplitudes of nutation components estimated by the indirect approach. The detail of the figure is similar with Figure 4.8

Chapter 5

Resonances adjustment in retrograde diurnal band

In order to estimate the Earth resonance parameters through VLBI data, in a first approach, we strictly follow the procedure of Mathews et al. (2002). It is based on a transfer function (3.9) that expresses the ratio between the non-rigid Earth nutation terms and its corresponding rigid Earth nutation. Here, we adopt the value $e = 3.2845479 \times 10^{-3}$, as reported in Mathews et al. (2002). The observed nutation $\eta(\sigma')$ is estimated by adding up the nutation offset terms of Table 4.2 to the corresponding IAU2000 nutation model (see Table 5.1 column 9 and 10). The rigid Earth nutation is adopted from REN2000 model (Souchay et al., 1999), as reported in Table 5.1 column 7 and 8.

We estimate the complex parameters $\tilde{\sigma}_j$ and $\tilde{N}_2$ by performing a weighted least square inversion. As $\tilde{N}_3$ is correlated with $\tilde{\sigma}_3$, $\tilde{N}_3$ is fixed to its theoretical value ($2.95844 \times 10^{-4} - i9.57705 \times 10^{-5}$) as given by Mathews et al. (2002). The weights of the nutation terms itself are deduced from the formal error displayed in Table 4.2. As mentioned by Mathews et al. (2002), before the inversion is performed, some corrections have to be applied. First, the nutation terms have to be referred to a dynamical celestial reference frame by removing the geodetic nutation. Then, non-linear effects are suppressed (see Table 5.2). Finally we eventually get rid of the atmospheric-oceanic contribution, which cannot be related to the rigid Earth nutation caused by lunisolar tides.

Table 5.1 – In-phase and out-phase coefficients of 42 nutation terms for a rigid Earth model REN2000 and a non-rigid three-layered Earth model IAU2000. Here the period is given with respect to the celestial frame. The Units are in day for the periods and mas for the coefficients.

| l | l' | F | D | Ω | | REN2000 | | IAU2000 | |
a_1	a_2	a_3	a_4	a_5	Period	IP	OP	IP	OP
0	0	0	0	1	-6798.38	-8050.87	-0.07	-8024.77	-1.43
0	0	0	0	-1	6798.38	-1177.04	-0.08	-1180.46	0.10
0	0	0	0	2	-3399.19	86.74	-0.00	86.14	0.03
0	0	0	0	-2	3399.19	3.59	0.00	3.61	-0.00
2	0	-2	0	-2	-1615.75	-0.00	0.00	-0.00	0.00
-2	0	2	0	2	1615.75	-0.13	0.00	-0.13	0.00
2	0	-2	0	-1	-1305.48	0.31	0.00	0.30	0.00
-2	0	2	0	1	1305.48	2.10	0.00	2.12	-0.00
2	0	-2	0	0	-1095.18	0.22	0.00	0.21	0.00
-2	0	2	0	0	1095.18	-0.22	0.00	-0.22	0.00
0	-1	0	0	-1	-386.00	-0.10	0.00	-0.15	-0.00
0	1	0	0	1	386.00	-0.69	0.00	-0.71	0.00
0	-1	0	0	0	-365.26	-24.89	0.00	-33.05	-0.33
0	1	0	0	0	365.26	25.03	0.00	25.66	-0.13
0	-1	0	0	1	-346.64	-0.46	0.00	-0.57	-0.00
0	1	0	0	-1	346.64	-0.07	0.00	-0.07	0.00
0	0	-2	2	-2	-182.62	-22.59	0.00	-24.56	0.04
0	0	2	-2	2	182.62	-530.74	0.00	-548.47	0.50
0	-1	-2	2	-2	-121.75	-0.88	0.00	-0.94	0.00
0	1	2	-2	2	121.75	-20.74	0.00	-21.50	0.02
1	0	0	-2	0	-31.81	-2.88	0.00	-3.06	0.01
-1	0	0	2	0	31.81	3.07	0.00	3.18	-0.00
-1	0	0	0	0	-27.55	-12.99	0.00	-13.81	0.04
1	0	0	0	0	27.55	13.96	0.00	14.48	-0.00
-1	0	-2	2	-2	-23.94	0.05	0.00	0.05	-0.00
1	0	2	-2	2	23.94	1.14	0.00	1.19	0.00
0	0	0	-2	0	-14.77	-1.12	0.00	-1.20	0.00
0	0	0	2	0	14.77	1.28	0.00	1.32	0.00
-2	0	0	0	0	-13.78	-0.51	0.00	-0.55	0.00
2	0	0	0	0	13.78	0.59	0.00	0.61	0.00
0	0	-2	0	-2	-13.66	-3.40	0.00	-3.65	0.01
0	0	2	0	2	13.66	-91.52	0.00	-94.20	-0.12
1	0	-2	-2	-2	-9.56	-0.08	0.00	-0.09	0.00
-1	0	2	2	2	9.56	-2.41	0.00	-2.46	-0.00
-1	0	-2	0	-2	-9.13	-0.42	0.00	-0.46	0.00
1	0	2	0	2	9.13	-12.19	0.00	-12.45	-0.03
-1	0	-2	0	-1	-9.12	-0.27	0.00	-0.29	0.00
1	0	2	0	1	9.12	-2.30	0.00	-2.34	-0.01
0	0	-2	-2	-2	-7.10	-0.05	0.00	-0.06	0.00
0	0	2	2	2	7.10	-1.57	0.00	-1.59	-0.00
-2	0	-2	0	-2	-6.86	-0.04	0.00	-0.04	0.00
2	0	2	0	2	6.86	-1.26	0.00	-1.28	-0.01

Table 5.2 – Correction to the observed nutation terms, as reported in Table 7 of Mathews et al. (2002). Here the period is given in days and with respect to the celestial frame.

| l | l' | F | D | Ω | | Geodesic | | Non-linear | |
a_1	a_2	a_3	a_4	a_5	Period	IP	OP	IP	OP
0	0	0	0	1	-6798.38	0.0013	-	0.0037	-
0	0	0	0	-1	6798.38	0.0001	-	-0.0336	-
0	0	0	0	2	-3399.19	-	-	-0.0022	-
0	0	0	0	-2	3399.19	-	-	-0.0002	-
0	-1	0	0	0	-365.26	0.0304	-	-	-
0	1	0	0	0	365.26	-0.0304	-	-	-
0	0	-2	2	-2	-182.62	0.0004	-	-	-
0	0	2	-2	2	182.62	-0.0004	-	-	-

5.1 Atmospheric-oceanic contribution

The analysis done in Mathews et al. (2002) was restricted to the atmospheric effect on the annual prograde nutation. Actually, a more complete treatment of the fluid layer perturbations has to include other nutation components (-365 d, $+182.6$ d, $+121.75$ d, $+13.66$ d) and consider the contribution of the non-tidal circulation in the ocean. The atmospheric and oceanic effects are computed by using the effective angular momentum function as explained in Chapter 2. However, as the nutation is estimated in the celestial reference frame, the straightforward approach is to transform this angular momentum function from terrestrial reference frame to celestial reference frame as follows

$$\xi(t) = -\chi^{eff}(t)e^{i\Theta(t)} \, , \tag{5.1}$$

where $\Theta(t)$ is the rotation angle defined in (3.6). Here we used the NIB version of atmospheric effective angular momentum time series from TU Vienna[1] (based on ECMWF model) (Schindelegger et al., 2011) and oceanic effective angular momentum series from ERA40 and opECMWF (Dobslaw and Thomas, 2007) starting from 1984 to 2017. Table 5.3 shows the synopsis of the data used in this Chapter. Following Bizouard et al. (1998), we first remove the mean from the effective angular momentum time series. This time series is then transformed

---

[1] ftp://ftp.iers.org/products/geofluids.

to the celestial effective angular momentum by using (5.1). Low-pass Gaussian filter is then applied with FWHM 0.025 yr for removing the short period terms. The data are then resampled 6 day step, corresponding approximatively to the time resolution of CPO. Finally, we obtain the celestial effective angular momentum function for atmosphere and ocean displayed in Figure 5.1 and 5.2.
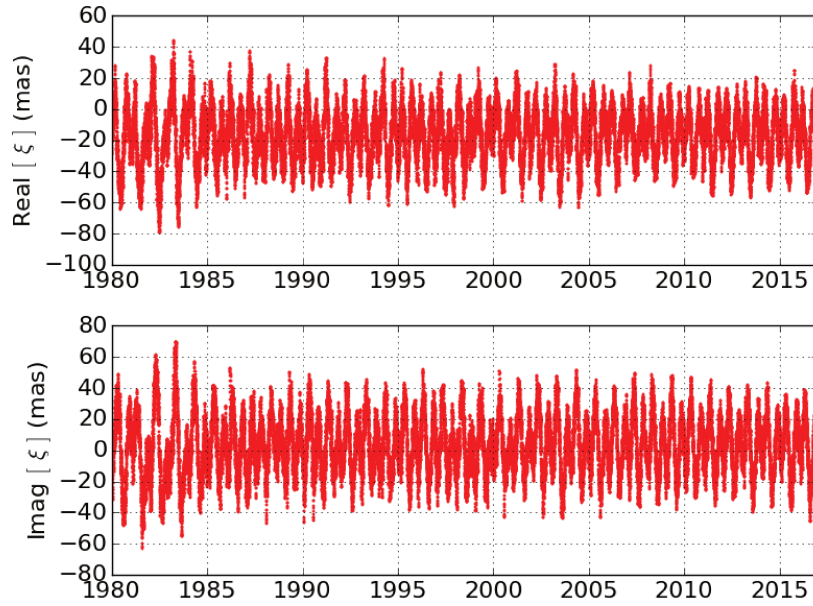

Figure 5.1 – The time series of atmospheric celestial effective angular momentum function.

We decompose $\xi(t)$ into the five most dominant oscillation terms, namely prograde and retrograde annual, prograde semi annual, prograde 1/3 annual and prograde 13.6 day. This decomposition is done either for the mass or motion terms as follows:

$$\xi_{(ma/mo)}(t) = \sum_{j=1}^{5} \left(\xi_{(ma/mo;\,j)}^{ip} + i\xi_{(ma/mo;\,j)}^{op} \right) e^{i(\sigma_j t + \phi_j)} \,, \tag{5.2}$$

where $\xi_{(ma/mo;\,j)}^{ip}$, $\xi_{(ma/mo;\,j)}^{op}$ are real and imaginary components of the oscillation terms.

Following Brzeziński (1994), the contribution to the nutation is calculated by multiplying the harmonic terms of (5.2) with the transfer function:

$$\eta_{fluid}(\sigma') = T(\sigma')_{ma}\xi_{ma}(\sigma') + T(\sigma')_{mo}\xi_{mo}(\sigma') \,, \tag{5.3}$$
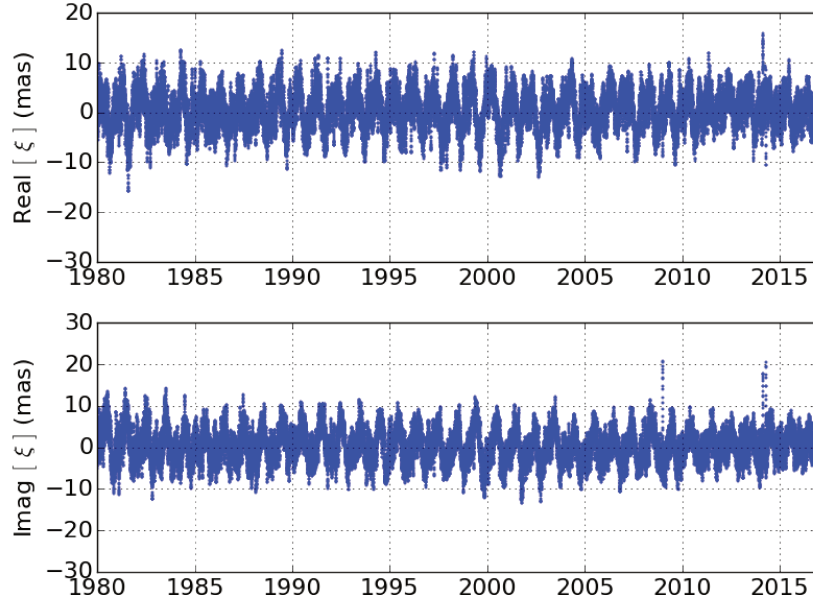
Figure 5.2 – The time series of oceanic celestial effective angular momentum function

where

$$T(\sigma')_{(ma/mo)} = \tilde{\sigma}_{CW}\Big[\frac{1}{\tilde{\sigma}'_{PMR} - \sigma'} + \frac{a_{(ma/mo)}}{\tilde{\sigma}'_{FCN} - \sigma'}\Big] \,. \tag{5.4}$$

Here σ' is the nutation angular frequency in the celestial frame, $\tilde{\sigma}'_{PMR}$ is the celestial angular frequency of the PMR in retrograde diurnal band, $\tilde{\sigma}_{CW}$ is the CW angular frequency, $\tilde{\sigma}'_{FCN}$ is the angular frequency of FCN, and $a_{(ma/mo)}$ are the dimensionless coefficients with $a_{ma} = 9.8 \times 10^{-2}$ and $a_{mo} = 2.6 \times 10^{-4}$ (Bizouard, 2014). The corresponding contribution of the fluid layers to the nutation is reported in Table 5.4.

Table 5.3 – Synopsis of geophysical excitation and observed nutation used in this section.

	model or series name	version	available data	sampling interval
Atmosphere	ECMWF	TU Vienna	1980 - 2019	6 hours
Ocean	OMCT	ERA40	1958 - 2001	6 hours
	OMCT	opECMWF	2001 - 2017	6 hours
Nutation	VLBI		1979 - 2019	varied

Table 5.4 – Non-tidal atmospheric and oceanic contribution to the nutation circular terms. Unit is μas. Here the period is given in the celestial frame.

Period (days)	Atmosphere			Ocean		
	IP	OP	±	IP	OP	±
−365.26	84.3	−50.6	2.7	−5.5	19.4	3.9
+365.26	43.4	−59.4	0.3	32.5	−22.2	0.3
+182.62	9.3	−43.6	0.2	32.8	7.3	0.2
+121.75	0.8	−3.4	0.2	2.1	−2.5	0.2
+13.66	3.9	−1.8	0.1	−0.1	−0.3	0.0

5.2   Estimating Earth rotation resonances

The resonance parameters are estimated by weighted least squares based on the total nutation terms and their formal errors, as reported in Table 4.2, starting from a-priori values given by Mathews et al. (2002). The impact of atmospheric-oceanic circulation is investigated by considering three cases: *i*) no correction at all, *ii*) correction restricted to the annual prograde term, *iii*) correction involving all terms listed in Table 5.4.

The results are displayed in Table 5.5 for the resonance parameters (P,Q) of PMR, FCN, and FICN in the terrestrial frame. For FCN and FICN, we also provide the equivalent parameters (P',Q') in the celestial frame. It should be noted that the negative value of Q_{PMR} is associated with the dynamical response of the ocean and therefore does not represents the damping of the resonance itself, as explained in Chapter 6.

Restricting the atmospheric-oceanic correction to the prograde annual term has no significant impact on the resonance parameters. In contrast, some resonance parameters are significantly changed if we consider all terms reported in Table 5.4. Whereas PMR parameters are not modified significantly, the absolute value of the FCN period in celestial frame increases by 0.6 days and the corresponding quality factor in the terrestrial frame by 400. As well, the FICN parameters are affected: the period decreases by 50 days and the terrestrial quality factor by 90. On the other hand, the way used for estimating nutation terms is not crucial: the direct and indirect approaches lead to almost the same results according to Table 5.5.

Figure 5.3, 5.4, and 5.5 show a comparison of the resonance parameters estimates based on no atmospheric-oceanic correction, atmospheric correction only, oceanic correction only, and their combination. The removal of either atmosphere or ocean terms does not have a significant influence to the PMR parameters. For the FCN parameters, the removal of atmospheric terms lengthen the FCN period of about one day, and the quality factor is increased to 17600, whereas the annihilation of oceanic terms does not have a significant contribution. Meanwhile, the removal of atmospheric components shorten the FICN period of about 200 days and the removal of ocean decrease the quality factor of about 90.
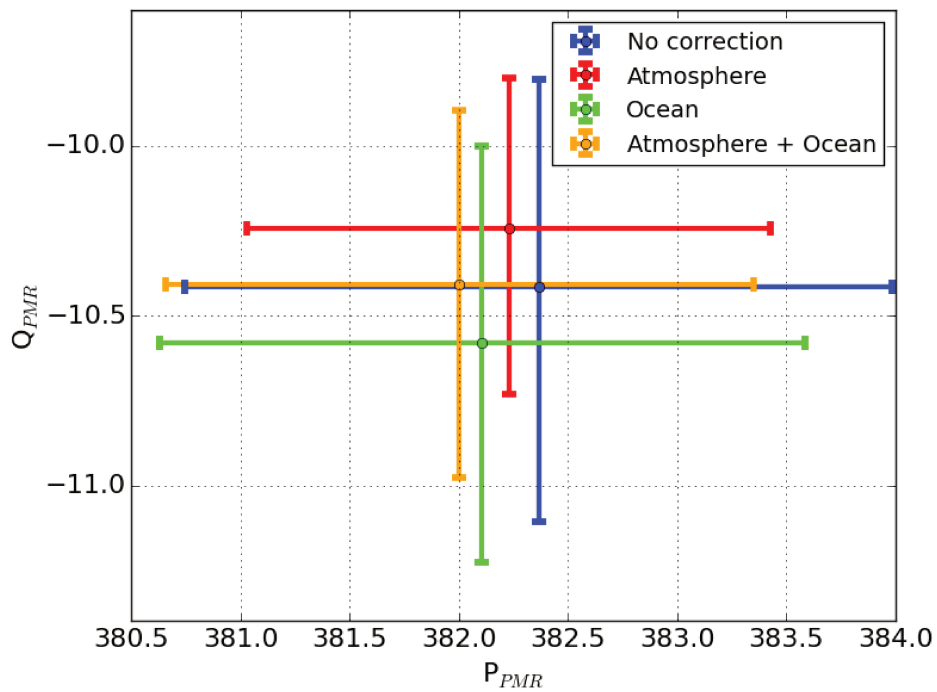
Figure 5.3 – Estimates of the PMR parameters based on no atmospheric-oceanic correction, atmospheric correction only, oceanic correction only, and their combination.
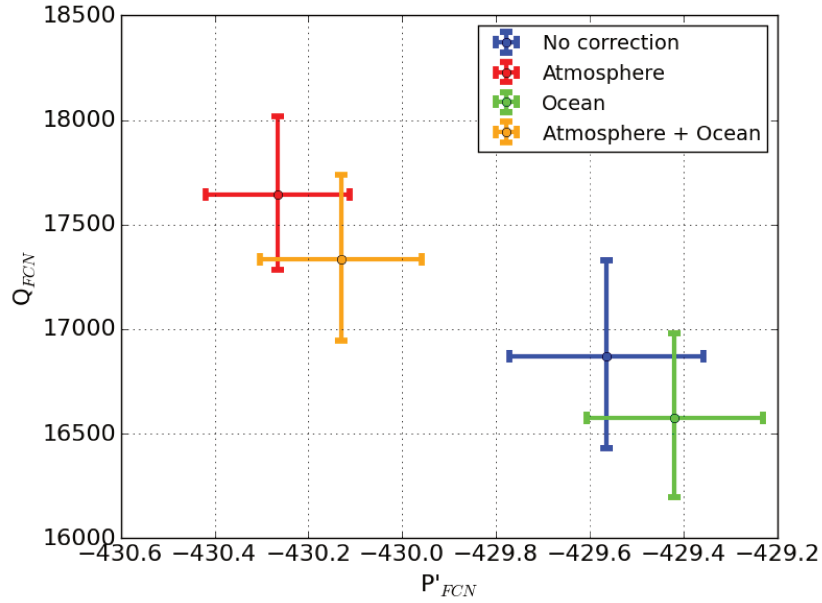
Figure 5.4 – Estimates of the FCN parameters based on no atmospheric-oceanic correction, atmospheric correction only, oceanic correction only, and their combination.
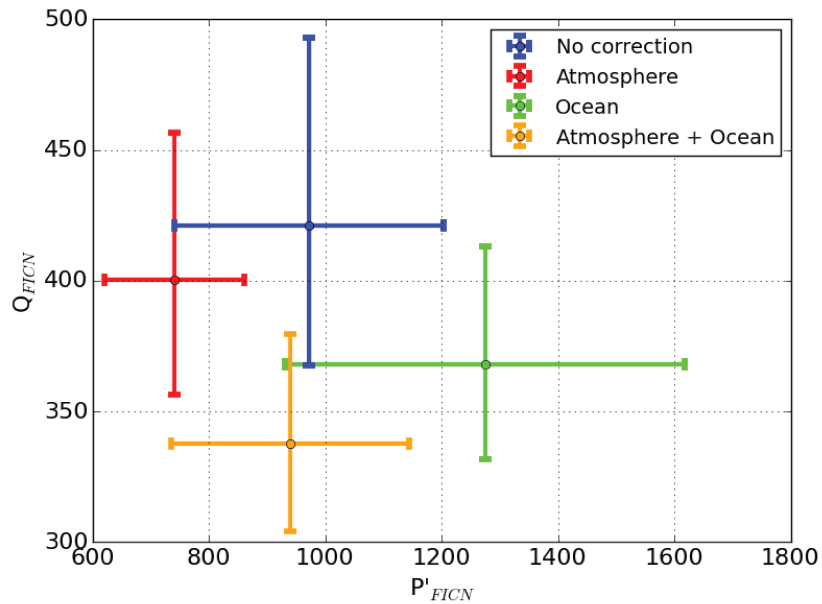

Figure 5.5 – Estimates of the FICN parameters based on no atmospheric-oceanic correction, atmospheric correction only, oceanic correction only, and their combination.

Table 5.5 – Resonance parameters associated with PMR, FCN, and FICN in the terrestrial frame (P, Q). For FICN and FCN, the period is also given in the celestial frame (P'). Periods are given in mean solar days. AO is an abbreviation for *atmospheric-oceanic*.

Procedure	AO Correction	Resonance Parameters		
		P_{PMR}	Q_{PMR}	-
Indirect	-	(380.9, **382.5**, 384.0)	(-11.0, **-10.4**, -9.8)	-
Indirect	+365.26 days only	(381.3, **382.6**, 383.9)	(-11.0, **-10.5**, -10.0)	-
Indirect	complete	(380.8, **382.1**, 383.4)	(-10.9, **-10.4**, -9.9)	-
Direct	complete	(380.7, **382.0**, 383.4)	(-11.0, **-10.4**, -9.9)	-
		P_{FCN}	Q_{FCN}	P'_{FCN}
Indirect	-	(-0.994961, **-0.994960**, -0.994959)	(16461, **16907**, 17379)	(-429.8, **-429.6**, -429.4)
Indirect	+365.26 days only	(-0.994961, **-0.994960**, -0.994959)	(16592, **16967**, 17358)	(-429.8, **-429.6**, -429.4)
Indirect	complete	(-0.994964, **-0.994963**, -0.994962)	(16958, **17361**, 17785)	(-430.3, **-430.2**, -430.0)
Direct	complete	(-0.994964, **-0.994963**, -0.994962)	(16946, **17332**, 17736)	(-430.3, **-430.1**, -430.0)
		P_{FICN}	Q_{FICN}	P'_{FICN}
Indirect	-	(-0.998492, **-0.998261**, -0.998031)	(387, **443**, 518)	(770.8, **1003.8**, 1236.9)
Indirect	+365.26 days only	(-0.998422, **-0.998240**, -0.998059)	(424, **476**, 543)	(833.9, **1025.6**, 1217.4)
Indirect	complete	(-0.998538, **-0.998312**, -0.998087)	(319, **355**, 400)	(748.4, **954.7**, 1161.0)
Direct	complete	(-0.998559, **-0.998329**, -0.998099)	(304, **338**, 380)	(735.6, **939.5**, 1143.5)

5.3 Analysis of polar motion resonance

The estimated parameters of the PMR ($P_{PMR} = 382$ d, $Q_{PMR} = -10$) confirm the fit of Mathews et al. (2002) based upon 20 years of VLBI observation, who had obtained ($P_{PMR} = 383$ d, $Q_{PMR} = -10$). These values differ from the ones corresponding to the common polar motion (see Table 2.2). According to Mathews et al. (2002), this modification results from the dynamical oceanic response in the diurnal band around the K1 sidereal frequency ($\sigma = -\Omega$).
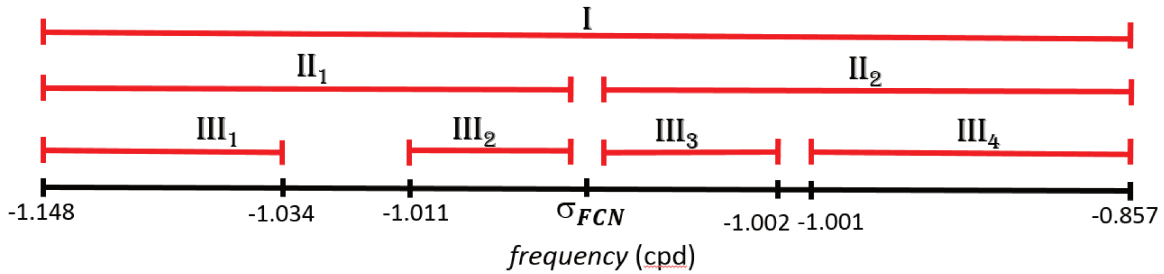

Figure 5.6 – Selected frequency band in the terrestrial frame for least-square adjustment of the PMR parameters. 18.6 year nutation term belongs to the Band III_3. Their precise limits are reported in Table 5.6.

Therefore, Mathews et al. (2002) presumed that the estimated values ($P_{PMR} = 383$ d, $Q_{PMR} = -10$) predominantly results from the 18.6 year ($\sigma = -1.00288$ cpd) nutation term, which is close to K1 frequency. To check this assumption, $\tilde{\sigma}_1$ is re-estimated (with FICN and FCN parameters fixed to the estimated values, "direct-complete" case, see Table 5.5) over restricted sets of nutation terms sweeping frequency bands as listed in Table 4.2 and illustrated in the Figure 5.6. It turns out that the estimates $\bar{P}_{PMR} = 382$, $\bar{Q}_{PMR} = -10$ over the whole set (band I) differ from the ones obtained over restricted bands, as shown by Table 5.6. In particular, for frequencies smaller than σ_{FCN} (Band II_1, III_1, III_2) we get P_{PMR} significantly larger than 415 days. Although the 18.6 year retrograde nutation prevails, the estimates of the PMR parameters are quite loose in the K1 band (band III_3) ($P_{PMR} = 382 \pm 8$, $Q_{PMR} = -10 \pm 3$) and better constrained by the prograde short period terms (band III_4) ($P_{PMR} = 382 \pm 1$, $Q_{PMR} = -10 \pm 1$).

Table 5.6 – The period and quality factor of polar motion resonance determined over certain band of frequencies.

Band	frequency (cpd)	P_{PMR}	Q_{PMR}
I	$(-\Omega - 1/6.86 \leq \sigma \leq -\Omega + 1/6.86)$	382.0 ± 1.3	-10.4 ± 0.5
II$_1$	$(-\Omega - 1/6.86 \leq \sigma \leq -\Omega - 1/386)$	418.5 ± 7.2	-8.24 ± 1.7
II$_2$	$(-\Omega - 1/1095.18 \leq \sigma \leq -\Omega + 1/6.86)$	381.8 ± 1.2	-10.4 ± 0.5
III$_1$	$(-\Omega - 1/6.86 \leq \sigma \leq -\Omega - 1/31.81)$	415.1 ± 3.3	-7.7 ± 0.7
III$_2$	$(-\Omega - 1/121.75 \leq \sigma \leq -\Omega - 1/386)$	486.8 ± 58.4	$+13.4 \pm 30.7$
III$_3$	$(-\Omega - 1/1095.18 \leq \sigma \leq -\Omega + 1/1095.18)$	381.7 ± 7.6	-10.2 ± 2.9
III$_4$	$(-\Omega + 1/386 \leq \sigma \leq -\Omega + 1/6.86)$	381.8 ± 1.3	-10.4 ± 0.5

Chapter 6

Geophysical explanation

The estimation of PMR parameters from nutation data has confirmed that the period of PMR decreases by approximately 40 days in the retrograde diurnal band in comparison with its estimation in the seasonal band, and the quality factor becomes negative. This chapter is devoted to a detailed geophysical explanation about this modification.

6.1 Contribution from the ocean

	Tidal Argument θ	χ	H_1	Φ_1	H_2	Φ_2	h_1	ϕ_1	h_2	ϕ_2
		(°)		(°)		(°)		(°)		(°)
Q1	$\gamma - l - 2F - 2\varkappa$	−90	0.116	340.4	0.264	215.4	0.058	307.8	0.075	217.1
O1	$\gamma - 2F - 2\varkappa$	−90	0.476	330.1	1.178	221.9	0.291	299.7	0.442	206.1
P1	$\gamma - 2F + 2D - 2\varkappa$	−90	0.169	310.6	0.450	223.2	0.183	287.4	0.255	192.8
K1	γ	+90	0.462	308.3	1.377	224.2	0.557	288.8	0.774	192.1
J1	$\gamma + l$	+90	0.026	294.0	0.076	228.8	0.036	292.0	0.055	186.7

Table 6.1 – The main terms of the ocean's angular momentum. These terms are generated by tesseral diurnal gravitational tides based on the FES 2012 model (Carrère et al., 2013), as reported in Madzak (2015). The reported coefficient is equivalent to (6.1). The amplitudes H_1, H_2, h_1, h_2 are in the unit of 10^{25} kg m^2/s and $\gamma = GMST + \pi$.

In the late 1980s, Dickman (1988) studied the dynamical influence of the ocean pole tide on the CW period and concluded that the dynamic effects at seasonal scales lengthen the CW period by one day, corresponding to a rise of about 0.0014 in the oceanic love number. Furthermore, the dynamic process slightly delays the ocean's reaction to the pole tide and thus introduces a tiny imaginary part in the ocean love number $\tilde{k}_o$ of about-2×10^{-4}. This imaginary part is too small to be regarded, so the assumption of a hydrostatic pole tide in the seasonal band stays true.

However, below 10 days, many studies have shown that the oceanic response to an atmospheric pressure variations strongly departs from the equilibrium, so the hydrostatic pole tide is not sound, and $\tilde{k}_o$ should change accordingly. In the diurnal band, this issue can be solved in light of the diurnal ocean tides. For, as the pole tide potential has the same form with the lunisolar tesseral potential and is relevant to the same frequency band, the Earth response should be formally the same. It is well known that the diurnal ocean tides are strongly affected by dynamical processes. Currents are generated, and in turn a relative angular momentum. Meanwhile, the observed diurnal ocean tide height is smaller than the theoretical equilibrium tide produced by the tesseral lunisolar potential, and strongly out-of-phased with respect to it. The tidal component at frequency σ causes the equatorial oceanic angular momentum

$$
\begin{aligned}
H(t) &= H_1 \cos(\theta(\sigma) + \chi - \Phi_1) + i\, H_2 \cos(\theta(\sigma) + \chi - \Phi_2)\,, \\
h(t) &= h_1 \cos(\theta(\sigma) + \chi - \phi_1) + i\, h_2 \cos(\theta(\sigma) + \chi - \phi_2)\,,
\end{aligned}
\tag{6.1}
$$

where $\theta(\sigma)$ is the tidal argument, $H(t)$ and the coefficients H_1, H_2, Φ_1, Φ_2 correspond to the matter term whereas $h(t)$ and the coefficients h_1, h_2, ϕ_1, ϕ_2 correspond to the motion term. According to the FES 2012 ocean tidal model, the main diurnal constituents are for tesseral tides J1, K1, P1, O1, and Q1. The corresponding coefficients calculated in Madzak (2015) are provided in Table 6.1. An ancient ocean tide model going back to 1996 yielded close estimates, as reported in Chao et al. (1996). The retrograde part of (6.1) is written as follows

$$
\begin{aligned}
H^-(t) &= (H^-)e^{-i(\theta+\chi)}\,, \\
h^-(t) &= (h^-)e^{-i(\theta+\chi)}\,,
\end{aligned}
\tag{6.2}
$$

where

$$H^- = \left(\frac{H_1 \cos(\Phi_1) - H_2 \sin(\Phi_2)}{2} + i \frac{H_1 \sin(\Phi_1) + H_2 \cos(\Phi_2)}{2} \right) ,$$
$$h^- = \left(\frac{h_1 \cos(\phi_1) - h_2 \sin(\phi_2)}{2} + i \frac{h_1 \sin(\phi_1) + h_2 \cos(\phi_2)}{2} \right) . \tag{6.3}$$

Here '-' corresponds to the retrograde term. From (A.4) and (A.5), the corresponding tesseral lunisolar potential is $-\Omega^2 R_e^2/3 Re \left[\tilde{\Phi}(t) \mathcal{Y}_2^{-1} \right]$, with

$$\tilde{\Phi}(t) = \frac{3g N_2^1}{\Omega^2 R_e^2} \xi_\sigma e^{-i(\theta_\sigma - \pi/2)} , \tag{6.4}$$

where g means equatorial Earth gravity, R_e is the Earth equatorial radius, ξ_σ is the equilibrium tidal height (see Table A.1), and $(N_2^1)^2 = 5/24\pi$. Accounting for the deformation effect of the tidal loading, the retrograde effective angular momentum function caused by $\tilde{\Phi}(t)$ is

$$\chi_o(t) = (1 + k_2')\chi_{ma}(t) + \chi_{mo}(t) , \tag{6.5}$$

where

$$\chi_{ma}(t) = \frac{H^-(t)}{(C-A)\Omega}; \qquad \chi_{mo}(t) = \frac{h^-(t)}{(C-A)\Omega} . \tag{6.6}$$

Since the tidal potential $\tilde{\Phi}(t)$ is formally equivalent to $m(t)$ (see A.4), so $\chi_o(t)$ is proportional to $\tilde{\Phi}(t)$, as the rotation excitation is proportional to $m(t)$:

$$\chi_o = \frac{\tilde{k}_o}{k_s} \tilde{\Phi} , \tag{6.7}$$

where $\tilde{k}_o$ is the oceanic Love number. Then, we obtain

$$\tilde{k}_o = k_s \frac{H^-(t)(1 + k_2') + h^-(t)}{(C-A)\Omega\tilde{\Phi}} = -k_s \frac{H^-(1 + k_2') + h^-}{C-A} \frac{\Omega R_e^2}{3g N_2^1 \xi_\sigma} . \tag{6.8}$$

We can estimate $\tilde{k}_o$ for the tidal components here-above by considering the ξ_σ values reported in Table A.1. The resonance of the loading love number k_2' at FCN frequency does not impact significantly $\tilde{k}_o$ in the retrograde diurnal band. For $k_2' = -0.3075$, the obtained values are given in Table 6.2 and Figure 6.2. They differ significantly from the oceanic Love number $k_o = 0.044$ estimated for an equilibrium pole tide. These results can be compared with the estimate of Mathews et al. (2002) for the K1 tide. In term of compliance, we have

Table 6.2 – Oceanic Love number $\tilde{k}_o$ of five main terms in diurnal retrograde band.

Q1	$-0.037 + i\,0.039$
O1	$-0.031 + i\,0.038$
P1	$-0.023 + i\,0.042$
K1	$-0.023 + i\,0.042$
J1	$-0.023 + i\,0.047$

$\tilde{\kappa}_o = \tilde{k}_o e / k_s = (-7.9 + i\,14.6) \times 10^{-5}$ in agreement with $(-6.9 + i\,11.5) \times 10^{-5}$, as estimated in Appendix D of Mathews et al. (2002). As shown in Figure 6.1, the values of $\tilde{k}_o$ can be fitted by a degree 2 polynomial of the frequency as follows

$$\tilde{k}_o(f) = (-0.716 + i\,0.721)f^2 + (-1.483 + i\,1.337)f + (-0.791 + i\,0.658), \qquad (6.9)$$

where f is in cpd. This expression of $\tilde{k}_o$ only holds for the diurnal domain. Then we see that the resonance frequency in (1.15) becomes frequency dependant:

$$\tilde{\sigma}_{PMR}(\sigma) = \sigma_e \frac{\bar{A}}{A_m}\left(1 - \frac{\tilde{k}_2 + \tilde{k}_o(\sigma)}{k_s}\right), \qquad (6.10)$$

here $\tilde{k}_2$ is slightly differs in diurnal band. In this band we have $\tilde{k}_2 = 0.299 - i\,0.00144$, (IERS Conventions 2010: (Petit and Luzum, 2010)). The corresponding period and quality factor is calculated by

$$P_{PMR}(\sigma) = \frac{2\pi}{\mathrm{Re}(\tilde{\sigma}_{PMR})} \quad Q_{PMR}(\sigma) = \frac{\mathrm{Re}(\tilde{\sigma}_{PMR})}{2\,\mathrm{Im}(\tilde{\sigma}_{PMR})}, \qquad (6.11)$$

Figure 6.2 displays the period and quality factor of PMR in the retrograde diurnal band. In the frequency band $[-1.2\ \mathrm{cpd}, -0.80\ \mathrm{cpd}]$, the dynamic response to the ocean leads to the interval of resonance parameters ($370\ \mathrm{d} < P_{PMR} < 383\ \mathrm{d}$; $-10 < Q_{PMR} < -4$).
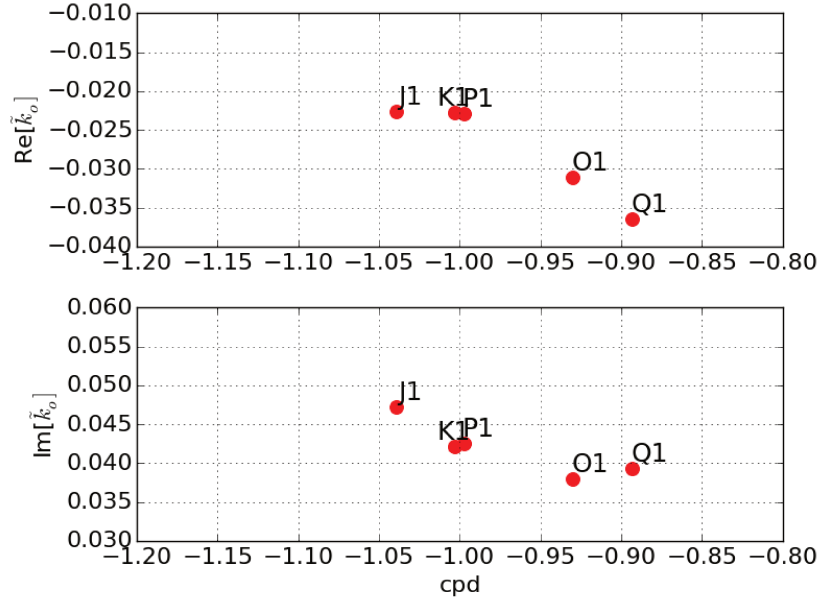
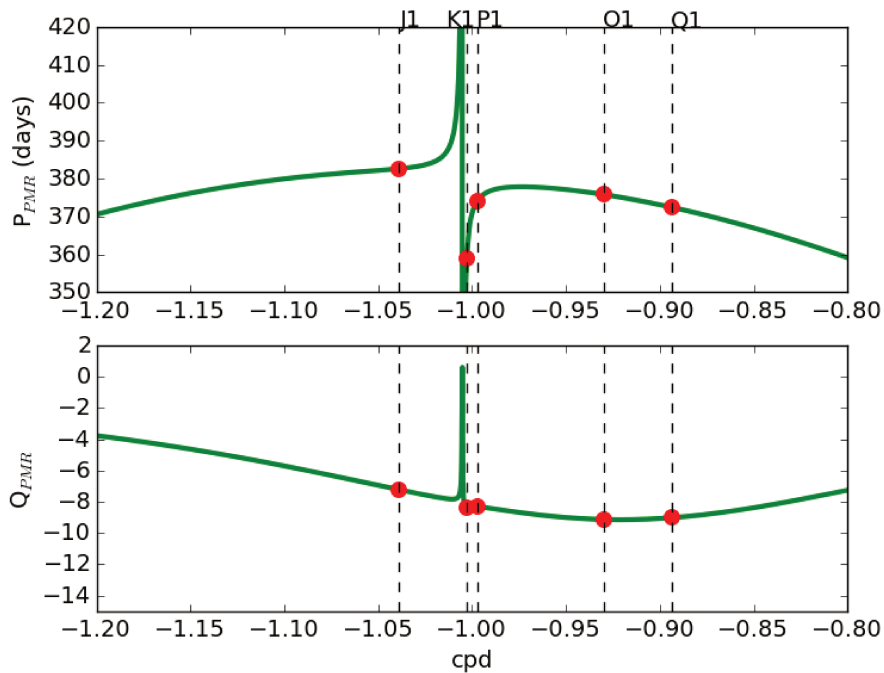Figure 6.1 – Oceanic Love number $\tilde{k}_o$ in diurnal retrograde band based on FES 2012 model.
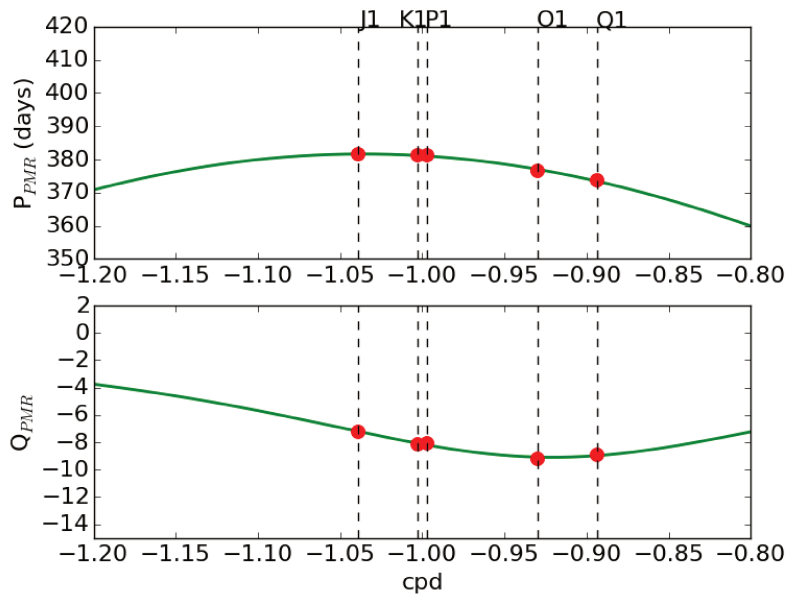
Figure 6.2 – The period and quality factor of PMR in diurnal retrograde band for anelastic Earth covered by ocean.

6.2   Contribution from Earth inner core

In the diurnal band, close to the free core nutation diurnal period, the solid Earth tide departs from the one of a quasi-elastic Earth. Indeed, the induced tilt of the core with respect to the mantle modifies the Earth mass distribution and in turn surface gravity. Predicted in the 1960's, this phenomenon had been confirmed in the 1990's through the superconducting gravimeter measurements (Crossley, 1997). Other perturbations, of much lesser amplitude (100 times less), occur because of the FICN mode at $\sigma_{FICN} \sim 1.0017$ cpd in the TRF, and because of the PMR appearing at the period of about 380 days.

Figure 6.3 – The period and quality factor of PMR in diurnal retrograde band for anelastic Earth covered by ocean and containing a fluid core.

From the IERS Conventions 2010, Table 6.4, equation 6.9 and 6.10, the perturbation of the diurnal tide on the geopotential can be described through the "diurnal" Love number as follows

$$\tilde{k}_2(\sigma) = 0.29954 - i\,0.1412\,10^{-2} - \frac{L_{PMR}}{\sigma - \sigma_{PMR}} - \frac{L_{FCN}}{\sigma - \sigma_{FCN}} - \frac{L_{FICN}}{\sigma - \sigma_{FICN}} \,, \qquad (6.12)$$

with the quantities

$$
\begin{aligned}
L_{PMR} &= (-0.77896 \times 10^{-3} - i\,0.3711 \times 10^{-4})\,k \\
L_{FCN} &= (0.90963 \times 10^{-4} - i\,0.2963 \times 10^{-5})\,k \qquad , \\
L_{FICN} &= (-0.11416 \times 10^{-5} + i\,0.5325 \times 10^{-7})\,k
\end{aligned}
\tag{6.13}
$$

and

$$
\begin{aligned}
\sigma_{PMR} &= 0.0026081 - i\,0.0001365 \\
\sigma_{FCN} &= -(1.0050624 - i\,2.5 \times 10^{-5}) \quad , \\
\sigma_{FICN} &= -(1.0017612 - i\,0.0007821)
\end{aligned}
\tag{6.14}
$$

expressed in cpd. Here $k = 1.002737811$ is the factor for converting the solar day to the sidereal day. Replacing the pure anelastic value of $\tilde{k}_2$ in (6.10) by its resonant version in (6.12), we get

$$
\tilde{\sigma}_{PMR}(\sigma) = \sigma_e \frac{A}{A_m} \frac{\tilde{k}_2(\sigma) + \tilde{k}_o(\sigma)}{k_s} \; .
\tag{6.15}
$$

Figure 6.3 displays the resonance parameter plot generated from (6.11) over the frequency $[-1.2\text{ cpd}, -0.80\text{ cpd}]$. It shows that the resonance parameters in the frequency close to K1 are heavily influenced by the FCN. Far from K1, the parameters of resonance rejoin the curve acquired from the anelastic Earth covered by ocean. In the near-FCN resonance, T_{PMR} strongly varies between -10 days to 1000 days, whereas the quality factor is below 0.5, then the resonance at $\tilde{\sigma}_{PMR}$ is heavily mitigated.

6.3 Comparison with observation

Figure 6.4 displays the comparison between the theoretical curve with the estimated values from lunisolar nutation terms, as reported in Table 5.6. It shows that, in average, the theoretical curve matches the whole band I ($P_{PMR} = 382 \pm 1$ days, $Q_{PMR} = -10 \pm 1$) except in the frequency near the FCN resonance. Meanwhile, the observation also confirms the strong perturbation of FCN resonance to the resonance parameters as well as the influence of ocean dynamics. The estimates of P_{PMR} from band III$_2$ ($P_{PMR} = 487 \pm 58$ days) confirms the enhancement of the resonance period around $\psi 1$ (theoretical value of 470 days at $\psi 1$). Furthermore, the nutation inversion in the band III$_3$ fully supports the theoretical decrease around $K1$ (modeled value

$P_{PMR} \sim 360$ days versus estimated value $P_{PMR} = 382 \pm 8$ days). Meanwhile, the nutation inversion allows getting the modeled quality factor of the band $K1$ (-10 versus -8.5). For the band ψ_1 the interval of the estimated value ($Q_{PMR} = 13 \pm 31$) is too loose for confirming the modeled value (-5), but it can include the modeled quality factor at the side frequency $\sigma_{FCN} = 1.005$ cpd ($Q_{PMR} \sim 0$).
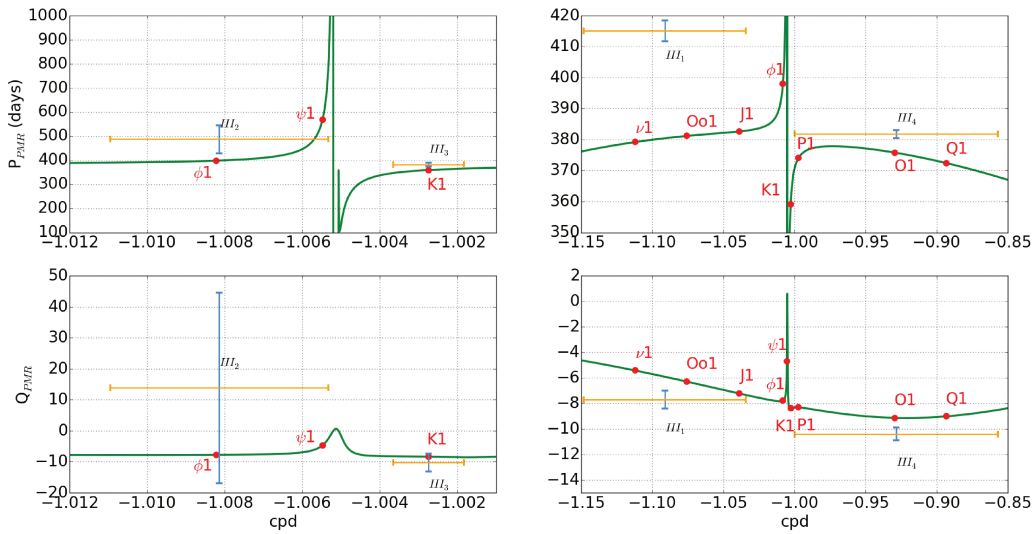

Figure 6.4 – Resonance parameters of the polar motion in the diurnal retrograde band for an anelastic Earth covered by oceans and containing a fluid core. Blue-orange crosses specify the values obtained from nutation inversion over the restricted frequency bands III_1 ($\nu 1$,Oo1), III_2 ($\phi 1$,$\psi 1$), III_3 (K1), III_4 (P1,O1,Q1): the horizontal bar extension gives the frequency band, and the vertical bar the uncertainty of the estimated value.

Outside the narrow band of the free core nutation frequency, far from $K1$ and $\psi 1$, the resonance parameters rejoin the curves obtained for an anelastic Earth covered by oceans. At the right part of the spectrum corresponding to band III_4, covering the tidal line $O1$, the estimates ($P_{PMR} = 381.8 \pm 1.3$ days, $Q_{PMR} = -10.4 \pm 0.5$) slightly differ from the modeled parameters. For the opposite band (II_1), the estimated period increased up to 415 days, as expected from the resonance. Whereas P_{PMR} varies significantly in the narrow band of the FCN, even sweeping

retrograde diurnal periods, this does produce significant resonance effect. Indeed, at σ_{FCN} the quality factor of the PMR is close to zero, associated with very strong damping.

Part III

Prograde diurnal band

Chapter 7

Polar motion resonance in prograde diurnal band

For now, we have investigated the resonance parameters in the seasonal and retrograde diurnal band. In order to obtain a more comprehensive picture, the analysis has to be extended to other frequency bands such as the multi-annual frequency range, the semi-diurnal band, and even the prograde diurnal band, where the resonance is reduced to the PMR. At multi-annual scales, our results are not conclusive, probably in reason of an incomplete knowledge of the geophysical excitation. At semi-diurnal time scale, the dominant excitation is the ocean tide potential. However, as it is no longer a tesseral wave, it cannot be used for deriving the ocean Love number describing the oceans response to the pole tide potential, which is tesseral. This leads us to only present our investigation pertaining to the diurnal prograde band, for which the dominant tidal excitation is represented by a tesseral potential, thus allowing us to model the corresponding ocean Love number. In the prograde diurnal band, like the retrograde diurnal band, the oceanic response to the pole tide is dynamic. Therefore, the PMR parameters should be different from the CW period $P_{CW} \sim 433$ days and quality factor $Q_{CW} \sim 60$ prevailing at seasonal scale.

7.1 Theoretical prediction of polar motion resonance

In the diurnal prograde band the angular momentum oscillations produced by the ocean tides is given by

$$
\begin{aligned}
H(t) &= H^+ \, e^{i\,(\theta+\chi)} \,, \\
h(t) &= h^+ \, e^{i\,(\theta+\chi)} \,,
\end{aligned}
\tag{7.1}
$$

where

$$
\begin{aligned}
H^+ &= \left(\frac{H_1 \cos(\Phi_1) + H_2 \sin(\Phi_2)}{2} + i\,\frac{-H_1 \sin(\Phi_1) + H_2 \cos(\Phi_2)}{2} \right) \,, \\
h^+ &= \left(\frac{h_1 \cos(\phi_1) + h_2 \sin(\phi_2)}{2} + i\,\frac{-h_1 \sin(\phi_1) + h_2 \cos(\phi_2)}{2} \right) \,.
\end{aligned}
\tag{7.2}
$$

The corresponding excitation function is associated with the matter and motion terms. It can be expressed in the frequency domain by

$$
\chi_{ma}(\sigma) = \frac{H^+(\sigma)}{(C-A)} \,, \qquad \chi_{mo}(\sigma) = \frac{h^+(\sigma)}{(C-A)\Omega} \,.
\tag{7.3}
$$

These lead to the effective angular function:

$$
\chi_o(\sigma) = (1 + k_2')\chi_{ma}(\sigma) + \chi_{mo}(\sigma) = \frac{H^+(\sigma)(1 + k_2') + h^+(\sigma)}{(C-A)\Omega} \,.
\tag{7.4}
$$

The $\tilde{k}_o$ number for prograde diurnal band is given by (6.8), where χ_o is replaced by the one in the prograde diurnal band:

$$
\tilde{k}_o(\sigma) = -k_s \frac{H^+(\sigma)(1 + k_2') + h^+(\sigma)}{(C-A)\Omega} \frac{\Omega R_e^2}{3gN_2^1\xi_\sigma} \,.
\tag{7.5}
$$

As shown in Table 7.1 and Figure 7.1, the oceanic love number $\tilde{k}_o$ in the prograde diurnal band is much smaller, in comparison with the retrograde diurnal one, notably for the real part, and is closer to the oceanic Love number estimated for an equilibrium pole tide. As shown in Figure 7.1, the $\tilde{k}_o$ values can be fitted by a degree two polynomial as follows

$$
\tilde{k}_o(f) = (-0.2390 + i0.5660) * f^2 + (0.4775 - i1.1334) * f + (-0.2298 + i0.5799) \,,
\tag{7.6}
$$

where f is in cpd. Then, the theoretical value of PMR in the prograde diurnal band is derived by substituting (6.15) with $\tilde{k}_o$ in (7.6). Meanwhile, the solid Earth number $\tilde{k}_2(\sigma)$ is still given in

(6.12). Figure 7.2 shows the theoretical prediction of PMR parameters. Since we are far away from FCN resonance, $\tilde{k}_2(\sigma)$ does not induce any frequency dependence. In turn, the variation of the PMR period is caused only by the ocean dynamics and is ranging from 395 to 400 in [0.8, 1.2] cpd, whereas the quality factor in the interval [-30, -10].

Table 7.1 – Oceanic Love number in the prograde diurnal band.

Q1	$0.006 + i\,0.019$
O1	$0.008 + i\,0.016$
P1	$0.008 + i\,0.012$
K1	$0.009 + i\,0.013$
J1	$0.009 + i\,0.013$
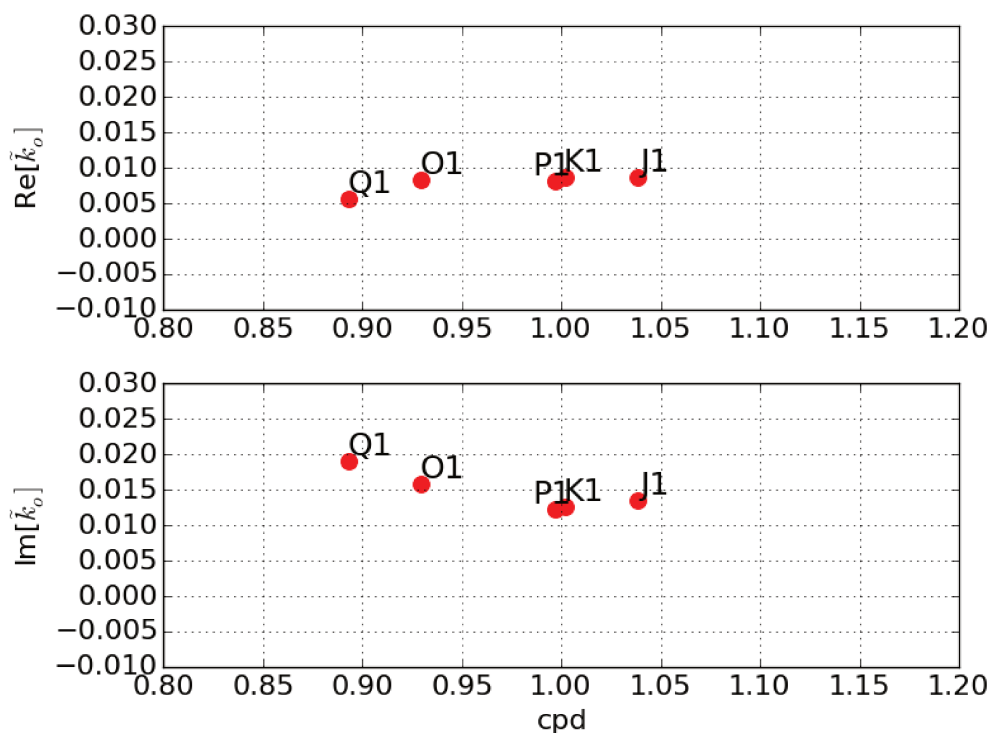
Figure 7.1 – $\tilde{k}_o$ in diurnal prograde band based on the FES 2012 ocean model.
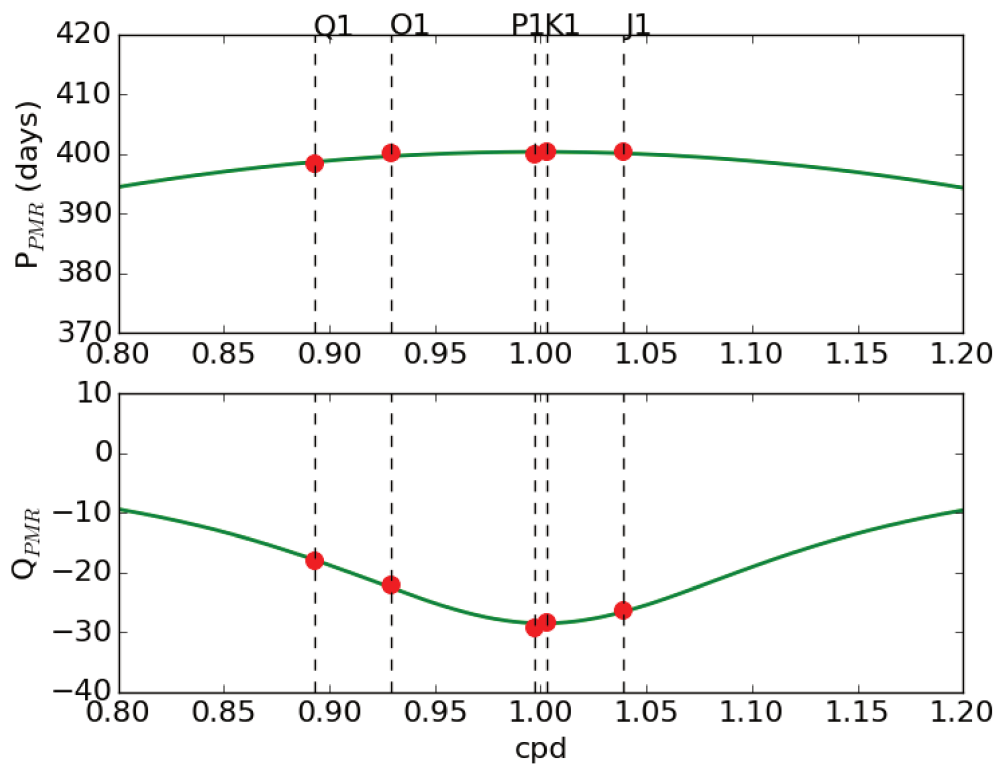
Figure 7.2 – The period and quality factor of PMR in diurnal prograde band calculated from the FES 2012 ocean model.

7.2 Estimation of prograde diurnal terms through VLBI observation

The polar motion can be represented by the sum of circular uniform motion as follows

$$p = x_p - iy_p = \sum_j \left(A_j^+ e^{i\theta_j(t)} + A_j^- e^{-i\theta_j(t)} \right) , \tag{7.7}$$

where A^+ and A^- are the complex amplitude of the prograde and retrograde terms respectively and $\theta_j(t)$ is the corresponding frequency associated with a linear combination of five Delaunay arguments (see Appendix A.3). In the prograde diurnal band, the complex amplitudes A_j^+ are decomposed into two components:

$$A_j^+ = A_{(IERS;j)}^+ + dA_j^+ , \tag{7.8}$$

where $A_{(IERS;j)}^+ = A_{(OT;j)}^+ + A_{(LIB;j)}^+$ are the complex amplitudes of the modeled variation in the pole coordinate, hereafter named IERS model, which can be separated into the ocean tidal terms $A_{(OT;j)}^+$ and the libration terms $A_{(LIB;j)}^+$. Here $dA_j^+ = dA_{(IP;j)}^+ + i\, dA_{(OP;j)}^+$ are the offsets from the model. We use the sine and cosine coefficients given in Table 8.2a and Table 5.1a in IERS conventions to calculate the a-priori $A_{(OT;j)}^+$ and $A_{(LIB;j)}^+$ respectively, whereas dA_j^+ are estimated from the VLBI observation.

Table 7.2 – Diurnal prograde terms estimated from VLBI observation over the period 1990 - 2020. Here $\gamma = GMST + \pi$ and the unit of components are μas.

	Tidal argument θ	Period (days)	A_{IP}^+	A_{OP}^+	$\pm$
Q_1	$\gamma - l - 2F - 2\varkappa$	+1.11951	30.47	−8.03	0.86
O_1	$\gamma - 2F - 2\varkappa$	+1.07580	136.70	−48.98	0.83
P_1	$\gamma - 2F + 2D - 2\varkappa$	+1.00274	49.74	−26.29	0.77
K_1	γ	+0.99726	164.36	−87.75	0.78
J_1	$\gamma + l$	+0.96243	8.70	−3.06	0.74

Actually, the complex amplitudes dA_j^+ are estimated directly from VLBI time delay according to the direct approach as for the nutation terms (see Chapter 4). The partial derivatives of the time delay with respect to dA_j^+ are

$$\frac{\partial \tau}{\partial dA_j^+} = c^{-1} \cdot \underline{k} \cdot Q(X, Y) \cdot R(-\theta) \cdot \frac{\partial W(x_p, y_p)}{\partial dA_j^+} \cdot \underline{b} \, . \tag{7.9}$$

The matrix W can be decomposed as

$$W(x_p, y_p) = W(x_{C04}, y_{C04}).W(x_{IERS}, y_{IERS}).dW(dx, dy) \, , \tag{7.10}$$

where (x_{C04}, y_{C04}) are the pole coordinates from C04 series (Bizouard et al., 2018) and (x_{IERS}, y_{IERS}) are the modeled variation of pole coordinate in the sub-diurnal band caused by ocean tides and librations, and (dx, dy) are the offsets of the pole coordinate. The matrix $dW(dx, dy)$ is given as follows

$$dW(dx, dy) = \begin{bmatrix} 0 & 0 & dx \\ 0 & 0 & dy \\ -dx & -dy & 0 \end{bmatrix} \, .$$

Here (dx, dy) are modeled as a harmonic function series:

$$dx - i\, dy = \sum_j \left(dA_j^+ e^{i\theta_j(t)} + dA_j^- e^{-i\theta_j(t)} \right) \, . \tag{7.11}$$

Therefore, the derivation of dW with respect to the IP and OP components of dA_j^+ gives

$$\frac{\partial dW}{\partial dA_{IP;j}^+} = \begin{bmatrix} 0 & 0 & \cos \theta_j(t) \\ 0 & 0 & -\sin \theta_j(t) \\ -\cos \theta_j(t) & \sin \theta_j(t) & 0 \end{bmatrix} \, ,$$

$$\frac{\partial dW}{\partial dA_{OP;j}^+} = \begin{bmatrix} 0 & 0 & -\sin \theta_j(t) \\ 0 & 0 & -\cos \theta_j(t) \\ \sin \theta_j(t) & \cos \theta_j(t) & 0 \end{bmatrix} \, .$$

We implement this partial derivative in Calc/Solve to find the corrections for 5 diurnal prograde polar motion terms: J1, K1, P1, O1, and Q1.

Table 7.3 – Diurnal prograde terms estimated from GNSS by Sibois et al. (2017).

Tide	Period (days)	A_{IP}^{+} (μas)	A_{OP}^{+} (μas)
$Q1$	1.1195148	31.7	-8.4
$O1$	1.0758059	133.8	-54.9
$P1$	1.0027454	48.3	-27.4
$K1$	0.9972696	148.3	-99.6
$J1$	0.9624365	6.7	-6.9
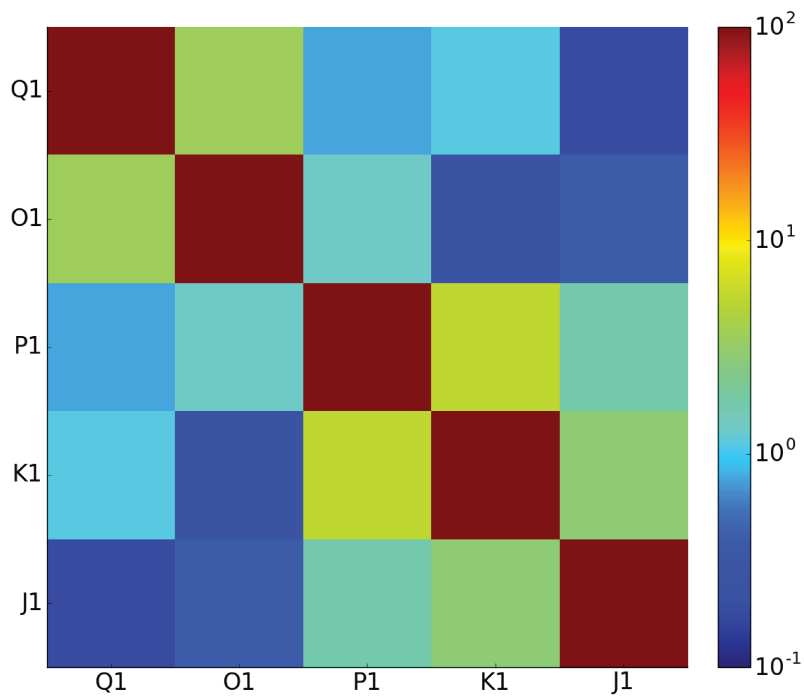
Figure 7.3 – Correlations between diurnal prograde polar motion terms from VLBI analysis. The units are in %.

The data are made up of 5452 VLBI sessions from 1990 to 2020. Unlike Chapter 4, we restrict the data range to the best VLBI session at hand (1990 - 2020), enough for splitting the considered tidal frequency. We used the same estimation strategy as in Chapter 4.

The results of our estimation are displayed in Table 7.2. This solution returned a postfit rms of 25.83 picoseconds and a χ^2 per degree of freedom equal to 1.06. The correlation between the estimated terms are given in Figure 7.3. On average, the correlations are 1.8 %, with the strongest one (5.3 %) between K_1 and P_1.

We compare our results to the ones of Sibois et al. (2017) which are based on GNSS data covering a period of 10 years with a 15 min temporal resolution. Since the results are given as sine and cosine coefficients, we have to convert them to the complex amplitude by using equation (4) of Sibois et al. (2017). These complex amplitudes are reported in Table 7.3. Figure 7.4 shows the comparison of our results with Sibois et al. (2017). They match the results from Sibois et al. (2017). Meanwhile, our results and the ones given by IERS model differ by no more than 30 μas.
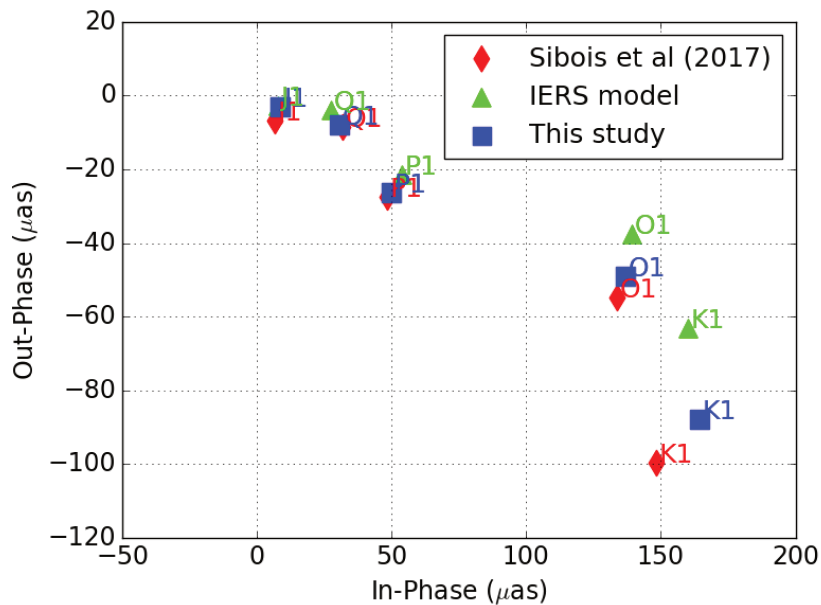
Figure 7.4 – Diurnal prograde terms according to this study, Sibois et al. (2017), and IERS model.

7.3   Polar motion resonance estimation

As the FCN and FICN do not play any role, and the ocean tide is a mass transport, we could use the relation in (1.18) to calculate the PMR parameters. It can be rewritten by considering (1.15) and (1.16) as follows

$$p(\sigma) = \frac{eA\Omega}{A_m}\left(-\frac{1}{\sigma - \tilde{\sigma}_{PMR}}\left((1 + k_2')\chi_{ma}(\sigma) + \chi_{mo}(\sigma)\right)\right). \tag{7.12}$$

In the diurnal prograde band the value of $\tilde{\sigma}_{PMR}$ is much smaller compared to σ. So, the system obtained from different tidal line in this frequency range could be ill conditioned. Hence, in order to have more robust results, we have to modify this equation. As $\chi_o(\sigma) = (1 + k_2')\chi_{ma}(\sigma) + \chi_{mo}(\sigma)$, the equation (7.12) becomes

$$p(\sigma) = \frac{eA\Omega}{A_m}\left(-\frac{\chi_o(\sigma)}{\sigma - \tilde{\sigma}_{PMR}}\right). \tag{7.13}$$

As $\chi_o = \tilde{k}_o/k_s\,\tilde{\Phi}$, we obtain

$$p(\sigma) = \frac{eA\Omega}{A_m}\left(-\frac{\tilde{k}_o}{k_s}\frac{\tilde{\Phi}(\sigma)}{\sigma - \tilde{\sigma}_{PMR}}\right). \tag{7.14}$$

By considering (6.15), the ocean love number is rewritten in term of $\tilde{\sigma}_{PMR}$ as follows

$$\tilde{k}_o = -\tilde{k}_2 + k_s\left(1 - \frac{A_m}{e\Omega A}\tilde{\sigma}_{PMR}\right). \tag{7.15}$$

Substituting $\tilde{k}_o$ in (7.14) with (7.15) leads to

$$p(\sigma) = \left[-\frac{1}{\sigma - \tilde{\sigma}_{PMR}}\left(\frac{eA\Omega}{A_m}\left(1 - \frac{\tilde{k}_2}{k_s}\right) - \tilde{\sigma}_{PMR}\right)\right]\tilde{\Phi}(\sigma). \tag{7.16}$$

The PMR parameters are estimated from (7.16) by fitting the observed prograde diurnal terms in Table 7.2 and Table 7.3 to the tidal potential $\Phi(\sigma)$. Before the inversion, the "libration" effect, corresponding to the effect of Earth triaxiality from lunisolar tide, has to be eliminated from the observed prograde diurnal terms. We adopt the libration model recommended in IERS conventions (Table 5.1a of IERS Conventions 2010).

The Table 7.4 displays the results obtained from two different set of data. It shows that the estimated period P_{PMR} is 400 ± 2 days and the quality factor Q_{PMR} is in the interval $(-26, -22)$.

Table 7.4 – Estimates PMR parameters in the prograde diurnal band.

	Period (days)	Q
This study	398.9 ± 0.4	(−24, −22)
Sibois et al. (2017)	401.9 ± 0.6	(−26, −23)

This resonance parameters match strikingly the theoretical value of Figure 7.2 (P_{PMR} = [395, 400] days; Q_{PMR} = [−30, −20]).

We test the sensitivity of the PMR parameters with respect to each prograde diurnal term by excluding one of them: thus in each estimation, we only consider four terms. The results, displayed in Table 7.5, show that the estimates are slightly sensitive to the removal of the term $K1$, which is understandable since this term is the most dominant one in the polar motion diurnal band (see Figure 7.4). By neglecting $K1$, the quality factor becomes (-21, -20).

Table 7.5 – The PMR parameters estimated from Q1, O1, P1, K1, and J1 terms by excluding one of them.

Ignored tide	Period (days)	Q
$Q1$	398.8 ± 0.5	(−24, −22)
$O1$	398.9 ± 0.3	(−25, −24)
$P1$	398.8 ± 0.5	(−24, −22)
$K1$	398.8 ± 0.3	(−21, −20)
$J1$	398.8 ± 0.5	(−24, −22)

Chapter 8

Conclusions

The main originality of my thesis is to treat three issues that are commonly investigated separately by different specialists: the processing of geodetic observations for estimating EOP, the development of Earth rotation theory, and the conjunction between observation and theory.

We have estimated the Earth resonance parameters in three frequency bands, namely the common polar motion, the retrograde diurnal, and the prograde diurnal band. The polar motion resonance (PMR) parameters in the common polar motion band were estimated by modifying the least squares fit procedure proposed by Kuehne et al. (1996) over the period 1976 - 2019. All the spectral bands from 10 days to decadal periods were taken into account except the seasonal terms. By considering all fluid layers excitations, we obtained the period 432.4 ± 1 days and the quality factor within the range $(41, 74)$. These results are in agreement with the previous studies, with a tighter quality factor. We calculated the Love number $\tilde{k}_2$ from the estimated PMR parameters and obtained the value in the range of $(0.305, 0.310)$ for the real part and $(-0.0071, -0.0027)$ for the imaginary part.

Second, we performed the adjustment of the main nutation terms and of the forced-free motion associated with the FCN by applying both direct and indirect treatment of VLBI observations. The direct approach, which was never implemented in this context, returned lower formal errors, lower correlations between the estimated nutation amplitudes, and, for some of them, amplitudes differing significantly from those of the indirect approach. The obtained nutation terms were used to determine the resonance frequencies of PMR, FCN, and FICN in the

diurnal retrograde band. For the direct approach, we obtained the period $P_{PMR} = 382.5 \pm 1.5$ and the quality factor Q_{PMR} in the interval $(-11, -10)$. Moreover, the estimates of the FCN period and quality factor are $P_{FCN} = -429.6 \pm 0.2$ and Q_{FCN} in the interval $(16461, 17379)$ and the estimates of the FICN parameters are $P_{FICN} = 1003 \pm 233$ and Q_{FICN} in the interval $(387, 518)$. No significant discrepancies have been noticed between the resonance parameters based upon the 'direct' and 'indirect' nutation terms. The inclusion of the complete atmospheric and non-tidal ocean corrections has increased the FCN period in the celestial frame by 0.6 day and the corresponding quality factor in the terrestrial frame by 400. Meanwhile, the FICN parameters have decreased the period by 50 days and the quality factor by 90.

We have shown that the shorter period of the PMR in the nutation band is mainly caused by the dynamical response of the oceans to the pole tide potential, and the associated negative quality factor reflects the strong phase-shift of this response with respect to the pole tide. The comparison of observed nutation terms to those of a rigid Earth, fit amazingly well to the modeled frequency dependence of PMR parameters derived from the ocean tidal model, and the knowledge of the effect of the free core nutation resonance on $\tilde{k}_2$. So, the lunisolar nutation determined by VLBI reflects the dynamical behavior of the oceans and the influence of the fluid core on solid Earth deformations in the retrograde diurnal band. A similar analysis is carried out for the prograde diurnal band and it shows that the estimated PMR has a period $P_{PMR} = 400 \pm 2$ days and a quality factor Q_{PMR} in the interval $(-26, -22)$. These results match the results derived from the ocean tidal model.

Our study has shown that the determination of the frequency of the Earth's rotational modes is a powerful way for determining the rheological properties of the solid Earth and the ocean response to an external forcing in a wide range of frequency, from one day to several years. So, our work has to be continued by analyzing the resonances in the frequency bands that have not been explored yet. The investigation in the semi diurnal band can be done by considering the excitation from ocean tides. Moreover, it would be crucial to estimate the PMR parameters at the decadal time scale, where the nature of the Earth inelasticity has an important impact on the solid Earth love number $\tilde{k}_2$. Finally, since this study is restricted to the equatorial changes of Earth rotation, it has to be extended to its axial ones. As length of day depends on the Earth deformation (i.e. $\tilde{k}_2$), we foresee the possibility to investigate the frequency dependence

of $\tilde{k}_2$ by treating the length of day and polar motion in a combined approach, as well as their corresponding excitation.

Appendix

A.1 Space geodetic technique

Several domains, such as the navigation of the satellites, need regular data for the Earth rotation, in particular the terrestrial and celestial oscillation of the CIP. In order to fulfill this requirement, several geodetical techniques monitor the Earth rotation at almost regular intervals. Very Long Baseline Interferometry (VLBI) is the only technique that can observe the nutation, whereas the polar motion is mostly monitored by Global Navigation Satellite System (GNSS), and in a less exact by Satellite Laser Ranging (SLR) and VLBI.

VLBI. This technique consist of a network of radio telescopes that fulfill certain criteria and make use of the technique called interferometry observing several objects in the sky. The development of VLBI for astronomical purposes begins in late 1960 (Broten et al., 1967; Bare et al., 1967). VLBI contributed to the observation of the reference frame and the EOP starting in 1979. It contributes to the International Terrestrial Reference Frame by enabling the estimation of its station positions. It is also the only technique that can be used to observe quasars in order to determine the International Celestial Reference Frame. Furthermore, VLBI is the only technique that can determine all of EOP at a regular basis. A VLBI network consists of several radio telescopes distributed all over the world. The principle of VLBI is based on the difference of the arrival time of the signal at the various stations. This information is extracted by using a so-called correlators. Figure A.1 shows the distribution of VLBI station. We clearly see that the station network covers the entire globe, even it is still dominated in the northern hemisphere.

GNSS. The four main systems of GNSS are the American GPS, the Russian GLONASS, the European GALILEO, and the Chinese Beidou. These satellite systems provide an autonomous
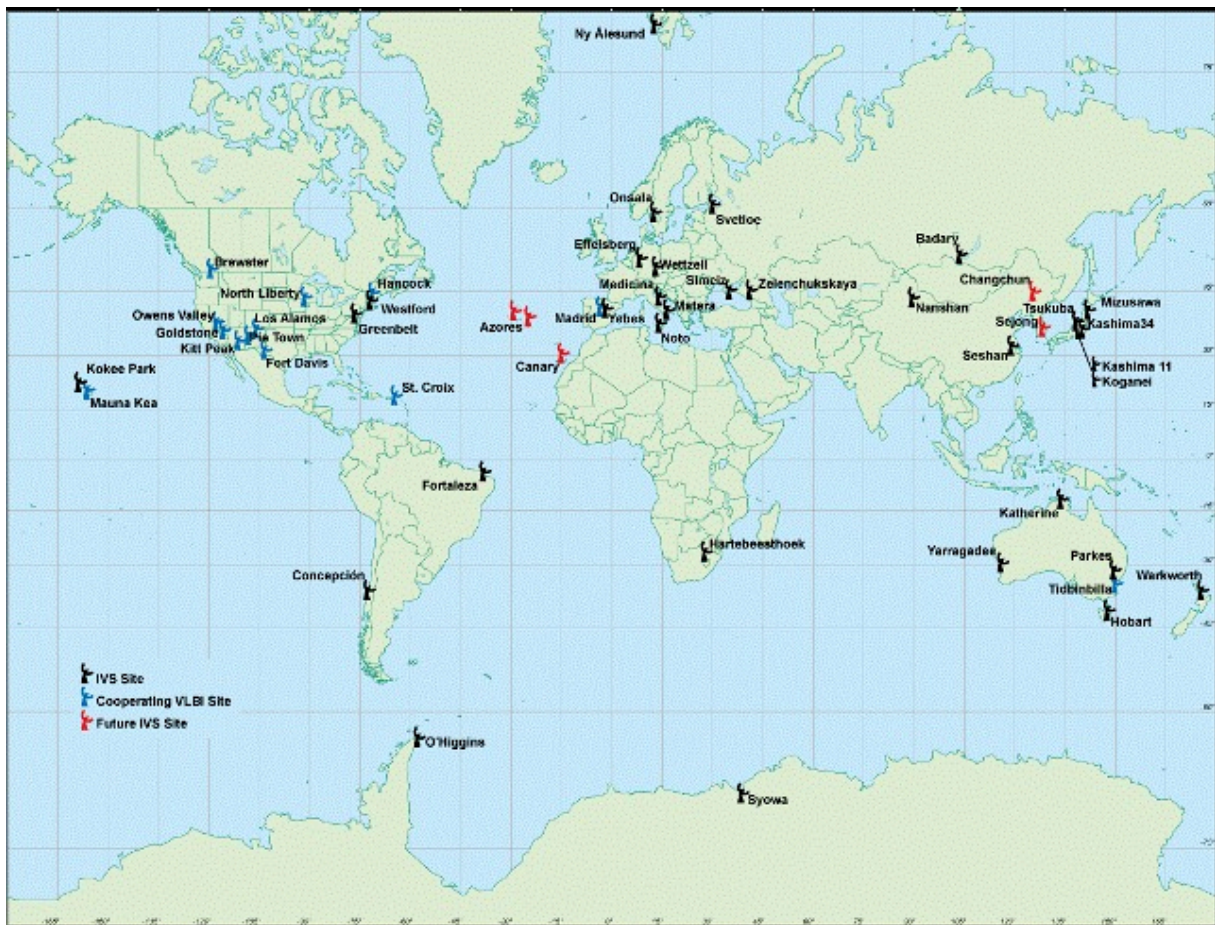
Figure A.1 – The distribution of VLBI station around the world.

geo-spatial positioning with global coverage. GNSS system can be used to study the Earth rotation, notably the polar motion and LOD, since the transfer of the satellite signals to the Earth's surface is influenced by the relative motion between the satellite and the receiver caused by the Earth rotation. It has the highest accuracy to determine the polar motion, notably the rapid polar motion.

SLR. SLR stations on the Earth's surface emit ultra-short laser pulses to the satellites equipped with retroreflectors. The laser pulses is reflected to the SLR station, and thus the time of laser propagation can be calculated. Since the position of the SLR station depends on the Earth rotation, the laser travel time is used to monitor the polar motion and the LOD. Nowadays, there is more than 50 SLR station around the world.

A.2   Celestial Intermediate Pole
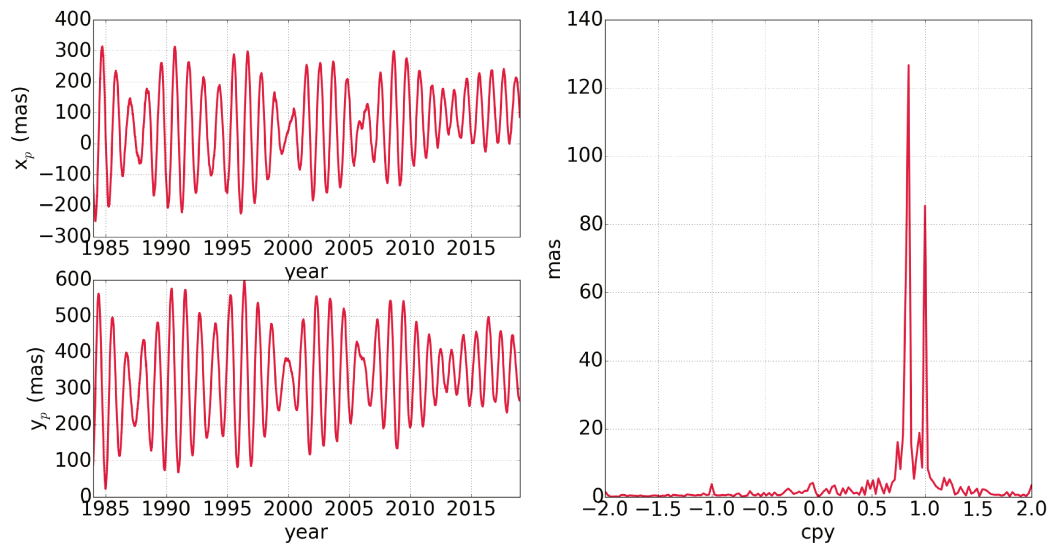
Figure A.2 – Observed polar motion: on the left side corresponds to the daily polar motion series and their corresponding spectral plot is on the right side.

The space geodetic observations allow to determine the CIP, which differs from the instantaneous rotational axis up to 20 mas. The polar coordinates (x, y) are the CIP position relative to
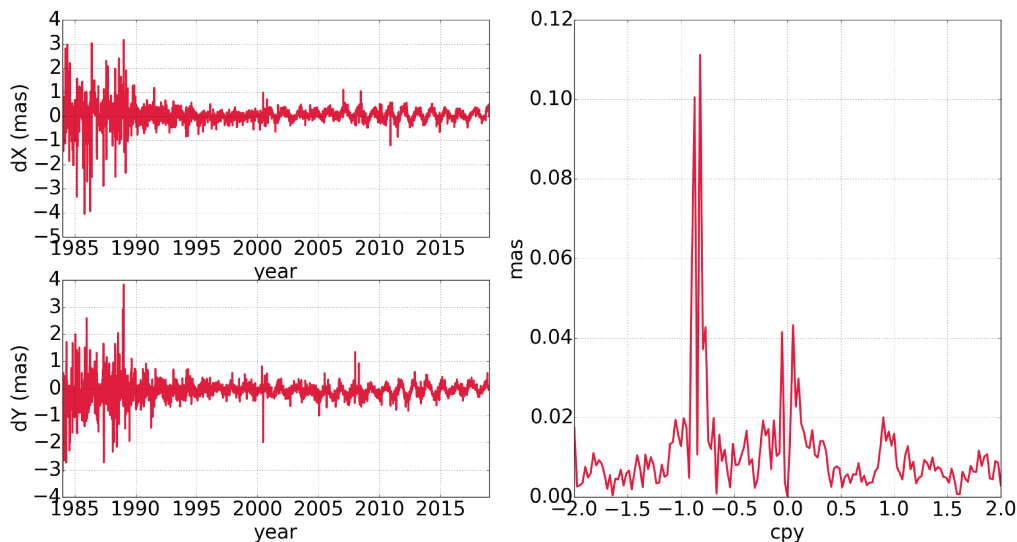
Figure A.3 – Observed nutation offset with respect to the IAU 2000/2006 model: on the left side corresponds to the daily nutation series and their corresponding spectral plot is on the right side.

the terrestrial reference frame, whereas celestial pole coordinates give (*X*, *Y*) as the CIP position with respect to the celestial reference frame.

Actually, the precession-nutation model yields the principal part of (*X*, *Y*) coordinates, to which one brings the corrections called nutation or celestial pole offsets (*dX,dY*) with values not exceeding one mas with respect the IAU 2000/2006 model (Petit and Luzum, 2010). Figure A.2 and Figure A.3 display the polar motion and nutation offsets in time and frequency domains. The highest peak in the polar motion spectrum comes from PMR, whereas FCN becomes the most dominant peak in the nutation offset spectrum.

The CIP fully separates the variation of the Earth rotation axis in the celestial frame (nutation) from its variation in the terrestrial frame (polar motion). Figure A.4 displays the frequency division of the CIP in the terrestrial and celestial reference frame. The nutation is equivalent to a retrograde diurnal polar motion, whereas the polar motion is equivalent to a sub-diurnal nutation.
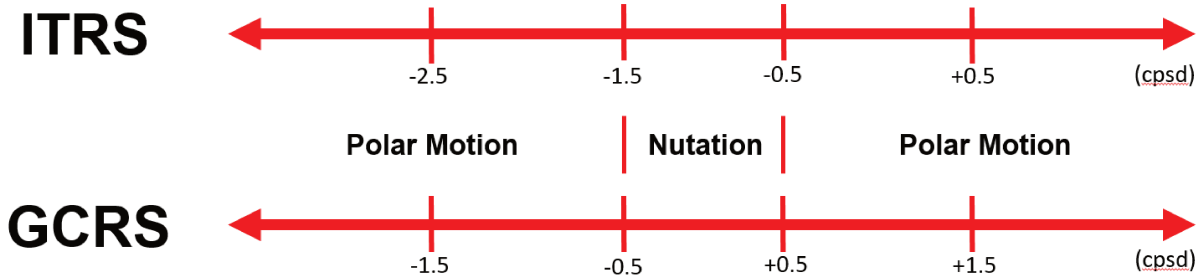
Figure A.4 – Frequency division of nutation and polar motion in the terrestrial and celestial frequency band. The frequency unit is cycle per siderial days (cpsd). This image is based on IERS Convention 2010.

A.3   Delaunay arguments

At a tidal frequency, the tidal phase can be obtained by the combination of Delaunay arguments $l, l', D, F, \varkappa$, and γ: $\theta = a_1 l + a_2 l' + a_3 D + a_4 F + a_5 \varkappa + a_6 \gamma$, where $\gamma = \text{GMST} + \pi$ and $a_6 = 1$ for diurnal terms, $a_6 = 2$ for semi-diurnal terms, and $a_6 = 0$ for seasonal terms. According to the IERS Convention 2010, the Delaunay arguments are represented as follows

Mean anomaly of the Moon:

$$l = 134.96340251° + 1717915923.2178''t + 31.8792''t^2 + 0.051635''t^3 - 0.00024470''t^4,$$

Mean anomaly of the Sun:

$$l' = 357.52910918° + 129596581.04810''t - 0.5532''t^2 + 0.000136''t^3 - 0.00001149''t^4,$$

Mean elongation of the Moon from the Sun:

$$D = 297.85019547° + 1602961601.2090''t - 6.3706''t^2 + 0.006593''t^3 - 0.00003169''t^4,$$

Mean longitude of the ascending node of the Moon:

$$\varkappa = 125.04455501° - 6962890.5431''t + 7.4722''t^2 + 0.007702''t^3 - 0.00005939''t^4,$$

The mean distance of the Moon from the ascending node:

$$F = 93.27209062° + 1739527262.8478''t - 12.7512''t^2 - 0.001037''t^3 + 0.00000417''t^4.$$

Here t is measured in Julian centuries.

A.4   Tesseral tidal potential

The material of this appendix is inspired from Dehant and Mathews (2015), Section 5.5. Consider a point of the Earth at distance r from the geocenter of latitude ϕ and longitude λ. At this place the tesseral part of the tidal potential generated by a celestial body of mass M — located in the true equatorial frame by its right ascension α, declination δ, and distance d from the geocenter — is given by

$$W = \frac{GM}{d^5}\frac{1}{3}d^2 P_2^1(\sin\delta)r^2 P_2^1(\sin\phi)\cos(\lambda - \alpha) \ . \tag{A.1}$$

Here the polar motion effect on the tidal potential is neglected: astronomical and geographic latitudes are merged, as well the node of prime meridian with the Terrestrial International Origin (Petit and Luzum, 2010). Introducing the terrestrial Cartesian coordinates (x, y, z) and (d_x, d_y, d_z) of the location and of the celestial body respectively, we can easily derive

$$W = \frac{3GM}{d^5}zd_z \operatorname{Re}\left[(d_x + id_y)(x - iy)\right] \ . \tag{A.2}$$

Then, noting that $r^2 \mathcal{Y}_2^{-1} = 3(xz - iyz)$, where $\mathcal{Y}_2^{-1} = 3\sin\theta\cos\theta e^{-i\lambda}$ is the complex conjugate of the non-normalized spherical harmonic function of degree 2 and order 1, we obtain

$$W = \frac{GM}{d^5}d_z r^2 \operatorname{Re}\left[(d_x + id_y)\mathcal{Y}_2^{-1}\right] \ . \tag{A.3}$$

It is useful to put the W into the form of the pole tide potential $\Delta U^{(r)} = -\frac{\Omega^2 r^2}{3}\operatorname{Re}\left[m(t)\mathcal{Y}_2^{-1}\right]$:

$$W = -\frac{\Omega^2 r^2}{3}\operatorname{Re}\left[\tilde{\Phi}(t)\mathcal{Y}_2^{-1}\right] \ , \quad \text{with} \quad \tilde{\Phi}(t) = -\frac{3GM}{\Omega^2 d^5}d_z(d_x + id_y) \ . \tag{A.4}$$

Then, $\tilde{\Phi}(t)$ presents the Cartwright-Taylor like expansion

$$\tilde{\Phi}(t) = \frac{3gN_2^1}{\Omega^2 R_e^2}\sum_{\sigma \geq 0}\xi_\sigma e^{-i(\theta_\sigma(t) - \pi/2)} \ , \tag{A.5}$$

where θ_σ is the tidal argument in the corresponding frequency σ. In Table A.1, we report the coefficients of the tesseral luni-solar tides that are considered in this thesis. For a given tidal component, the numerical application yields

$$\tilde{\Phi}_\sigma(t) = 3.51\ 10^{-5}\ [\text{m}^{-1}]\,\xi_\sigma[\text{m}]e^{-i(\theta_\sigma(t) - \pi/2)} \ . \tag{A.6}$$

	Tidal argument θ_σ	σ (cpd)	ξ_σ (m)
Q_1	$\gamma - l - 2F - 2\varkappa$	0.8932	-0.05021
O_1	$\gamma - 2F - 2\varkappa$	0.9295	-0.26223
P_1	$\gamma - 2F + 2D - 2\varkappa$	0.9973	-0.12199
K_1	γ	1.0027	0.36864
J_1	$\gamma + l$	1.0390	0.02062

Table A.1 – Coefficients of the luni-solar tides used in this thesis, as reported in Dehant and Mathews (2015)

List of Figures

95

List of Tables

Acronyms

μas   microarcsecond.

CIP   Celestial Intermediate Pole.

CMB   Core-Mantle Boundary.

cpd   cycle per day.

CPO   Celestial Pole Offset.

CW   Chandler Wobble.

EAAM   Effective Atmospheric Angular Momentum Function.

ECCO   Estimating the Circulation and Climate of the Ocean.

ECMWF   European Centre for Medium-Range Weather Forecasts.

EHAM   Effective Hydrological Angular Momentum Function.

EOAM   Effective Oceanic Angular Momentum Function.

EOP   Earth Orientation Parameters.

FCN   Free Core Nutation.

FFT   Fast Fourier Transform.

FICN   Free Inner Core Nutation.

FWHM   Full Width at Half Maximum.

GFZ   GeoForschungsZentrum.

GNSS   Global Navigation Satellite System.

IB	Inverted Barometer.
ICB	Inner-Core Boundary.
ICW	Inner Core Wobble.
IERS	International Earth Rotation Service.
IP	In-Phase.
LSDM	Land Surface Discharge Model.
mas	Milliarcsecond.
MPIOM	Max Planck Institute Ocean Model.
NCEP	National Center for Environmental Prediction.
NIB	Non-Inverted Barometer.
OP	Out-of-Phase.
PMR	Polar Motion Resonance.
RMS	Root Mean Square.
SLR	Satellite Laser Ranging.
VLBI	Very Long Baseline Interferometry.

Bibliography

Altamimi, Z., Rebischung, P., Métivier, L., and Collilieux, X. (2016). Itrf2014: A new release of the international terrestrial reference frame modeling nonlinear station motions. Journal of Geophysical Research: Solid Earth, 121(8):6109–6131.

Bare, C., Clark, B. G., Kellermann, K. I., Cohen, M. H., and Jauncey, D. L. (1967). Interferometer experiment with independent local oscillators. Science, 157(3785):189–191.

Belda, S., Ferrándiz, J. M., Heinkelmann, R., Nilsson, T., and Schuh, H. (2016). Testing a new free core nutation empirical model. Journal of Geodynamics, 94:59–67.

Bizouard, C. (2014). Le mouvement du pole de lheure au siecle : Modelisation geophysique. Presses Academiques Francophones.

Bizouard, C., Brzeziński, A., and Petrov, S. (1998). Diurnal atmospheric forcing and temporal variations of the nutation amplitudes. Journal of Geodesy, 72(10):561–577.

Bizouard, C., Lambert, S., Gattano, C., Becker, O., and Richard, J.-Y. (2018). The IERS EOP 14C04 solution for Earth orientation parameters consistent with ITRF 2014. Journal of Geodesy.

Böhm, J., Werl, B., and Schuh, H. (2006). Troposphere mapping functions for gps and very long baseline interferometry from european centre for medium-range weather forecasts operational analysis data. Journal of Geophysical Research: Solid Earth, 111(B2).

Broten, N., Legg, T., Locke, J., McLeish, C., Richards, R., Chisholm, R., Gush, H., Yen, J., and

Galt, J. (1967). Long base line interferometry: a new technique. Science, 156(3782):1592–1593.

Brzeziński, A. (1994). Polar motion excitation by variations of the effective angular momentum function, ii: extended model. Manuscr Geod, 19:157–171.

Brzeziński, A. and Capitaine, N. (1993). The use of the precise observations of the celestial ephemeris pole in the analysis of geophysical excitation of earth rotation. Journal of Geophysical Research: Solid Earth, 98(B4):6667–6675.

Brzeziński, A., Dobslaw, H., Dill, R., and Thomas, M. (2012). Geophysical excitation of the chandler wobble revisited. In Geodesy for Planet Earth, pages 499–505. Springer.

Capitaine, N., Wallace, P. T., and Chapront, J. (2003). Expressions for IAU 2000 precession quantities. Astronomy & Astrophysics, 412(2):567–586.

Carrère, L., Lyard, F., Cancet, M., Guillot, A., and Roblou, L. (2013). Fes 2012: a new global tidal model taking advantage of nearly 20 years of altimetry. In 20 Years of Progress in Radar Altimatry, volume 710.

Chao, B. F. and Hsieh, Y. (2015). The Earth's free core nutation: Formulation of dynamics and estimation of eigenperiod from the very-long-baseline interferometry data. Earth and Planetary Science Letters, 432:483–492.

Chao, B. F., Ray, R. D., Gipson, J. M., Egbert, G. D., and Ma, C. (1996). Diurnal/semidiurnal polar motion excited by oceanic tidal angular momentum. Journal of Geophysical Research: Solid Earth, 101(B9):20151–20163.

Chen, W. and Shen, W. (2010). New estimates of the inertia tensor and rotation of the triaxial nonrigid earth. Journal of Geophysical Research: Solid Earth, 115.

Crossley, D. (1997). Earth's Deep Interior. Gordon and Breach Sci. Publ.

Dehant, V., de Viron, O., and Greff-Lefftz, M. (2005). Atmospheric and oceanic excitation of the rotation of a three-layer Earth. Astronomy & Astrophysics, 438:1149–1161.

Dehant, V., Feissel-Vernier, M., de Viron, O., Ma, C., Yseboodt, M., and Bizouard, C. (2003). Remaining error sources in the nutation at the submilliarc second level. Journal of Geophysical Research: Solid Earth, 108(B5).

Dehant, V., Laguerre, R., Rekier, J., Rivoldini, A., Triana, S. A., Trinh, A., Van Hoolst, T., and Zhu, P. (2017). Understanding the effects of the core on the nutation of the earth. Geodesy and Geodynamics, 8(6):389–395.

Dehant, V. and Mathews, P. M. (2015). Precession, nutation and wobble of the Earth. Cambridge University Press.

Desai, S. D. (2002). Observing the pole tide with satellite altimetry. Journal of Geophysical Research: Oceans, 107(C11):7–1.

Dickman, S. (1988). The self-consistent dynamic pole tide in non-global oceans. Geophysical Journal International, 94(3):519–543.

Dobslaw, H., Dill, R., Grötzsch, A., Brzeziński, A., and Thomas, M. (2010). Seasonal polar motion excitation from numerical models of atmosphere, ocean, and continental hydrosphere. Journal of Geophysical Research: Solid Earth, 115(B10).

Dobslaw, H. and Thomas, M. (2007). Simulation and observation of global ocean mass anomalies. Journal of Geophysical Research: Oceans, 112(C5).

Eubanks, T. (1993). Variations in the orientation of the Earth. Contributions of Space Geodesy to Geodynamics: Earth Dynamics, pages 1–54.

Fey, A. L., Gordon, D., Jacobs, C. S., Ma, C., Gaume, R., Arias, E., Bianco, G., Boboltz, D., Böckmann, S., Bolotin, S., et al. (2015). The second realization of the international celestial reference frame by very long baseline interferometry. The Astronomical Journal, 150(2):58.

Furuya, M. and Chao, B. F. (1996). Estimation of period and q of the chandler wobble. Geophysical Journal, 127(3):693–702.

Gross, R. (2005). The observed period and q of the chandler wobble. In Forcing of Polar Motion in the Chandler Frequency Band: A Contribution to Understanding Interannual Climate Change, volume 24, pages 31–37.

Gross, R., Fukumori, I., and Menemenlis, D. (2005). Atmospheric and oceanic excitation of decadal-scale earth orientation variations. Journal of Geophysical Research: Solid Earth, 110(B9):CiteID B09405.

Herring, T. A., Mathews, P. M., and Buffett, B. A. (2002). Modeling of nutation-precession: Very long baseline interferometry results. Journal of Geophysical Research: Solid Earth, 107(B4):ETG 4–1–ETG 4–12.

Himwich, W. and Harder, E. (1988). Direct estimation of nutation coefficients from vlbi data. In Symposium-International Astronomical Union, volume 128, pages 301–307. Cambridge University Press.

Jeffreys, H. (1968). The variation of latitude. Monthly Notices of the Royal Astronomical Society, 141(2):255–270.

Kalnay, E., Kanamitsu, M., Kistler, R., Collins, W., Deaven, D., Gandin, L., Iredell, M., Saha, S., White, G., Woollen, J., et al. (1996). The NCEP/NCAR 40-year Reanalysis Project. Bulletin of the American meteorological Society, 77(3):437–471.

Koot, L., Rivoldini, A., De Viron, O., and Dehant, V. (2008). Estimation of earth interior parameters from a bayesian inversion of very long baseline interferometry nutation time series. Journal of Geophysical Research: Solid Earth, 113(B8).

Krásná, H., Böhm, J., and Schuh, H. (2013). Free core nutation observed by vlbi. Astronomy & Astrophysics, 555:A29.

Kuehne, J., Wilson, C. R., and Johnson, S. (1996). Estimates of the chandler wobble frequency and q. Journal of Geophysical Research, 101:13573–13580.

Lyard, F., Lefevre, F., Letellier, T., and Francis, O. (2006). Modelling the global ocean tides: modern insights from fes2004. Ocean Dynamics, 56(5-6):394–415.

Ma, C., Clark, T., Ryan, J., Herring, T., Shapiro, I., Corey, B., Hinteregger, H., Rogers, A., Whitney, A., Knight, C., et al. (1986). Radio-source positions from vlbi. The Astronomical Journal, 92:1020–1029.

Madzak, M. (2015). Short period ocean tidal variations in Earth rotation. PhD thesis, Vienna University of Technology.

Malkin, Z. (2007). Empiric models of the earth's free core nutation. Solar System Research, 41(6):492–497.

Mathews, P., Buffett, B., Herring, T., and Shapiro, I. (1991a). Forced nutations of the earth: Influence of inner core dynamics: 2. numerical results and comparisons. Journal of Geophysical Research: Solid Earth, 96(B5):8243–8257.

Mathews, P., Buffett, B. A., Herring, T. A., and Shapiro, I. I. (1991b). Forced nutations of the earth: Influence of inner core dynamics: 1. theory. Journal of Geophysical Research: Solid Earth, 96(B5):8219–8242.

Mathews, P. M., Herring, T. A., and Buffett, B. A. (2002). Modeling of nutation and precession: New nutation series for nonrigid earth and insights into the earth's interior. Journal of Geophysical Research: Solid Earth, 107(B4):ETG–3.

Mignard, F. and Klioner, S. (2012). Analysis of astrometric catalogues with vector spherical harmonics. Astronomy & Astrophysics, 547:A59.

Nastula, J. and Gross, R. (2015). Chandler wobble parameters from slr and grace. Journal of Geophysical Research: Solid Earth, 120:4474–4483.

Nothnagel, A. (2009). Conventions on thermal expansion modelling of radio telescopes for geodetic and astrometric vlbi. Journal of Geodesy, 83(8):787–792.

Ooe, M. (1978). An optimal complex ar. ma model of the chandler wobble. Geophysical Journal International, 53(3):445–457.

Petit, G. and Luzum, B. (2010). IERS Conventions 2010. IERS Technical Note 36, Frankfurt am Main: Verlag des Bundesamts für Kartographie und Geodäsie, 2010. 179 pp., ISBN 3-89888-989-6.

Petrov, L. (2007). The empirical earth rotation model from vlbi observations. Astronomy & Astrophysics, 467(1):359–369.

Petrov, L. and Boy, J.-P. (2004). Study of the atmospheric pressure loading signal in very long baseline interferometry observations. Journal of Geophysical Research: Solid Earth, 109(B3).

Roosbeek, F. and Dehant, V. (1998). Rdan97: An analytical development of rigid earth nutation series using the torque approach. Celestial Mechanics and Dynamical Astronomy, 70(4):215–253.

Rosat, S., Lambert, S., Gattano, C., and Calvo, M. (2016). Earth's core and inner-core resonances from analysis of vlbi nutation and superconducting gravimeter data. Geophysical Supplements to the Monthly Notices of the Royal Astronomical Society, 208(1):211–220.

Rosat, S. and Lambert, S. B. (2009). Free core nutation resonance parameters from vlbi and superconducting gravimeter data. Astronomy & Astrophysics, 503(1):287–291.

Schindelegger, M., Böhm, J., Salstein, D., and Schuh, H. (2011). High-resolution atmospheric angular momentum functions related to earth rotation parameters during cont08. Journal of Geodesy, 85(7):425.

Seitz, F., Kirschner, S., and Neubersch, D. (2012). Determination of the earth's pole tide love number k2 from observations of polar motion using an adaptive kalman filter approach. Journal of Geophysical Research: Solid Earth, 117(B9).

Sibois, A. E., Desai, S. D., Bertiger, W., and Haines, B. J. (2017). Analysis of decade-long time series of gps-based polar motion estimates at 15-min temporal resolution. Journal of Geodesy, 91(8):965–983.

Souchay, J., Loysel, B., Kinoshita, H., and Folgueira, M. (1999). Corrections and new developments in rigid earth nutation theory-iii. final tables" ren-2000" including crossed-nutation and spin-orbit coupling effects. Astronomy and Astrophysics Supplement Series, 135(1):111–131.

Vondrák, J., Weber, R., and Ron, C. (2005). Free core nutation: direct observations and resonance effects. Astronomy & Astrophysics, 444(1):297–303.

Wilson, C. R. (1985). Discrete polar motion equations. Geophysical Journal, 80(2):551 – 554.

Wilson, C. R. and Haubrich, R. A. (1976). Meteorological excitation of the earth's wobble. Geophysical Journal International, 46(3):707–743.

Wilson, C. R. and Vicente, R. (1980). An analysis of the homogeneous ils polar motion series. Geophysical Journal International, 62(3):605–616.

Wilson, C. R. and Vicente, R. O. (1990). Maximum likelihood estimates of polar motion parameters. Washington DC American Geophysical Union Geophysical Monograph Series, pages 151–155.

RÉSUMÉ

À partir 20ème siècle, l'observation des variations de rotation de la Terre par les techniques astrogéodétiques permet d'examiner le propriétés rhéologiques globale de la Terre, en particulier les paramètres de résonance des modes de rotation libre.On peut obtenir de meilleures contraintes sur ces paramètres de résonance en confrontant le mouvement du pôle observé, y compris la nutation en tant que mouvement du pôle rétrograde diurne, à l'excitation modélisée qui le produit. Une mise à jour des paramètres de résonance confirme, particuliarement, le raccourcissement de la période de résonance du mouvement du pôle dans la bande diurne. Ensuite, nous montrons que le comportement dynamique des océans dans la bande diurne est principalement responsable de cela. Nous avons également prédit une modification supplémentaire des paramètres de résonance au tour de la résonance de nutation libre du noyau, comme prévu de la réponse de la Terre solide, et confirmez-le par une analyse de nutation. Enfin, nous étendons cette étude au mouvement du pôle prograde diurne, où les excitations, principalement dues à la marée océanique.

MOTS CLÉS

Rotation de la terre - Structure de la terre - Géodésie spatiale

ABSTRACT

The observation of Earth rotation variations through astrogeodetic techniques enables to investigate the global rheological properties of the Earth, particularly the resonance parameters of the free rotation modes. Better constraints on these resonance parameters can be obtained by confronting the observed polar motion, including nutation as a retrograde diurnal polar motion, to the modeled excitation producing it. An update of the resonance parameters confirms, in particular, the shortening of the polar motion resonance period in the diurnal band. Then, we show that the dynamical behavior of the oceans in the diurnal band is mostly responsible for that. We also predicted a supplementary change of the resonance parameters in the vicinity of the free core nutation resonance, as expected form the solid Earth response, and confirm it by nutation analysis. Finally, we extend this investigation to the prograde diurnal polar motion, where excitations, mostly resulting from the ocean tidal.

KEYWORDS

Earth rotation - Structure of the Earth - Space geodesy